Self-Encapsulation of Vaccine Antigens in PLGA Microparticles and Microneedles

By

John Maxwell Mazzara

A dissertation submitted in partial fulfillment
of the requirements for the degree of
Doctor of Philosophy
(Pharmaceutical Sciences)
in the University of Michigan
2016

Doctoral Committee:

Professor Steven P. Schwendeman, Chair
Research Professor Gregory E. Amidon
Adjunct Associate Professor Susan M. Ciotti
Assistant Professor James J. Moon
Associate Professor Max Shtein

Dedication

To you, dear reader.

I hope you find what you're looking for.

Acknowledgements

Science isn't done in a day, a year, or a decade. Science isn't even done over a lifetime; it is done through a connected stream of knowledge and dedication that spans throughout all people. So while I have many people to thank for their assistance, I must also thank the people whom helped the people that helped me, and so on. We are all in this together.

I must first thank my advisor, Dr. Steven Schwendeman for his support and guidance over the years. Dr. Schwendeman helped mold me into an independent scientist capable of critical thought and useful scientific exploration. He continues to build an excellent team of scientists, and I have been fortunate to benefit from his expertise and leadership. I also thank my thesis committee. Dr. James Moon and his research group, especially Lukasz Ochyl, have been invaluable in their assistance with planning and executing immunological studies – I owe them all a great deal of gratitude. Dr. Susan Ciotti is one of the most passionate and practical scientists I have met, and her long-time guidance of my scientific development has been enormously helpful. Likewise, Dr. Greg Amidon is a scientist all students can look up to. His combination of critical thinking, dedication to science, and groundedness is rare among scientists. I also owe many thanks to Dr. Max Shtein for stepping in

to help with my dissertation. It has been a great pleasure working with him and his research group. The same goes for Dr. Michael Thouless and his student Jessie Huang, who have been very gracious in helping with the materials sciences aspects of this work. Without their collaboration this project would never have got off the ground. I also owe thanks to Dr. Mark Prausnitz and his research group at Georgia Tech for taking me in and giving me a home away from home. Collaborating with a world expert in the field was a wonderful experience.

I have also been very fortunate to work with some incredibly talented scientists over the years. Additional members of the Schwendeman lab including Dr. Anna Schwendeman, Karl Olsen, Rose Ackerman, Dr. Desai, Dr. Milacic, Dr. Patel, Dr. Keiji, Yajun, Ronak, Brittany, Amy, Karthik, RaeSung, Kelly, Morgan, Kari, Jia and others helped build an environment of learning that has gotten me to this point. Likewise, Linda Barthel at MIL, Joel Whitfield at the Immunology Core, Dr. Kai Sun at EMAL, Leslie George and the LNF, and many other staff at the various core centers across the university have been incredibly helpful. And an extra thank you to the dedicated staff at the U of M College of Pharmacy for helping make everything run as smooth as possible. I am also very grateful to all my funding sources including the University of Michigan, the College of Pharmacy and its donors, and the PhRMA Foundation for supporting me and my research during this long process.

While graduate school can be overwhelming, it has also been some of the best times of my life. I would never have got through it without the help of my friends, including Brittany, Amy, Karthik, Kelly, Morgan, my co-worker Jamie, and many many others. 4 o'clock on a Friday will not be the same without you all.

And of course, everything I do is done with the support and encouragement of my family. I am blessed to have such wonderful parents and in-laws. Thank you all for your patients, care, and love.

And lastly, if dissertations could have co-authors, it would be my amazing wife Jackie. She served as editor, reviewer, assistant, advisor, counselor, friend, and wife all at once. She gave me the strength and support I needed to attempt and finish graduate school, and she makes every day amazing.

For today, good-bye. For tomorrow, good-luck. And forever, Go Blue!

Table of Contents

List of Figures

List of Tables

Abstract

There is an urgent need to reduce reliance on hypodermic injections for many protein-based therapies. Alternative approaches include developing controlled release formulations, which reduce dosing frequencies, and utilizing alternative delivery devices, such as microneedles. This thesis explores the development of controlled release microparticles made of poly(lactic-*co*-glycolic acid) (PLGA) that encapsulate stable/active proteins. These microparticles are then delivered via novel microneedle patches. This work has great implications for improving the utility and coverage of protein-based vaccines.

PLGA microparticles are loaded with protein through a novel approach termed active self-healing encapsulation (ASE). This method loads proteins after microparticle fabrication, thus preventing protein exposure to a variety of stresses. ASE utilizes a protein trapping agent (Alhydrogel), along with the self-healing of microparticle surface pores to sequester and trap proteins inside the microparticles. The self-healing phenomenon was explored in detail, and was determined to be a viscoelastic response of the polymer to high surface tension when above the glass-transition temperature (T_g). The healing kinetics followed expected Williams-Landel-Ferry behavior, and Arrhenius plots generated activation energies consistent with polymeric creep. A mathematical model to predict healing times is also presented.

The ASE technique afforded high loading (1.64% *w/w*) and encapsulation efficiencies up to 91% for the model protein Ovalbumin. *In vitro* controlled release was shown to be biphasic, with an initial release of soluble protein followed by a delayed release of Alhydrogel-complexed protein over the course of two months. Furthermore, a bulk batch of microparticles can be used to load many different proteins without needing to reformulate unique batches.

A process was also designed to deliver protein-loaded microparticles via a microneedle patch. Microneedle patches can be easily self-applied, are easy to store/dispose, and are generally preferred by patients over traditional hypodermic needles. These patches, made of a dissolvable material, successfully delivered microparticles intradermally where they began antigen release. In animal models these patches generated a robust immune response that was as good as or better than conventional administration techniques.

This thesis lays the ground work for a versatile system for delivering protein-based vaccines with reduced dosing requirements or limited need for hypodermic injections.

Chapter 1: Introduction

1.1 Controlled Release

Very few therapies can be given once and have long-lasting or lifelong effects. Instead, most drugs demonstrate effectiveness only when their concentration at a particular site in the body is between some therapeutic window. Below this window, the patient does not experience any benefits, and above it the drug may begin to demonstrate deleterious side effects. In order to maintain drug concentrations within this therapeutic window, many therapies are given on a schedule. Common examples in oral medication are pain relievers and birth control medicines, while insulin injections represent the most common parenteral therapy. In both cases, the drug concentration rises after administration to therapeutic levels, but begins to drop after complete absorption until the process must be repeated.

While seemingly simple, the obstacles to scheduled dosing are numerous. For example, inconvenient dosing intervals, busy lifestyles styles, physical inabilities, and cost can all lead to decreased patient compliance. If the patient misses a dose, the drug concentration drops out of the therapeutic window and the treatment stops working. To overcome these obstacles, scientists have developed a variety of controlled release drug delivery (CRDD) systems that are designed to maintain therapeutic concentrations after a single dose for longer than would be possible with conventional drug products.

One area in particular where CRDD is desperately needed is treatments with biomacromolecules, such as proteins, antibodies, or nucleic acids. While small molecules like birth control drugs can be taken orally, biomacromolecules are degraded during oral administration and/or have poor gastrointestinal absorption, and must therefore be dosed via injection. Repeated injections can be painful, costly, cause psychological stress, and produce large amounts of biohazardous waste. Although there are many approaches to achieving CRDD, a long-studied approach is through the use of polymer systems that control the rate of drug release via a variety of internal and external mechanisms. While many of these have been used experimentally, only a few have seen approval and success on the clinical market.

1.1.1 PLGA

Poly(glycolic acid) was one of the early polymers used as a biodegradable/bioresorbable suture (1). To increase the suture half-life, the more hydrophobic lactic acid, with its sterically hindered ester bond, was later added to make poly(lactic-*co*-glycolic acid) (PLGA) (Fig 1-1). PLGA's history as a safe and biodegradable polymer stems from the biochemistry of its monomers, lactide and glycolide. These soluble acids are released as PLGA degrades through spontaneous chain cleavage caused by hydrolysis (2). Both monomers are viewed as natural products to the body, and are shuttled into normal biochemical processes. Lactic acid enters the Cori Cycle along with that produced by fermentation in the muscles and is converted to glucose in the

liver. Glycolic acid is either degraded to oxalic acid or malate, which then enters Krebs cycle (3).

Researchers soon found that by altering the ratio of lactide and glycolide, along with the molecular weight (*Mw*) of the polymer chains, the end-groups, and the concentration, degradation times could be tailored to the needs of the specific device – with release profiles lasting between days and years. PLGA has been used in a litany of FDA-approved products including bone regeneration scaffolds, cardiovascular stents, films/patches, and *in situ* forming gels (4). This has led to PLGA's success and popularity as a polymer for CRDD.

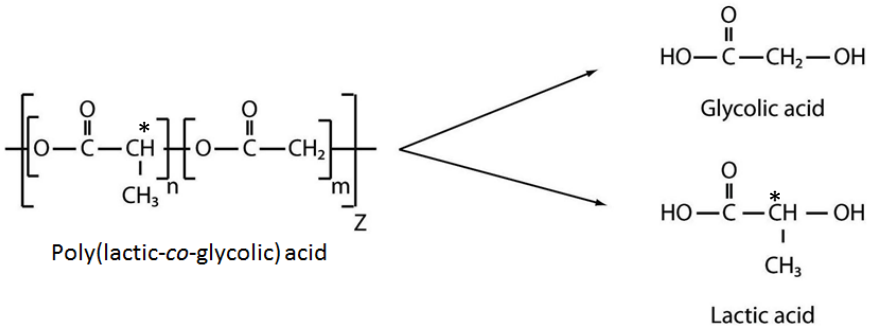

Figure 1-1: Molecular structure of PLGA. * denotes the sterocenter of lactide.

1.1.1.1 PLGA Microparticles

Perhaps the most common use of PLGA is as nano- or microparticles loaded with drug. These are small particles, typically spheres, of the polymer, which can be solid, contain cavities/pores, or be coated in other materials. As the polymer undergoes bulk degradation (in addition to other mechanisms) the payload is slowly released. A variety of techniques are available for making microparticles, but the most popular are emulsion or phase-separation based (5) (Fig 1-2). Here, the hydrophobic polymer is dissolved in an organic oil

phase. The oil phase is then added to a non-solvent (often water) with an emulsifying agent (such as poly(vinyl alcohol) (PVA)). The mixture is then stirred to evaporate the solvent, leaving behind hardened polymer particles. If the drug is hydrophobic (typical of small molecule drugs), then it can be dissolved along with the polymer in the oil phase, and the emulsion is a simple oil-in-water (o/w) type. If the drug is hydrophilic (typical of proteins), it is first dissolved in an inner-water phase, which is then homogenized into a larger volume of the polymer phase before that is added to the even larger aqueous bath solution. The result is a water-in-oil-in-water (w/o/w) emulsion. Other seldom used techniques include spray drying, melting/grinding, or supercritical fluid extraction (5).

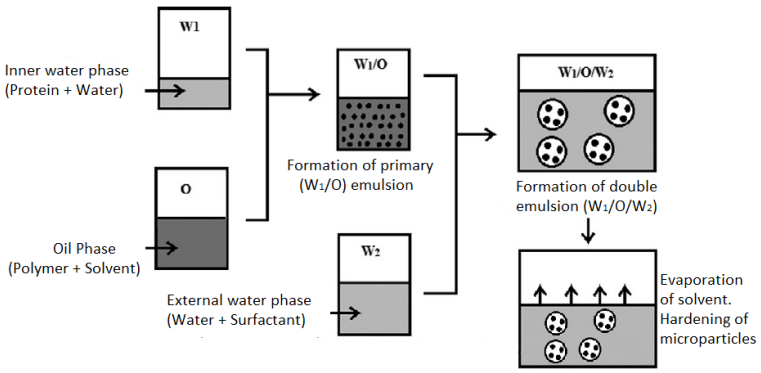

Figure 1-2: Double-emulsion fabrication process for PLGA microparticles. Modified from Ref. (6)

Mechanisms of Controlled Release from PLGA Devices

The manner in which PLGA microparticles release drug is dependent on many factors, and the rate-limiting process can change during the course of release. For certain low molecular weight drugs with similar solubility parameters to PLGA, the molecules may be able to directly diffuse out of the

polymer matrix. For other small molecules that do not dissolve in the polymer, and for all larger molecules, bulk erosion of the polymer microparticle must occur for the drug to be released (5). To begin the erosion process, water slowly diffuses into the polymer phase and molecular degradation occurs throughout the microparticle (rather than just at the surface). When the polymer chains reach a critical length, they become soluble and diffuse out of the microparticle through aqueous microchannels created by degradation.

When working with proteins or other larger hydrophilic biomacromolecules, the microparticles are usually made from a double-emulsion containing an inner water phase in which protein will reside (Fig 1-2). This inner-water phase creates a pore network that percolates throughout the bulk of the microparticle. For such microparticles, release is typically dependent on diffusion of protein out of these pores. If the pores are exposed/open on the surface of the microparticle, the protein can diffuse out. Thus, release is limited by both the rate of diffusion through these pores, and by the opening of the pores to the environment, which can also be dependent on the degradation kinetics of the polymer (7).

Another feature that has made PLGA such a useful polymer is its glass-transition temperature (T_g). The glass-transition is a feature of amorphous materials like PLGA. Unlike crystalline materials, amorphous materials do not have a long-range ordered structure; the molecules of an amorphous material tend to be arranged more randomly. When well below the T_g, polymer backbones are largely locked into their conformation, and the material is

referred to as a glass. Glasses tend to be brittle and highly viscous materials. Above the T_g, the molecules have improved mobility, and the material (now referred to as a rubber) is soft, malleable, and less viscous. The transition from glass to rubber is reversible and time-dependent, but is not a true phase-transition – the material remains a solid without translational molecular movement. As the chains gain mobility, the heat capacity of the material changes, allowing the transition to be recorded on a calorimeter. Many factors can affect when a polymer will undergo a glass-transition, including *Mw* and the degree of cross-linking or branching. Encapsulated drugs, excipients, solvents, and especially water can all act as plasticizers by increasing the free volume – essentially lubricating the polymer chains and dropping the T_g(8). In general, mechanisms such as hydration, degradation, and pore opening/closing do not occur with significant speed below the T_g, making it a critical feature to controlled release.

This feature is relevant for PLGA CRDD systems because the T_g of most hydrated PLGAs are just below body temperature; while dry it is well above normal ambient temperatures. This means that when stored on the shelf the chains cannot move, increasing the shelf-life and preventing serious morphological changes. Only when applied *in vivo* do the polymer chains begin to move, accelerating degradation and beginning drug release.

Limitations to Encapsulating Biomacromolecules

While some PLGA delivery systems have seen success on the market, several obstacles still limit their potential for future therapies. Sensitive biomacromolecules (henceforth generalized as proteins) have proven particularly challenging to deliver, which should be of great concern as pharmaceutical development becomes increasingly biologic. From formulation through release, there are many potential causes of protein instability. During microparticle manufacturing, for example, the emulsion is stirred quickly, creating high shear stresses and exposing the protein to large water-solvent interfaces, both of which are known to be sources of irreversible protein aggregation (9, 10). Furthermore, for use in humans, drug delivery systems must be sterile. Since maintaining aseptic manufacturing conditions of sterile starting materials is often cost-preventative, PLGA microparticles are usually terminally sterilized with γ-irradiation (11). The heat and energy imparted during this process can cause further disruption of protein structure (12). Additional limitations are damage caused during freeze-drying to increase shelf-life, and the relatively high cost of manufacturing PLGA (13). Therefore, there is significant need for an encapsulation paradigm that limits protein exposure to harmful conditions, and that limits the amount of PLGA and protein required for use.

A complication shared by both proteins and small molecules encapsulated in PLGA microparticles is high burst release (7). During this phase, a significant amount of drug is released during the early stages of incubation, occasionally

as high as 80% within just the first day (4). Since the goal of CRDD is to maintain therapeutic concentrations over an extended period, too much drug released over a short period of time is counterproductive. Not only does this beget the potential to increase concentrations above the therapeutic window and cause toxicity, it also limits the lifespan of the therapy and necessitates re-dosing earlier than maybe desired. While burst release has historically been attributed to liberation of drug from the surface of the microparticles (14), mechanistic research suggests that it may instead be controlled by the spontaneous opening and closing of the surface of the pore network where solubilized drug resides (15, 16).

Pore Behavior and Utility in PLGA Microparticles

As previously mentioned, PLGA microparticles often contain an aqueous pore network. This is most prominent when working with microparticles created via a w/o/w double-emulsion. When creating the emulsion, the inner water phase forms droplets within the polymer solution. Typically, this inner water phase will contain the dissolved proteins, along with excipients such as sugars and salts that may be included for stability purposes. These dissolved solutes create an osmotic force inside the microparticles. When the two inner phases are added to the final outer water phase, if the outer water phase is not osmotically balanced to the inner water phase, the osmotic pressure difference can rupture or crack through the polymer, thus creating an opening to the pores on the surface (a surface pore) (4). Other pores are also formed when the

solvent leaves the polymer phase during both solvent evaporation and freeze-drying.

When the finished microparticles are again introduced into an aqueous environment (*e.g.*, during release), these pores fill with fluid, redissolving any protein and excipients present. Again, since these entities generally cannot diffuse into or through the polymer, the rate-limiting step to their release is the diffusion through the pores and out of the microparticles. However, it has been noticed that the surface of these pores are not static. Rather, they appear to be capable of opening and closing (or vice versa) during release/incubation. In general, it has been noticed that in the early stages of release the pores may be open, either occurring during microsphere preparation or as a result of water entering and swelling the microparticles during the initial burst phase. After some period of time, however, the pores spontaneously close and the microparticles becomes smooth (7, 16). The time window over which this process occurs appears to closely match the beginning and end of the initial burst release phase (7). Thus, it appears plausible that rather than release of unencapsulated protein from the surface, initial burst release may actually be caused by the rapid diffusion of protein out of the open pores, and its cessation is caused by the healing of said pores preventing further protein from escaping. For some period of time, the microparticles remain smooth, which appears to correspond to the lag phase where little to no protein is releasing. Then, in the final stages of release the polymer physically degrades and new pores form as the microparticles fall apart, allowing the remaining cargo to be

released. In summary, it appears that in the case of biomacromolecules, the physical behavior of these polymer pores can be the rate-limiting step to release. However, the mechanisms and driving forces that govern pore behavior are poorly understood. On a final note, evidence suggests that the healing of the pores only takes place above the T_g (17). This indicated there is a polymer chain mobility component, and that the rate of healing/opening may depend on the physical-chemical properties of the polymer.

The mechanism by which the surface pores of PLGA heal-over has not been well studied, and it remains unclear to what extent various forces drive the process. It is currently hypothesized that PLGA microparticles have high surface/interfacial tension in air and water, respectively, caused by the solvent evaporation process. When the polymer is raised above T_g the chains are able to relieve this stress by rearranging via reptation to minimize the surface area, thus healing the pores. In this way, self-healing could be considered a form of creep (18). If true, then the rate of healing would be dependent on the viscoelastic properties of PLGA (such as Young's Modulus) and healing kinetics should fit the Williams-Landel-Ferry equation (WLF) of time-temperature superposition. This equation states that since viscoelastic moduli decrease predictably with temperature, a shift factor exists that allows data from viscoelastic experiments performed at different temperatures to superimpose (18).

Passive Self-Encapsulation

After the discovery that healing of surface pores can trap proteins inside PLGA microparticles and prevent their release, it was proposed that the closing of these pores could be used to entrap drugs inside the microparticles as a new loading paradigm (19). In this strategy, called self-healing encapsulation, porous PLGA particles were created via a double-emulsion without protein present. This made "blank" or empty microparticles. These microparticles were then incubated in a protein solution and the temperature was slowly ramped from 4 to 42 ˚C (above T_g). The microparticles were then washed and analyzed for protein content. Indeed it was found that microparticles could be loaded in this fashion, and the amount of drug encapsulated in the microparticles increased linearly with the protein concentration of the loading solution and the porosity of the microparticles. This approach is unique in that it does not expose the proteins to the conditions used to fabricate the microparticles.

Prior to loading, the microparticles were porous, but afterwards they were smooth. Furthermore, when the microparticles were reintroduced to a release solution at 37 ˚C, the pores slowly reformed and the protein was released over several days. Of significant importance however, was that because the pores were closed at the beginning of release, a severe attenuation in initial burst was observed. Instead, the microparticles demonstrated more linear early-phase release kinetics.

While this development was promising, it carried two serious caveats. First, since the pores were simply equilibrating with the protein loading solution, but

the volume of the pore network was much lower than the overall loading solution, there was poor encapsulation efficiency (~30%). Given the cost of many protein drugs, this made the strategy interesting, but not useful. Additionally, in order to achieve useful loading (>1%), very high protein concentrations were required – upwards of 240 mg/mL. Such a system is not translatable to all biomacromolecules, as solubility and aggregation complications may arise at such high concentrations.

Active Self-Encapsulation

To overcome the limitations mentioned above, investigators sought a way to sequester proteins exclusively inside the microparticles rather than relying on diffusion/equilibration from a loading solution. If a trapping agent could be included in the microparticles, it would provide a driving force to draw protein from solution into the microparticles, thus wasting less protein (improve encapsulation efficiency) and allowing the use of lower concentrations (Fig 1-3). This technique, referred to as Active Self-Encapsulation, is currently being investigated with a variety of trapping agents. The trapping agent selected depends primarily on the protein of interest, but is some entity that will bind to the protein. Examples of trapping agents include zinc complexes, biopolymers, and metal-based vaccine adjuvants (20, 21). Of focus here will be the vaccine adjuvant class, particularly aluminum hydroxide gel (Alhydrogel). More detail is provided on Alhydrogel in future sections, but it is known to bind many negatively charged or phosphorylated proteins. It has excellent adsorption

capacity, up to 3 mg protein/mg Alhydrogel (22). By including this in the microparticles, very little unencapsulated protein is left in the loading solution (up to 98% encapsulation efficiency) (21).

The potential of Active Self-Encapsulation is its ability to separate proteins from the damaging aspects of manufacturing mentioned previously. Now, microparticles can be prepared and sterilized in the absence of protein, stored in bulk, and loaded only when needed at the point of care (*i.e.*, at the pharmacy or in the field). This paradigm can also significantly reduce costs since more of the protein in the microparticles is in the therapeutic state. Moreover, the absence of a large initial burst and a longer delivery lifetime means less frequent and safer dosing. Finally, since Alhydrogel binds to many different proteins, the same parent batch of microparticles can be used to load a variety of different proteins.

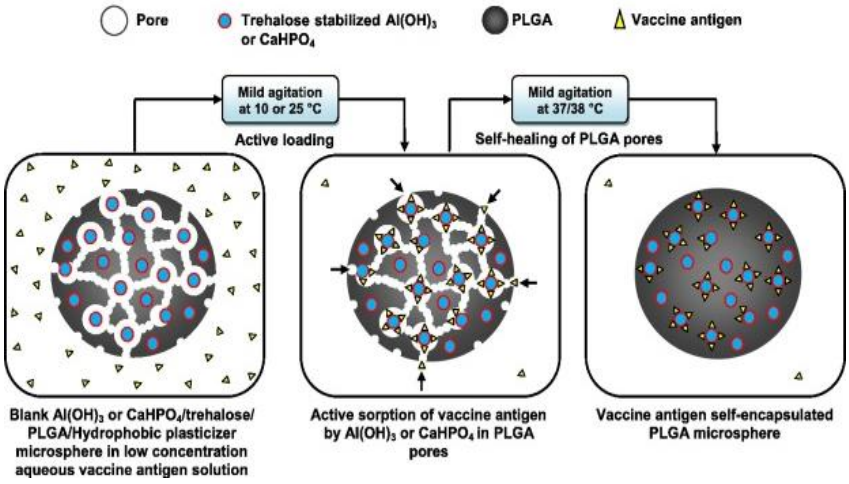

Figure 1-3: Schematic of Active Self-Encapsulation system. From Ref. (21)

1.2 Vaccination

The concept of intentionally manipulating the immune system to prevent future diseases dates back several millennia and is often considered to be the single greatest advancement in the defense against disease (23). Active immunization is the process where an individual is intentionally exposed to a pathogen-derived antigen to prime the adaptive immune response before any infection actually develops.

There are several types of vaccines, each with distinct advantages and disadvantages. The first type heavily used in the USA was Salk's killed (inactivated) Poliomyelitis vaccine. This was a fully inactivated pathogen. When injected, no infection develops; instead, antigen-presenting cells (APCs) engulf the antigen, and a humoral immune response begins. Because there is no infection, the immune response is weak and lacking cell-mediated aspects. Several boosters are needed to fully develop and maintain humoral memory.

To create a stronger immune response, Saban's Polio vaccine contains a whole but partially attenuated form of the virus. When injected, a transient infection develops that does not demonstrate the symptoms of the disease. This leads to a strong humoral and cell-mediated response requiring fewer (typically only one) boosters. The drawback of this vaccine class is the chance that the virus will revert to its fully infectious form and cause the disease it is designed to prevent (24). Modern vaccines in development are attempting to use purified recombinant proteins or DNA from pathogens. While the hope is these may lead to new treatments that can provide both cell-mediated and

humoral immunity with no chance of reversion, they have thus far proved poorly immunogenic, and very few 'modern' vaccines have been approved for use, with 'old school' vaccines still dominating the market (25).

1.2.1 Vaccine Adjuvants

Not all vaccines (particularly those that do not establish infection) properly stimulate immune cells. Early researchers noticed this when they added blended bits of bacteria to purified antigen and the response improved (26). Now referred to as adjuvants, these are any materials that enhance the immune response towards a vaccine. In modern vaccinology, adjuvants also help stabilize antigens during storage and administration (26).

Currently, the most common type of adjuvants approved for human use in the USA are salts and gels based on aluminum (27). The exact mechanism through which these work is still hotly debated, but can be summarized briefly into three processes: (A) extends residence time of antigen in tissue through slow release from the gel surface, (B) creates a particulate, rather than soluble form of antigen that is easier for APCs to engulf, (C) aluminum causes inflammation, recruiting immune cells to the antigen (22, 26). A common adjuvant, aluminum hydroxide gel (henceforth referred to as Alhydrogel) is a colloidal suspension of aluminum oxyhydroxide. It carries a positive charge below pH ~10.5, so it can electrostatically adsorb to many negatively charged proteins (28). This reaction is reversible through changes in pH or by outcompeting the adsorption with a strong co-ion (such as phosphate or

succinate). Also, because aluminum has a very high affinity for phosphate, Alhydrogel can undergo ligand exchange with the phosphate groups of phosphorylated proteins. This reaction is much stronger, and generally irreversible. When bound to Alhydrogel, the protein conformation is locked, and the protein-Alhydrogel complex takes on a colloidal state.

Despite its usefulness, Alhydrogel is also very sensitive. Freezing results in nearly complete loss of antigen binding. This is caused by ice crystals putting a compressive force on the particles – overcoming their surface repulsion and causing aggregation. Furthermore, the particles lose their internal water phase and settle (28-30). To protect Alhydrogel, it can be frozen by quick submersion in liquid nitrogen (29-30). This creates smaller, more numerous ice crystals than would form during a slow freeze. Additionally, a glass forming excipient such as the sugar trehalose can be included. This disrupts the hydrogen bonds of water and creates an amorphous glassy phase in which crystals do not properly form, thus protecting the Alhydrogel particles. Multiple studies have shown that when trehalose is included with Alhydrogel, aggregation of the particles is almost completely avoided (31, 32)

1.2.2 Controlled Release Vaccination Systems

The necessity of boosters in modern vaccines is one of the biggest hurdles to complete elimination of diseases for which vaccines currently exist. They are required because of the poor immune response to killed or purified vaccines leads to low numbers of poorly binding antibodies. In some cases, five or more

boosters are required before protective immunity develops. Reintroducing the antigen helps strengthen the antibody response, but also increases costs and patient discomfort, while decreasing compliance (33). To decrease reliance on boosters, researchers are investigating Single Administration Vaccines (SAVs). Early research in this field attempted to mimic the booster schedule of discrete, pulsatile release patterns via programmable implants or controlled release from distinct sections of a device (34, 35). However, it has been shown for decades that continuous antigen delivery can also serve to improve the immune response, and that the kinetics of antigen presentation significantly affects the strength of the response (36, 37).

PLGA microparticles have received much interest for their potential in SAVs. In fact, PLGA itself is considered a possible vaccine adjuvant because it demonstrates potential to elicit a $CD8^+$ cell-mediated response while also encapsulating the antigen without showing toxicity (33). While the controlled release potential of PLGA SAVs is enticing, these systems have thus far been plagued by the stability and cost concerns mentioned in Section 1.1.1.1, preventing them from serious human use. It has yet to be seen whether the addition of stabilizing excipients, along with the Active Self-Encapsulation paradigm, may allow PLGA to be used in a SAV device.

1.3 Microneedles for Drug Delivery

As the pharmaceutical field has become more advanced, there has been a push away from the once ubiquitous small-molecule drugs towards larger

biologics such as proteins, peptides, and DNA/RNA. However, these macromolecules are typically poorly absorbed and/or degraded in the gastrointestinal tract and liver (38). To overcome this, an increasing percent of medications, including many of the CRDD-types mentioned above, are relying on hypodermic needles for delivery. However, the hypodermic needle is a less-than-optimal delivery system. It is difficult to use (typically requiring a trained professional), painful, often fear-inducing, and risks spreading blood-borne pathogens if not disposed of properly. So, in the late 1990s scientists thought to shrink needles down to the micron scale to meet many of these challenges, and the field of microneedle drug delivery was born.

Primarily, four different types of microneedles exist (Fig 1-4). The first style created was solid metal microneedles. These are made from strong materials such as steel or silicon. Their purpose is not to deliver drugs themselves; rather they pierce the dense and impermeable upper layer of skin and create microchannels. When drug is applied later, either from a patch-based fluid reservoir or topical cream, it diffuses into these channels to enter the skin and/or dermal vasculature (39, 40). The next system developed was coated microneedles. The underlying structure here is the same as solid microneedles. However, before administration the microneedles are coated with a drug solution and then dried. The mechanical strength of the base material allows the microneedles to penetrate the skin, introducing the drug coating to the hydrated lower layers where it rapidly dissolves (40, 41). A number of therapeutics have been experimentally delivered using coated microneedles,

including protein and DNA vaccines (42). Since not all formulations are stable when dried, the next category of microneedles attempts to more directly mimic hypodermic needles. These microneedles have a hollow center through which drug can be delivered just past the upper layer of skin. This system allows specific amounts to be manually delivered via a syringe attached to the microneedles' backing (43), or can be diffusion-driven from a reservoir (44). Studies have shown that up to 1 mL of fluid can be injected with only mild pain (40). The final microneedle category is those made entirely from biocompatible compounds that erode when pressed into the skin to release encapsulated drugs. Often made from water-soluble polymers or sugars, the material is mixed with the drug and dried into a mold or melted and cast. After application, the microneedles dissolve/degrade and the drug is released into the skin where it can act directly or diffuse into the vasculature. Since all the material that has entered the skin remains there, this type has great potential to reduce biohazardous waste (40). There have also been combinatorial approaches, which utilize a sort of pedestal and arrow-head to lengthen the microneedles and help them better insert into the skin. In these cases the backing materials and pedestal may or may not be soluble, but the microneedle itself rests on the pedestal and dissolves more fully in the skin. This also helps reduce the amount of time the patch must remain on the skin, as the arrowhead may separate from the backing for extended dissolution (45).

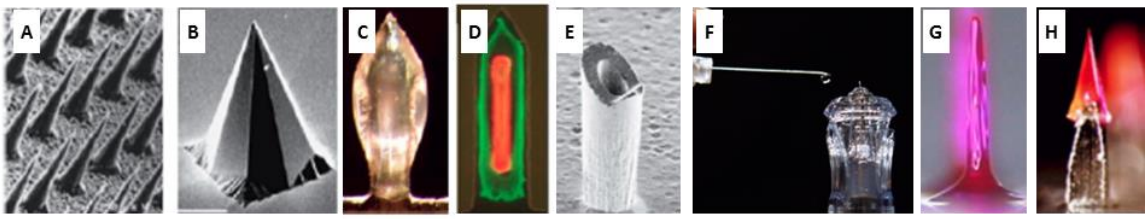

Figure 1-4: Various microneedles. *A* & *B*) Solid metal, *C* & *D*) Coated, *E* & *F*) Hollow, *G* & *H*) Soluble. From Ref. (40)

1.3.1 Anatomy of the Skin

The skin is the largest organ of the body, accounting for 10% of total body mass (41). It allows terrestrial life to exist by "keeping our insides in, and the outside out". While many consider it a simple static barrier, it is surprisingly dynamic and consists of separate well-defined layers. The deepest level is the hypodermis. This is a layer of subcutaneous fat between organs/muscles and the skin. It helps insulate the body and serves as an energy store. Above this is the dermis, which ranges between 3 and 5 mm thick in humans. The dermis is predominantly collagen and fibroblast cells, and is very hydrated to the point of sometimes being considered gelled water. This is the uppermost layer for blood, lymph, and nervous tissue, and the base for hair follicles and sweat glands. Apical to the dermis is the dermo-epidermal membrane, which separates the dermis from the epidermis. The epidermis ranges between 60-800 µm (average ~80 µm) and is composed mostly of avascularized keratinocytes. These cells are loosely bound together with desmosomes, with the basal layer bound to the dermo-epidermal membrane. Only the most basal monolayer of cells divide, with daughter cells being pushed up with each division. As cells move to the surface, they lose cellular functions, eventually

becoming part of the top layer, the stratum corneum (SC). The SC is ~10 µm thick, and is a very dense layer of dead keratinized cells embedded in a lipid matrix. The brick-and-mortar makeup of this layer prevents absorption of hydrophilic substances or penetration of large molecules. It is the rate-limiting layer to trans/intradermal drug delivery and absorption, with no useful cellular activity (41).

The skin also hosts a variety of different cells and molecules, both resident and recruited. Like the gut, it is home to a diverse non-pathogenic microbiome. The cells and extracellular fluids have also been estimated to have an enzymatic capacity roughly 5% that of the liver. Finally, the skin has a powerful immune system capable of operating on its own and in coordination with the rest of the body (41).

1.3.1.1 The Skin Immune System

It is intuitive that the body would put such a strong immunologic focus on the skin, as it interacts the most with the outside word. Early man evolved the immune system by stepping on rocks and scraping against bushes, and required skin immunity to survive past infancy. It is now projected that half of all cells present in the skin have some immunologic function, and the phrase *skin-associated lymphoid tissue* (SALT) is used to describe their interactions (46).

The most immunogenic cells are dermal dendritic cells (DCs), and their epidermal subset, Langerhans cells (LCs). Both are phagocytic antigen presenting cells (APC)s, but LCs are found only in skin and mucosa, making up

3-5% of epidermal tissue (47). They are voraciously phagocytic and, like DCs, express Toll-like Receptors (TLRs) to identify pathogens via pathogen-associated molecular patterns (PAMPs). After ingesting an antigen, LCs and DCs enter lymphatic vessels located in the dermis and travel to skin-draining lymph nodes. There they mature and express the antigen on MHC I and/or II receptors to lymphocytes circulating in the lymph node – beginning the adaptive response (26). There is also a native T cell population that is estimated to be larger than that in peripheral blood (46).

Cells of the innate immune system also reside in the skin. Histocytes are resident macrophages that exist in both the dermis and epidermis and act as professional phagocytes and APCs. The abundant keratinocytes express TLRs, and react to pathogens by releasing inflammatory cytokines, which recruit non-native inflammatory cell and T cells to the skin (46, 48).

1.3.2 Intradermal Vaccination via Microneedles

Because of its powerful immune system, the skin is a potent site for vaccination, and microneedles are poised to become the new standard in intradermal (i.d.) vaccination. While the i.d. route is mankind's oldest form of immunization, it has mostly lost ground to intramuscular (i.m.) and subcutaneous (s.c.) delivery. Only the Mantoux technique remains common, which is used in the tuberculin "skin bump" test. However, this requires a high degree of skill to perform, as it utilizes a small-gauge needle inserted at an acute angle into the skin so as to not pass through the dermis. Smallpox

vaccines were also dosed i.d. using a special bifurcated needle that held vaccine between two prongs. The needle was repeatedly stabbed into the skin in a sacrificial technique to dose the antigen (49). The problem facing i.d. immunization is that while the skin is prevalent, its thinness makes it a difficult site to properly administer to. I.m. immunization, despite its flaws, is simple to perform. Microneedles, however, are specifically designed to overcome this challenge.

Several studies have suggested that i.d. immunization, including that from microneedles, may in fact be superior to the i.m. or s.c. routes. While those sites are easier to deliver to, they have lower concentrations of APCs. Antigen that is not presented on APCs does not contribute to immunological memory and is degraded. Since the skin is packed with APCs, less antigen is wasted and a smaller dose can be used to generate an equivalent response. Multiple clinical studies have shown that the when delivered i.d., a $1/5^{th}$ dose of influenza vaccine demonstrates similar or better results than a full i.m. injection (50, 51). Indeed the currently approved i.d. seasonal influenza vaccine, Fluzone I.D.® uses 40% less antigen than its i.m. counterpart. This device is a hollow microneedle that delivers an i.d. injection. In a separate study, when dried influenza virus-like particles were delivered using coated microneedles, the antibody levels were a full order of magnitude higher than the standard i.m. vaccination. Upon a second challenge, the recall antibody levels were also higher, and *in vivo* virus titers were lower (52). This suggests that the site of administration may be important even for systemic immunity.

In addition to the physiologic benefits, many experts agree that intra- or transdermal vaccination has logistical benefits, especially in mass or immediate vaccination campaigns. Current stockpiles contain millions of glass vials of vaccine solution stored in refrigerated warehouses, and must be kept cold during transportation. They also require trained personnel to administer the vaccine and dispose of the needles. It is estimated that storage, delivery, administration, and clean-up represent 80% of the cost of vaccine programs. However, a self-administered and freeze-dried vaccine, such as those tailored to the i.d. route, may help control these parameters while also decreasing the time required to get the treatment to populations in need, thus increasing the country's resiliency to mass vaccination scenarios (51).

1.4 Thesis Outline

The preceding sections highlight two important topics that require further research. First, there are large gaps in the understanding regarding the self-healing phenomenon observed in PLGA microparticles. If the self-encapsulation technique previously mentioned is to be commercially employed, a more mechanistic awareness will be required. Second, as microneedles are a relatively new technology, there is great opportunity to utilize them in novel ways; particularly with regards to intradermal vaccination. This work will explore three connected topics. First, there will be a mechanistic evaluation of self-healing in PLGA. This enhanced understanding will then be used to further explore the potential of Active Self-Encapsulating PLGA microparticles for the

controlled release of stable vaccine antigens. Finally, this microparticle technology will be translated to a microneedle system for intradermal vaccination without the use of hypodermic needles.

In Chapter 2, a model system is developed for studying self-healing in PLGAs. This system removes many of the complexities involved with studying surface morphology on PLGA microparticles. Using this system, various effectors to pore healing are studied, such as pore geometry, PLGA structure, and environmental conditions. These studies allow for elucidation of the physical-mechanical nature of PLGA molecules during self-healing. Mathematical representations of the self-healing process are presented and existing polymer theory is modeled over the data. This chapter presents the underlying driving forces and limiting factors in self-healing, and is designed to empower researchers with better information as to how best utilize the technique in future work.

Chapter 3 more directly capitalizes on self-healing by further exploring the Active Self-Encapsulation loading paradigm. PLGA microparticles are fabricated using Alhydrogel as a trapping agent. These microparticles are then evaluated *in vitro* for their ability to load and release stable vaccine antigens. Also included is an investigation into the various mechanisms of antigen release. This includes the evaluation of several clinically relevant antigens.

Chapter 4 then takes these microparticles and encapsulates them in a microneedle patch. This patch is fully soluble, and designed to embed the loaded microparticles in the epidermis and dermis without the use of a

hypodermic needle. The mechanical strength of these microneedles is evaluated, with consideration towards how well and how deeply they are able to penetrate model skin tissue and deposit the microparticle payload. The patches are evaluated *in vitro* to determine if the controlled release capabilities of the microparticles have been affected. Lastly, the work concludes with an *in vivo* study of the capability of the microneedle patches to illicit a robust immune response in an animal model.

It is the intention of Chapter 5 to summarize the important aspects of this work, and expound on potential future directions for these fields of research. Also included is an appendix of work collaboratively done to develop mathematical simulations of the self-healing process in PLGAs.

1.5 References

1. Schmitt EE, Polistina RA, inventors; American Cyanamid Company, assignee. Surgical Sutures. United States patent 3297033. 1963.
2. Alexis F. Factors affecting the degradation and drug-release mechanism of poly(lactic acid) and poly[(lactic acid)-co-(glycolic acid)]. Polymer International. 2005;54(1):36-46. doi: 10.1002/pi.1697.
3. Nelson DL, Cox MM. Principles of Biochemistry. Lehninger, editor: W.H. Freeman and Company; 2008.
4. Wischke C, Schwendeman SP. Degradable Polymeric Carriers for Parenteral Controlled Drug Delivery. Adv Del Sci Technol. 2012:171-228. doi: Doi 10.1007/978-1-4614-0881-9_8. PubMed PMID: ISI:000302879700008.
5. Wischke C, Schwendeman SP. Principles of encapsulating hydrophobic drugs in PLA/PLGA microparticles. International journal of pharmaceutics. 2008;364(2):298-327. Epub 2008/07/16. doi: 10.1016/j.ijpharm.2008.04.042. PubMed PMID: 18621492.
6. Giri TK, Choudhary C, Ajazuddin, Alexander A, Badwaik H, Tripathi DK. Prospects of pharmaceuticals and biopharmaceuticals loaded microparticles prepared by double emulsion technique for controlled delivery. Saudi Pharm J. 2013;21(2):125-41. doi: 10.1016/j.jsps.2012.05.009. PubMed PMID: ISI:000317354700001.
7. Wang J, Wang BM, Schwendeman SP. Characterization of the initial burst release of a model peptide from poly(D,L-lactide-co-glycolide) microspheres. Journal of controlled release : official journal of the Controlled Release Society. 2002;82(2-3):289-307. Epub 2002/08/15. PubMed PMID: 12175744.
8. Blasi P, D'Souza SS, Selmin F, DeLuca PP. Plasticizing effect of water on poly(lactide-co-glycolide). Journal of controlled release : official journal of the Controlled Release Society. 2005;108(1):1-9. Epub 2005/08/16. doi: 10.1016/j.jconrel.2005.07.009. PubMed PMID: 16098624.
9. Maa YF, Hsu CC. Protein denaturation by combined effect of shear and air-liquid interface. Biotechnology and bioengineering. 1997;54(6):503-12. Epub 1997/06/20. doi: 10.1002/(SICI)1097-0290(19970620)54:6<503::AID-BIT1>3.0.CO;2-N. PubMed PMID: 18636406.
10. Sah H. Protein behavior at the water/methylene chloride interface. Journal of pharmaceutical sciences. 1999;88(12):1320-5. Epub 1999/12/10. PubMed PMID: 10585229.
11. Desai KG, Kadous S, Schwendeman SP. Gamma Irradiation of Active Self-Healing PLGA Microspheres for Efficient Aqueous Encapsulation of Vaccine Antigens. Pharmaceutical research. 2013. Epub 2013/03/22. doi: 10.1007/s11095-013-1019-2. PubMed PMID: 23515830.
12. Alexander P, Hamilton LD, Stacey KA. Irradiation of proteins in the solid state. I. Aggregation and disorganization of secondary structure in bovine serum albumin. Radiation research. 1960;12:510-25. Epub 1960/05/01. PubMed PMID: 13792598.
13. Prestrelski SJ, Tedeschi N, Arakawa T, Carpenter JF. Dehydration-Induced Conformational Transitions in Proteins and Their Inhibition by Stabilizers. Biophys J. 1993;65(2):661-71. PubMed PMID: ISI:A1993LU23300014.
14. Cohen S, Yoshioka T, Lucarelli M, Hwang LH, Langer R. Controlled delivery systems for proteins based on poly(lactic/glycolic acid) microspheres. Pharmaceutical research. 1991;8(6):713-20. Epub 1991/06/01. PubMed PMID: 2062800.
15. Kang J, Schwendeman SP. Pore closing and opening in biodegradable polymers and their effect on the controlled release of proteins. Molecular pharmaceutics. 2007;4(1):104-18. Epub 2007/02/06. doi: 10.1021/mp060041n. PubMed PMID: 17274668.
16. Reinhold SE, Desai KG, Zhang L, Olsen KF, Schwendeman SP. Self-healing microencapsulation of biomacromolecules without organic solvents. Angew Chem Int Ed Engl. 2012;51(43):10800-3. Epub 2012/09/27. doi: 10.1002/anie.201206387. PubMed PMID: 23011773.
17. Mazzara JM, Balagna MA, Thouless MD, Schwendeman SP. Healing kinetics of microneedle-formed pores in PLGA films. Journal of controlled release : official journal of the Controlled Release Society. 2013;171(2):172-7. Epub 2013/07/09. doi: 10.1016/j.jconrel.2013.06.035. PubMed PMID: 23831588.
18. Zaoutsos SP, Papanicolaou GC. Viscoelastic constitutive modeling of creep and stress relaxation in polymer and polymer matrix composites. In: Guedes RM, editor. Creep and fatigue in polumer matrix composits. Pennsylvnia: Woodhead Publishing in Materials; 2011.

19. Reinhold SE. Self-Healing Polymers Microencapsulate Biomacromolecules Without Organic Solvents. University of Michigan, PhD Thesis, Department of Pharmaceutical Sciences. 2009.
20. Shah RB, Schwendeman SP. A biomimetic approach to active self-microencapsulation of proteins in PLGA. Journal of controlled release : official journal of the Controlled Release Society. 2014;196:60-70. Epub 2014/09/16. doi: 10.1016/j.jconrel.2014.08.029. PubMed PMID: 25219750; PubMed Central PMCID: PMC4268178.
21. Desai KG, Schwendeman SP. Active self-healing encapsulation of vaccine antigens in PLGA microspheres. Journal of controlled release : official journal of the Controlled Release Society. 2013;165(1):62-74. Epub 2012/10/30. doi: 10.1016/j.jconrel.2012.10.012. PubMed PMID: 23103983.
22. Hem SL, HogenEsch H. Aluminum-Containing Adjuvants: Properties, Formulation, and Use. In: Singh M, editor. Vaccine Adjuvants and Delivery Systems: John Wiley & Sons, Inc; 2007. p. 81-114.
23. Wilson-Welder JH, Torres MP, Kipper MJ, Mallapragada SK, Wannemuehler MJ, Narasimhan B. Vaccine adjuvants: current challenges and future approaches. Journal of pharmaceutical sciences. 2009;98(4):1278-316. Epub 2008/08/16. doi: 10.1002/jps.21523. PubMed PMID: 18704954.
24. David Salisbury KN, Mary Ramsay. Immunisation against infectious disease. Department of Health, Social Services and Public Saftey. 2006.
25. Oyston P, Robinson K. The current challenges for vaccine development. Journal of medical microbiology. 2012;61(Pt 7):889-94. Epub 2012/02/11. doi: 10.1099/jmm.0.039180-0. PubMed PMID: 22322337.
26. Murphy K, Travers P, Walport M, Janeway C. Janeway's immunobiology. 7th ed. New York: Garland Science; 2008. xxi, 887 p. p.
27. Cornelia Dekker LG, Jerome Klein. Dose Optimization Strategies for Vaccines: The Role of Adjuvants and New Technologies. Report of the National Vaccine Advisory Committee. 2008.
28. Lindblad EB, Schonberg NE. Aluminum adjuvants: preparation, application, dosage, and formulation with antigen. Methods Mol Biol. 2010;626:41-58. Epub 2010/01/26. doi: 10.1007/978-1-60761-585-9_4. PubMed PMID: 20099120.
29. Maa YF, Zhao L, Payne LG, Chen DX. Stabilization of alum-adjuvanted vaccine dry powder formulations: Mechanism and application. Journal of pharmaceutical sciences. 2003;92(2):319-32. doi: Doi 10.1002/Jps.10294. PubMed PMID: ISI:000180713200013.
30. Clausi AL, Merkley SA, Carpenter JF, Randolph TW. Inhibition of aggregation of aluminum hydroxide adjuvant during freezing and drying. Journal of pharmaceutical sciences. 2008;97(6):2049-61. Epub 2007/09/20. doi: 10.1002/jps.21143. PubMed PMID: 17879291.
31. Ohtake S, Wang YJ. Trehalose: Current Use and Future Applications. Journal of pharmaceutical sciences. 2011;100(6):2020-53. doi: Doi 10.1002/Jps.22458. PubMed PMID: ISI:000289442200004.
32. Solanki VA, Jain NK, Roy I. Stabilization of tetanus toxoid formulation containing aluminium hydroxide adjuvant against freeze-thawing. International journal of pharmaceutics. 2011;414(1-2):140-7. doi: DOI 10.1016/j.ijpharm.2011.05.022. PubMed PMID: ISI:000292795500018.
33. Jiang W, Gupta RK, Deshpande MC, Schwendeman SP. Biodegradable poly(lactic-co-glycolic acid) microparticles for injectable delivery of vaccine antigens. Advanced drug delivery reviews. 2005;57(3):391-410. Epub 2004/11/25. doi: 10.1016/j.addr.2004.09.003. PubMed PMID: 15560948.
34. Michael Cardamone SL, Jane Lucas, Rogan Lee, Michael O'Donoghue, Mal Brandon. In vitro testing of a pulsatile delivery system and its in vivo application for immunisation against tetanus toxoid. Journal of Controlled Release. 1997;47:205-19.
35. Vogelhuber W, Rotunno P, Magni E, Gazzaniga A, Spruss T, Bernhardt G, et al. Programmable biodegradable implants. Journal of controlled release : official journal of the Controlled Release Society. 2001;73(1):75-88. Epub 2001/05/05. PubMed PMID: 11337061.
36. Preis I, Langer RS. A single-step immunization by sustained antigen release. Journal of immunological methods. 1979;28(1-2):193-7. Epub 1979/01/01. PubMed PMID: 469267.
37. Johansen P, Storni T, Rettig L, Qiu Z, Der-Sarkissian A, Smith KA, et al. Antigen kinetics determines immune reactivity. Proceedings of the National Academy of Sciences of the United States of America. 2008;105(13):5189-94. Epub 2008/03/26. doi: 10.1073/pnas.0706296105. PubMed PMID: 18362362; PubMed Central PMCID: PMC2278203.

38. Singh R, Singh S, Lillard JW, Jr. Past, present, and future technologies for oral delivery of therapeutic proteins. Journal of pharmaceutical sciences. 2008;97(7):2497-523. Epub 2007/10/09. doi: 10.1002/jps.21183. PubMed PMID: 17918721.
39. Williams A. Transdermal and topical drug delivery: from theory to clinical practice. Pharmaceutical Press. 2003.
40. Kim YC, Park JH, Prausnitz MR. Microneedles for drug and vaccine delivery. Advanced drug delivery reviews. 2012;64(14):1547-68. Epub 2012/05/12. doi: 10.1016/j.addr.2012.04.005. PubMed PMID: 22575858; PubMed Central PMCID: PMC3419303.
41. Williams A. Transdermal and Topical Drug Delivery. London, GB: Pharmaceutical Press; 2003.
42. Kim YC, Quan FS, Compans RW, Kang SM, Prausnitz MR. Formulation and coating of microneedles with inactivated influenza virus to improve vaccine stability and immunogenicity. Journal of controlled release : official journal of the Controlled Release Society. 2010;142(2):187-95. Epub 2009/10/21. doi: 10.1016/j.jconrel.2009.10.013. PubMed PMID: 19840825; PubMed Central PMCID: PMC2823933.
43. Gupta J, Felner EI, Prausnitz MR. Minimally invasive insulin delivery in subjects with type 1 diabetes using hollow microneedles. Diabetes technology & therapeutics. 2009;11(6):329-37. Epub 2009/05/23. doi: 10.1089/dia.2008.0103. PubMed PMID: 19459760; PubMed Central PMCID: PMC2779563.
44. Hafeli UO, Mokhtari A, Liepmann D, Stoeber B. In vivo evaluation of a microneedle-based miniature syringe for intradermal drug delivery. Biomedical microdevices. 2009;11(5):943-50. Epub 2009/04/07. doi: 10.1007/s10544-009-9311-y. PubMed PMID: 19347587.
45. Chu LY, Prausnitz MR. Separable arrowhead microneedles. Journal of controlled release : official journal of the Controlled Release Society. 2011;149(3):242-9. Epub 2010/11/05. doi: 10.1016/j.jconrel.2010.10.033. PubMed PMID: 21047538; PubMed Central PMCID: PMC3040254.
46. Bos J, Luiten R. Skin Immune System. In: Stockfleth E, Ulrich C, editors. Skin Cancer after Organ Transplantation: Springer US; 2009. p. 45-62.
47. Burke KE, Anandasabapathy N. Cellular Immunity of the Skin: Langerhans Cells and Dendritic Cells. Innate Immune System of Skin and Oral Mucosa: John Wiley & Sons, Inc.; 2011. p. 195-214.
48. Miller LS. Toll-like receptors in skin. Advances in dermatology. 2008;24:71-87. Epub 2008/01/01. PubMed PMID: 19256306; PubMed Central PMCID: PMC2633625.
49. Kim YC, Jarrahian C, Zehrung D, Mitragotri S, Prausnitz MR. Delivery systems for intradermal vaccination. Current topics in microbiology and immunology. 2012;351:77-112. Epub 2011/04/08. doi: 10.1007/82_2011_123. PubMed PMID: 21472533; PubMed Central PMCID: PMC3173582.
50. Belshe RB, Newman FK, Wilkins K, Graham IL, Babusis E, Ewell M, et al. Comparative immunogenicity of trivalent influenza vaccine administered by intradermal or intramuscular route in healthy adults. Vaccine. 2007;25(37-38):6755-63. Epub 2007/08/19. doi: 10.1016/j.vaccine.2007.06.066. PubMed PMID: 17692438; PubMed Central PMCID: PMC2148502.
51. Glenn GM, Kenney RT. Mass vaccination: Solutions in the skin. Curr Top Microbiol. 2006;304:247-68. PubMed PMID: ISI:000242419300014.
52. Quan FS, Kim YC, Vunnava A, Yoo DG, Song JM, Prausnitz MR, et al. Intradermal vaccination with influenza virus-like particles by using microneedles induces protection superior to that with intramuscular immunization. Journal of virology. 2010;84(15):7760-9. Epub 2010/05/21. doi: 10.1128/JVI.01849-09. PubMed PMID: 20484519; PubMed Central PMCID: PMC2897640.

Chapter 2: Healing Kinetics of Microneedle-formed Pores in PLGA Films

2.1 Abstract

The spontaneous healing of aqueous pores in poly(D,L-lactic-*co*-glycolic acid) (PLGA) drug delivery systems has been identified to play a key role in terminating the burst release of large molecules, and to provide a means for novel aqueous-based microencapsulation. To examine healing of PLGA, pores were created of defined size and depth on the surface of thin PLGA films by stamping with blunt-tip microneedles. Pore dimensions on the micron-scale were relevant to surface pores of common PLGA microspheres and could be easily monitored by light microscopy. Most pores healed reproducibly at temperatures above the glass-transition temperature (T_g) of the films, with healing times decreasing sharply with increasing temperature according to Williams-Landel-Ferry (WLF) behavior. It is suggested that healing is driven by high surface tension in the films, and occurs through viscoelastic creep. Hydrated films healed at lower temperatures than dry films, consistent with a drop in T_g upon polymer hydration. Larger pores took longer to heal than smaller ones, while pores larger than 20 μm did not heal before significant polymer degradation occurred. Films of a less hydrophobic PLGA showed slower healing kinetics, attributed to a weaker surface tension driving force. Deeper pores showed signs of in-plane stress from spin-coating, and either ruptured or only partially healed when incubated wet and dry, respectively.

2.2 Introduction

Poly(D,L-lactic-*co*-glycolic acids) (PLGAs) have been studied exclusively for controlled release devices for delivery of peptides, proteins, vaccine antigens, and even nucleic acids [1-6]. Despite their widespread use over more than four decades, a few fundamental physical-chemical properties of PLGAs having significant impact on their biomaterial performance have nonetheless remained elusive. An important example involves the spontaneous self-healing of pores in the polymer that are created during processing (*e.g.*, microencapsulation and drying) and incubation. This phenomenon has been shown to play an important role in encapsulation and release of drugs and peptides [7-12], and could become of increased significance as the pharmaceutical pipeline becomes increasingly biologic, and greater precision and control is required of long-term controlled release devices.

Passive healing in polymers is a known occurrence [13], and can reasonably be expected to occur and have similar relevance in numerous other biomaterials (*e.g.*, poly(ethylene-*co*-vinyl) acetate and silicone rubber) commonly used for controlled release. For example, during previous evaluation of the release kinetics of a cyclic peptide (octreotide) from PLGA microspheres, the pores on the surface of the polymer were observed to slowly heal over a time-scale of hours in an aqueous medium [7]. The sealing of the surface pores was found to correspond to both the cessation of the initial burst release of peptide, and a sharp reduction in effective permeability of fluorescent markers capable of

entering the polymer matrix by pore-diffusion [7]. Similar behavior was also observed with bovine serum albumin (BSA) and dextran-loaded PLGA microspheres [14]. As the temperature was raised to a physiological temperature or above (*i.e.*, above T_g of the hydrated polymer [15]), the initial burst release of both dextran and BSA dropped as polymer healing became more rapid. The use of pore-markers incubated outside the PLGA microspheres indicated that the healing of pores also occurred during the degradation phase of the polymer, suggesting a two-way valve mechanism of large molecule release [14]. Finally, spontaneous pore closing in water has recently been shown to facilitate encapsulation of macromolecules [8,9,13] without exposing them to the damaging organic solvents and sterilizing conditions used in traditional fabricating/loading methods [16-22].

In order to better understand healing in PLGAs, developed here is a system that could be used to reproducibly evaluate the kinetics and mechanism of self-healing in the polymer. To accomplish this, blunt microneedles capable of creating well-defined pore morphologies within the surface of PLGA films were exploited. The purpose of this chapter is to describe this simple development and the key findings related to the kinetic behavior of PLGA self-healing of pores from a variety of pore sizes and depths.

2.3 Materials and Methods

2.3.1 Materials

Unless otherwise specified, the PLGA used was poly(D,L-lactic-*co*-glycolic acid) 50:50 with lauryl ester-terminated chains, inherent viscosity (*i.v.*) and weight-averaged molecular weight (*Mw*) of 0.61 dl/g in hexafluoroisopropanol (HFIP) at 25 ˚C and 55.3 kDa, respectively (Lactel Inc., Birmingham, AL). PLGA 504H (50:50, carboxylic acid-terminated, *Mw* = 38-54 kDa, *i.v.* = .45-.60 dl/g) was also purchased from Sigma-Aldrich (St. Louis, MO). All other chemicals were of analytical grade or higher.

2.3.2 Fabrication of Blunt-tip Microneedle Stamps

The general pattern of the stamps consisted of an array of square needles with inter-needle distance set at 10X needle width. Needles ranged between 1 and 250 µm-wide squares, while the depth was set at 7 or 15 µm. The smaller arrays (≤ 5 µm) were surrounded by a larger square (1 mm thick) so the target area could be easily located. Three separate stamps were used; one with needles 1, 2, 3, and 5 µm wide, 7 µm deep. The second contained needles 10, 20, 30, and 50 µm wide, also 7 µm deep. The final stamp had needles 50, 100, 150, and 250 µm wide, but 15 µm deep.

To form the microneedle stamps, a negative of the design was first drafted in L-edit (Tanner Research, Monrovia, CA), scaled up 5X from the final feature size. This was fractured into a series of squares and rectangles used to shoot the photomask reticle. The pattern was then exposed onto a 127 mm

photomask spin-coated with positive photoresist. After exposure, the photomask was developed in developer solution and the exposed areas were etched with chrome etchant before stripping away the remaining photoresist. The mask was then loaded into a stepper (GCA AS 200, Andover, MA), which scaled the feature size down by 5X, and the proper exposure times were determined incrementally. Silicon wafers were coated with 2.5 µm of positive photoresist (SPR 220 (3.0) series resist) by an ACS Cluster tool (SUSS MicroTech, Garching, Germany) and then etched (STS Pegasus 4, San Jose, CA) accordingly. The remaining photoresist was then stripped away and the wafers were characterized by contact profiling and SEM. Finally, the wafers were diced (ADT 7100, Horsham, PA) into usable sizes before being glued to a plastic dowel for grip.

2.3.3 Film Preparation and Stamping

PLGA films were prepared by dissolving the PLGA in acetone (27% *w/w*) and then spin-coating the solution onto cover-glass slides using a G3-8 Spin Coater (Specialty Coating Systems Inc., Indianapolis, IN). The volume used was 0.25 mL, coating time was 7 s, and the spin speeds were 1515 and 3200 rpm for ester- and acid-terminated polymers, respectively. The thicknesses of the films were determined by a microcaliper (Marathon, Ontario, Canada). Immediately after spin-coating, the microneedle stamps were gently pressed onto the film surface to create the indentation and then removed. Films were then dried for 24 h in a fume-hood and 24 h under vacuum. Sample quality was ensured by

viewing each sample on a light microscope (Axiolab, Carl Zeiss, Oberkochen, Germany) with 5-40X magnification. Images were taken with a Canon Rebel EOS XSi equipped with a 2.5X phototube (Carl Zeiss) attached to the microscope. All samples were imaged prior to incubation for reference. Excess glass and polymer were cut away from the stamp area and the samples were stored at 4 ˚C until further use.

2.3.4 Film Incubation

For incubation under aqueous conditions, the films were placed in plastic Petri dishes (5 cm diameter) and filled with 7 mL pre-warmed buffer solution before capping and allowed to stand during incubation (Precision, Thermo Scientific, Waltham, MA). The standard buffer was PBS (137 mM NaCl, 2.7 mM KCl, 10.1 mM Na_2HPO_4, 1.7 mM KH_2PO_4) + 0.02% Tween 80, pH 7.4 (PBST). At predetermined times, the media were discarded, and the films were rinsed with distilled and deionized H_2O to prevent salt formation. The films were then patted dry with tissue paper before immediate imaging. Three replicates were used for each time point and the samples were discarded after imaging.

Films incubated without aqueous media were placed and capped in the same Petri dishes under ambient conditions before being placed in the incubator. At predetermined times, they were removed from the incubator, imaged quickly, and then returned for further incubation.

2.3.5 Thermal Analysis

The amount of residual solvent was determined by thermogravimetic analysis (TGA) (Discovery, TA Instruments, New Castle, DE) as previously reported [22]. Briefly, 15-20 mg of sample were placed on platinum pans before equilibrating at 25 ˚C. The temperature was then ramped to 600 ˚C at 10 ˚/min. The solvent loss was determined from the mass lost between 25 ˚C and 150 ˚C, which is much lower than the temperature range over which significant mass loss of the polymer occurs.

Glass-transition temperatures were determined by modulated differential scanning calorimeter (mDSC) (Discovery, TA Instruments, New Castle, DE). Approximately 10 mg of sample were crimped in aluminum pans. Temperatures were ramped between -20 ˚C and 150 ˚C (80 ˚C for hydrated films) at 3 ˚C/min, with a modulation amplitude of ± 1 ˚C/min (1.5 ˚C/min for hydrated films) and a period of 60 s. All samples were subjected to a heat/cool/heat cycle. The glass-transition temperatures of hydrated films were determined by soaking them in PBST at room-temperature for 1 h before patting dry, removing the glass substrate, and sealing with hermetic lids. The analysis was done using TA Trios software, and all experiments were performed in triplicate.

2.4 Results

2.4.1 PLGA Films with Microneedle-stamped Pores

Spin-coating under the given conditions produced films 26 ± 3 and 24 ± 4 µm thick (mean ± SEM, n = 9) for ester- and acid-terminated films, respectively. The films began to dry rapidly after coating, so applying the microneedle stamps had to be done immediately. Each film was stamped several times in different locations, and the individual stamps were cut out after drying. Using the 1–5-µm stamp, only the 5-µm needles repeatedly produced usable pores. In some instances, and particularly with larger pores, a ridge appeared around the pores as a result of in-plane compressive stresses. This appears as a black ring in some light microscope images.

After drying, the films appeared generally uniform and transparent with a modest level of roughness (Fig 2-1). No significant differences were observed between the two PLGAs used, although different spin-speeds were required to achieve similar thicknesses. Pores ranged between 5 and 250 µm in width. The 5-µm-wide, 7-µm-deep pores were used for all experiments except when the effect of pore size was evaluated, as described below. The amounts of residual solvent and glass-transition temperatures are presented in Table 1.

2.4.2 Effect of Temperature on Healing Time in PBST

When PLGA films were incubated in PBST at temperatures of 43 °C and above, the pores slowly healed until the surface became uniform and no evidence of the pores could be observed by light or scanning electron

microscopy (SEM). For example, in Fig 2-2A films are displayed at different stages of the healing process under aqueous conditions. The morphology of the pores suggest that healing occurs both from the edges in and from the bottom up, as the initially square pores quickly became circular, but the outline of the pore could be observed throughout healing. The film around the pores became rougher as the incubation continued, likely due to hydration of the film or from buffer solution trapped between the film and the glass substrate after drying. As the incubation temperature increased, the healing times decreased, as shown in Fig 2-3A.

When films were incubated at 37 ˚C, they became an opaque milky-white, and SEM was required to evaluate pore morphology. Here, the early stages of healing could be observed (rounding out of pores and some loss of definition) but full healing did not occur after two weeks. Results were similar when incubated at 25 ˚C for one week, although the films remained translucent and any change to pore morphology was minimal. Finally, when incubated at 5 ˚C the films' morphology did not change, and remained smooth during a one-week incubation, suggesting only minimal hydration of the glassy polymer (supplementary information).

2.4.3 Effect of Temperature on Dry Healing

When the films were incubated dry, the required healing times jumped significantly, and the minimal required temperature to observe healing at reasonable time scales rose to 50 ˚C. Similar to the behavior of wet films,

further increases in temperature reduced healing time, as shown in Fig 2-3B. The pores also behaved in a similar fashion, becoming less well defined over time. In contrast to the wet films, the parts of the films surrounding the pores remained smooth throughout incubation (Fig 2-2B).

2.4.4 Healing Kinetics of Carboxylic Acid-terminated PLGA

When the more hydrophilic, carboxylic acid-terminated PLGA 504H was used in healing studies, the rate of healing slowed considerably. When incubated in PBST at 50 ˚C, healing was not complete after three days, at which point the polymer was severely degraded. Partially-degraded films were imaged on SEM, and unhealed pores were still clearly visible with only minor morphology changes (supplementary information). When incubated dry, healing proceeded similar to that of dry-healed ester-terminated PLGA films, but required higher temperatures. For example, the lowest temperature used was 55 ˚C, which took over 5 days before complete healing was observed (see Fig 2-4).

2.4.5 Fitting Williams-Landel-Ferry (WLF) and Arrhenius Equations to PLGA Healing Data

In order to test if polymer healing was dependent on the viscoelastic properties of the polymer, as would be expected if healing occurs by material flow to minimize surface energy, the healing times of 5-μm pores in both dry (ester- and acid-terminated polymers) and aqueous (ester-terminated only)

conditions were fit by the Williams-Landel-Ferry equation for time-temperature superposition:

$$\mathrm{Log}\left(\frac{t}{t_o}\right) = \frac{-C_1(T - T_o)}{C_2 + (T - T_o)} \qquad (1)$$

where t and T are time and temperature, respectively; t_o is the reference time at the reference temperature T_o, and C_1 and C_2 are constants. When T_g is used as the reference temperature T_o, then the constants C_1 and C_2 become universal values of 17.4 and 51.6 K, respectively [23]. The T_g recorded during the first heating cycle of mDSC were used (see Table 1), as this best simulates experimental conditions. Data were independently fit using non-linear regression to determine t_o for all data sets. As shown in Fig 2-4, the WLF equation could be adequately fit to the data ($r^2 > .951$), yielding $t_o = 1.78 \cdot 10^6$ h, $4.35 \cdot 10^6$ h, and $2.4 \cdot 10^8$ h for lauryl ester-terminated dry and wet films, and acid-end group dry films, respectively.

An approximate mechanics analysis of healing indicated that healing times should follow an Arrhenius rate law of the form:

$$t = Ae^{-Q/RT} \qquad (2)$$

Therefore, to determine the activation energy for the healing process, healing data were individually plotted on an Arrhenius plot ($\ln(t)$ vs. $1/T$) (Fig 2-4 inset). The activation energy (Q) was determined by dividing the slope of the line by the gas constant, R. The observed values of Q were 288 kJ/mol

(r^2 = .985), 193 kJ/mol (r^2 = .973), and 240 kJ/mol (r^2 = .991) for lauryl ester-terminated dry and wet films, and acid-end group dry films, respectively.

2.4.6 Effects of Pore Width

Pores could be made using microneedles of 5, 10, 20, 30, and 50 μm width, all at a depth of 7 μm. When incubated in PBST, the healing time was found to increase with pore width for the 5, 10, and 20 μm pores (Fig 2-5). Pores of 30 and 50-μm size displayed the beginning signs of pore closing, (*i.e.*, pores had become circular, and were becoming less distinct – consistent with healing in the smaller pores). However, complete healing was not observed by 48 h (at 50 ˚C), at which time the films were so significantly damaged by degradation that further observations were not possible (Fig 2-6A). Had a thicker film or non-degradable polymer been used, it is likely that these pores would have healed eventually.

2.4.7 Effects of Pore Depth

A set of pores with a depth of 15 μm, which extended them more than halfway through the 26 μm film, were also made with widths of 50, 100, 150, and 250 μm. When incubated in aqueous conditions at 50 ˚C, these pores tended to rupture rather than heal (Fig 2-6B). That is, the pores went from initially being a dent on the film surface, to a through-hole that extended to the glass substrate. The polymer at the bottom of the pores tore away from the glass, and the pores grew up to 300% in diameter while becoming more circular.

The larger pores tended to rupture less often than the smaller ones, although none demonstrated healing during the times studied (up to 48 h).

When the study was conducted under dry conditions at 60 °C, the rupturing phenomenon was not typically observed. These pores showed some signs of the onset of healing, but did not heal fully on relevant timescale (< 2 wks). The pores had clearly become smaller and less distinct, but never fully disappeared. On rare occasions, some of the pores did rupture, but did not grow as they had in the aqueous experiment.

2.5 Discussion

The model system of using PLGA films stamped with a microneedle array proved to be a reliable system for reproducibly measuring pore-healing. Pores could be made of controlled width and depth, and could be individually monitored by light microscopy or occasionally SEM. This method did demonstrate difficulties creating pores smaller than 5 μm wide, which may have been because the polymer solution was able to relax back into these small pores, or because the 10X inter-needle distance was not sufficient in these instances. An alternative currently being explored for making smaller surface pores is physical indentation by the tip of an Atomic Force Microscope (AFM), similar to a previously reported study [24]. In addition, Axelsson *et al.* used $ZnCl_2$ as a pore forming excipient in PLGA films, but this method produced pores with great polydispersity and it was not possible to have precise control over the number or spacing of the pores [25].

After drying, the films contained a slightly elevated level of residual solvent, but this was expected since drying at elevated temperature (annealing) could not be done, as it would also begin to heal the pores. The glass-transition temperatures recorded are in reasonable agreement with previously reported values, and a drop in T_g for the hydrated films is consistent with the plasticization effect of water on the polymer [15]. The change in T_g in the dry films compared to the raw polymer is likely due to residual solvent, which is partially released during the first heating cycle, and leads to the higher T_g seen in the second heating cycle. Since the acid-end capped films had more residual solvent, the T_g increases more dramatically between cycles. While the first T_g was used for analysis, the true T_g likely changes between the two reported values during the course of the experiment as more solvent evaporates or more water enters the polymer matrix [25].

It is known that mid-to-high *Mw* PLGA films have a high interfacial tension, particularly in aqueous environments. This is frequently demonstrated by low wettability and/or a high water droplet contact angle, and is the result of a combination of van der Waals' interactions, hydrophobic interactions, and preference of the methyl side chains of lactic acid units to orientate to the polymer-air interface [25-28]. While lauryl ester-terminated PLGAs are particularly hydrophobic, carboxylic acid-capped PLGAs are less so. This results in weaker hydrophobic interactions, and lower surface stresses as evident by more acute water-droplet contact angles [29]. While these effects are

particularly pronounced in aqueous environments, they also affect dry healing under ambient humidity, and weaken the tension at the polymer-air interface.

The results presented here are consistent with a model for pore healing driven by surface tension and controlled by the rate of deformation of the polymer. In the absence of any other stresses, the surface tension and local curvature set up a stress field that drives flow of the polymer to reduce the surface area and, hence, heal the pores. A simple special case that serves to illustrate the physics of the phenomenon is the healing of a spherical pore in a linear viscous material. The von Mises effective stress ($\tilde{\sigma}$) at a distance r from the surface of the sphere is given by

$$\tilde{\sigma} = 3\gamma a^2 / r^3 \tag{3}$$

where γ is the surface tension of the material, and a is the radius of the pore. Assuming that the material obeys a Levy-Mises flow rule with a linear relationship between the effective stress and effective strain rate ($\dot{\tilde{\varepsilon}}$):

$$\dot{\tilde{\varepsilon}} = \tilde{\sigma} / 3\eta \tag{4}$$

where η is the viscosity. Assuming a single thermally-activated mechanism for flow, with an activation energy Q, the viscosity is of the form

$$\eta = \eta_o \exp\left(Q / RT\right) \tag{5}$$

where η_o is a material constant, R is the molar gas constant, and T is the absolute temperature. These equations can be used to show that the healing time (t) for a spherical pore is given by

$$t = 2\eta_o a_o \exp(Q/RT)/\gamma \quad (6)$$

where a_o is the initial pore radius.

While this model has an oversimplified geometry and, probably, an oversimplified constitutive law, it does provide a good connection to many of the experimental observations. Firstly, it should be noted that the transition from the square pore to the rounded shape is a classic sign of a surface-tension driven phenomenon. The stresses that drive flow are inversely dependent on the local radius of curvature (as in Eqn. (3)), so there is a very large driving force for the sharp corners of a square to be rounded out, and the pore to take up a circular shape to minimize surface energy. Secondly, Eqn. (6) shows that the healing time is proportional to the initial pore size. A linear relationship would be a direct consequence of a linear constitutive law; non-linear materials would exhibit a non-linearity in this relationship. While there are only three data points in Fig 2-5, the data are in general agreement with what would be expected in this type of phenomenon. In ester-terminated PLGA, it is noted that all the pores 7 μm in depth began to heal when incubated above T_g in aqueous conditions, but not all pores managed to close completely before significant degradation took place. The potential of an upper size limit on healing has great implications for PLGA devices used in controlled release; since the healing

phenomenon is now gaining interest as a possible encapsulation strategy [13], it suggests that particularly large pores may not heal before a degradation phase begins. Any unhealed pores would contribute significantly to burst release upon incubation in release media. This may limit or add additional considerations to the types of PLGA devices that are considered for this loading paradigm. Lastly, Eqn. (6) suggests that an Arrhenius plot will give the activation energy for the flow process. Fig 2-4 shows such a plot, indicating activation energies of roughly 288 kJ/mol, and 193 kJ/mol for the ester-terminated polymer in dry and wet conditions, respectively, and 240 kJ/mol for dry acid-terminated PLGA – values within the somewhat wide range of apparent activation energies reported for polymer flow and relaxation [30-32]. A lower activation energy for the hydrated polymer is expected, as water acts as a lubricant to polymer flow. Also, despite healing slower, a lower activation energy for acid-capped PLGA compared to the ester-terminated PLGA is expected. The former has a lower *Mw* and a further depressed T_g, so the polymer chains have more freedom to move, and can do so more readily. However, the observed healing kinetics are slower in acid-capped PLGA due to a lower overall driving force. This is an important distinction with regards to self-healing in PLGA microspheres, as choosing a more mobile polymer may not always promote faster self-healing unless the effect on other parameters, notably surface tension, are considered as well.

Data from Figures 2-2 and 2-3, along with the T_g information, indicate that healing of the microneedle-stamped pores takes place in a reasonable time-

frame when the polymer is in the rubbery state above the T_g, but not in the glassy state below it. The time-temperature shift associated with the WLF equation for polymers is another manifestation of a thermally-activated process, with significant mobility being associated with temperatures above the glass-transition temperature. Driven by the stress of surface tension, this enhanced mobility allows viscoelastic flow of the polymer to heal defects. This flow in response to surface tension could be considered a form of creep that occurs when $T > T_g$. Although healing was not observed in aqueous conditions at 37 ˚C, it is clear from previous research that healing at this temperature is possible [13]. The WLF equation predicts that pores would have healed if experiments were carried out longer (35 days for healing in PBST at 37 ˚C, 65 days for dry healing at 46 ˚C). Microspheres typically have smaller pores, and may have greater surface tension caused by a very different manufacturing process, or a lower T_g due to the inclusion of excipients, thus allowing them to heal faster at 37 ˚C than is predicted here. Additionally, the reason pores in PLGA 504H did not heal when exposed to aqueous conditions is likely two-fold. First, this polymer degrades much faster than ester-capped PLGA, limiting the window over which healing can be seen. Second, the lower hydrophobicity caused by the presence of the carboxylic acid severely weakens the surface tension driving force.

The behavior of 15-μm deep pores when incubated under aqueous conditions was particularly intriguing. These pores did not heal, and in fact grew in size significantly and caused damage to the film. It is possible that this

occurred because the films were spin-coated to a glass substrate, and this allowed an in-plane stress to develop, as has been previously reported [33]. Therefore, the rupturing phenomenon might not be expected to extend to free-standing PLGA microspheres. Nonetheless, whether a pore will heal or extend and rupture depends on a competition between elastic strain energy and surface energy. The relative importance of these two terms is measured by the dimensionless group $\sigma a_o / \gamma E$ [34], where E is the appropriate elastic modulus of the polymer, and σ is the normal stress at the tip of the pore. If the value of this group is small, the problem is dominated by surface tension, and the pore is expected to heal. Conversely, if the value of this group is large, the problem is dominated by the elastic energy term and rupture is favored. It is possible that rupturing occurred more commonly under wet conditions because of moisture uptake by the polymer leading to an enhanced stress. It should be noted that swelling caused by moisture uptake for microparticles and other PLGA devices might cause the pores to open initially [7], depending on the relative time scales for moisture absorption and healing. Whether the pores would eventually heal or not would likely depend on the nature of any geometrical constraint (similar as that provided by the glass substrate) that might result in the evolution of elastic stresses.

2.6 Conclusion

Healing of PLGA devices is an important phenomenon with strong implications for affecting release kinetics and providing an avenue for aqueous-

based encapsulation of large molecules. The microneedle-stamped films used here are a simple way to study this phenomenon in a controlled pore geometry. This system allowed the healing behavior of different PLGAs exposed to various conditions to be identified, and the data was adequately described by universal WLF and Arrhenius behavior. Self-healing was consistent with a surface tension driven process, causing creep when the polymer was above the T_g and chain motion via viscoelastic flow was possible. In the future, this approach may allow more quantitative assessment of healing phenomenon in PLGA and other biomaterials.

2.7 Acknowledgements

The authors wish to acknowledge Leslie George and Sandrine Martin at the Michigan Laurie Nanofabrication Facility (LNF) for their assistance with microneedle fabrication. The LNF is funded in part by the National Science Foundation's National Nanotechnology Infrastructure Network. This study was funded by NIH EB08873.

2.8 References

[1] D.H. Lewis, Controlled release of bioactive agents from lactide/glycolide polymers, in: M. Chasin, R. Langer, (Eds.), Biodegradable polymers as drug delivery systems, Marcel Dekker, New York, 1990, pp. 1-41.

[2] L.J. Cleland, A.J. Jone, Stable formulation of recombinant human growth hormone and interferon-gamma for microencapsulation in biodegradable microspheres, Pharm. Res. 13 (1996) 1464-1475.

[3] S.P. Schwendeman, H.R. Costantino, R.K. Gupta, M. Tobio, A.C. Chang, M.J. Alonso, G.R. Siber, R. Langer, Strategies for stabilizing tetanus toxoid toward the development of a single-dose tetanus vaccine, Dev. Biol. Stand. 87 (1996) 293-306.

[4] K.A. Woodrow, C.J. Booth, J.K. Saucier-Sawyer, M.J. Wood, W.M. Saltzman, Intravaginal gene silencing using biodegradable polymer nanoparticles densely loaded with small-interfering RNA, Nat. Mater. 8 (2009) 526-533.

[5] K.G.H. Desai, S.R. Mallery, A.S. Holpuch, S.P. Schwendeman, Development and in vitro-in vivo evaluation of fenretinide-loaded oral mucoadhesive patches for site-specific chemoprevention of oral cancer, Pharm. Res. 28 (2011) 2599-2609.

[6] S.S. Venkatraman, L.P. Tan, J.F.D. Joso, F. Boey, X.T. Wang, Biodegradable stents with elastic memory, Biomaterials 27 (2006) 1573-1578.

[7] J. Wang, B. Wang, S.P. Schwendeman, Charcterization of the initial burst release of a model peptide from poly(D,L-lactide-co-glycolide) microspheres, J. Control. Release. 82 (2002) 289-307.

[8] S.P. Schwendeman, J. Kang, S. Reinhold, Methods for encapsulation of biomacromolecules in polymers, US Patent No. 8017155B2 (2011).

[9] S. Reinhold. Self-healing polymers microencapsulate biomacromolecules without organic solvents, Ph.D Thesis, (2009) University of Michigan.

[10] G. Zhu, S.R. Mallery, S.P. Schwendeman, Stabilization of proteins encapsulated in injectable poly(lactide-co-glycolide), Nat. Biotech. 18 (2000) 52-57.

[11] C. Pérez, G. Kai, Effects of salt on lysozyme stability at the water-oil interface and upon encapsulation in poly(lactic-co-glycolic) acid microspheres, Biotechnol. Bioeng. 82 (2003) 825-832.

[12] S.P. Schwendeman, M. Cardamone, M. Brandon, A. Klibanov, R. Langer, Stability of proteins and their delivery from biodegradable polymer microspheres, in: S. Cohen, H. Bernstein (Eds.), Microparticulate systems for the delivery of proteins and vaccines, Marcel Dekker, New York, 1996, pp. 1-50.

[13] S.E. Reinhold, K.G.H. Desai, L. Zhang, K.F. Olsen, S.P. Schwendeman, Self-healing microencapsulation of biomacromolecules without organic solvents, Angew. Chem. Int. Ed. 51 (2012) 10800-10803.

[14] J. Kang, S.P. Schwendeman, Pore closing and opening in biodegradable polymers and their effect on the controlled release of proteins, Mol. Pharm. 4 (2007) 104-118.

[15] P. Blasi, S.S. D'Souza, F. Selmin, P.P. DeLuca, Plasticizing effect of water on poly(lactide-co-glycolide), J. Control. Release. 108 (2005) 1-9.

[16] H. Sah, Protein behavior at the water/methylene chloride interface, J. Pharm. Sci. 8812 (1999) 1320-1325.

[17] Y.F. Maa, C.C. Hsu, Protein denaturation by combined effect of shear and air-liquid interface, Biotechnol. Bioeng. 54 (1997) 503-512.

[18] S.J. Prestrelski, N. Tedeschi, T. Arakawa, J.F. Carpenter, Dehydration-induced conformational transitions in proteins and their inhibition by stabilizers, Biophys. J. 65 (1993) 661-671.

[19] W.R. Lie, R. Langer, A.M. Klibanov, Moisture-induced aggregation of lyophilized proteins in the solid-state, Biotechnol. Bioeng. 37 (1991) 177-184.

[20] C.E. Holy, C. Cheng, J.E. Davies, M.S. Shoichet, Optimizing the sterilization of PLGA scaffolds for use in tissue engineering, Biomaterials. 22 (2001) 25-31.

[21] P. Alexander, L.D.G. Hamilton, A. Stacey, Irradiation of proteins in the solid state: I. aggregation and disorganization of secondary structure of bovine serum albumin, Radiation Research. 12 (1960) 510-525.

[22] S. Kim, D. Hong, Y. Chung, H. Sah, Ammonolysis-induced solvent removal: a facile approach for solidifying emulsion droplets into PLGA microspheres, Biomacromolecules. 8 (2007) 3900-3907.

[23] S.P. Zaoutsos, G.C. Papanicolaou, Viscoelastic constitutive modeling of creep and stress relaxation in polymer and polymer matrix composites, in: R.M. Guedes (Ed), Creep and fatigue in polymer matrix composites, Woodhead publishing in Materials, Pennsylvania, 2011, pp. 1-45.
[24] J.A. Yoon, J. Kamada, K. Koynov, J. Mohin, T. Kowalewski, K. Matyjaszewski, Self-healing polymer films based on thiol-disulfide exchange reaction and self-healing kinetics measured using atomic force microscopy, Macromolecules. 45 (2012) 142-149.
[25] S. Fredenberg, M. Wahlgren, M. Reslow, A. Axelson, Pore formation and pore closure in poly(D,L-lactide-co-glycolide) films, J. Control. Release. 150 (2011) 142-149.
[26] E.I. Vargha-Butler, E. Kiss, C.N. Lam, Z. Keresztes, E. Kalman, L. Zhang, A.W. Neumann, Wettability of biodegradable surfaces, Colloid and Polymer Sci. 279 (2001) 1160-1168.
[27] N.B. Viswanathan, S.S. Patil, J.K. Pandit, A.K. Lele, M.G. Kulkarni, R.A. Mashelkar, Morphological changes in degrading PLGA and P(DL)LA microspheres: implications for the design of controlled release systems, J. Microencapsulation. 18 (2001) 783-800.
[28] T.G. Park, Degradation of Poly(D,L-Lactic Acid) microspheres: Effect of molecular weight, J. Control. Release. 30 (1994) 61-173.
[29] J.Y. Yoo, S. Mitragotri. Polymer particles that switch shape in response to a stimulus. PNAS. 107 (2010) 11205-11210.
[30] Y.M. Boiko, Interdiffusion of polymers with glassy bulk, Colloid Polym. Sci. 289 (2011) 1847-1854.
[31] J.F. Mano, Study of the segmental dynamics in semi-crystalline poly(lactic acid) using mechanical spectroscopies, Macromol. Biosci. 5 (2005) 337-343.
[32] M.L.Williams, R.F. Landel, J.D. Ferry, The temperature dependence of the relaxation mechanisms in amorphous polumers and other glass-forming liquids, JACS. 77 (1955) 3701-3707.
[33] P. Damman, G. Sylvain, C. Séverine, S. Despres, D. Villers, G. Reiter, et al, Relaxation of residual stress and reentanglement of polymers in spin-coated films, Phys. Rev. Letts. 99 (2007) 036101-1-4.
[34] Z. Suo, W. Wang, Diffusive void bifurcation in stressed solid, J. Appl. Phy. 76 (1994) 3410-3421.
[35] D.Y. Kwon, A.W. Neuman. Contact angle measurement and contact angle interpretation. Adv. Colloid Interface 81 (3) 1999 164-429.
[36] J. Huang, J.M. Mazzara, S.P. Schwendeman, M.D. Thouless. Self-healing of pores in PLGAs. J. Control. Release. 206 (2015) 20-29.

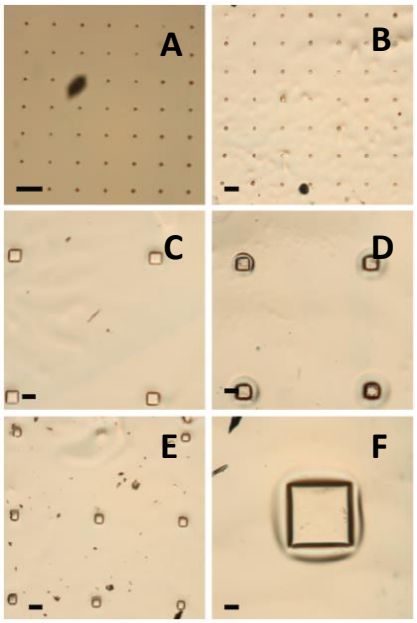

Figure 2-1: Representative light micrographs of PLGA films with various surface pores created by blunt-tip microneedle stamps. 7 µm deep and *A*) 5 µm wide, *B*) 10 µm wide, *C*) 50 µm wide, *E*) 30 µm wide; and 15 µm deep and *D*) 50 µm wide, and *F*) 250 µm wide.

Polymer End-cap	Residual Solvent (%)	Raw Polymer T_g (°C)		Dried Film T_g (°C)		Hydrated Film T_g (°C)	
		First Heat	Second Heat	First Heat	Second Heat	First Heat	Second Heat
Lauryl Ester	1.7 ± 0.1	42.7 ± 0.3	44.7 ± 0.2	35.4 ± 0.3	40.7 ± 0.3	23.4 ± 0.4	24.0 ± 0.3
Carboxylic Acid	3.6 ± 0.4	51.5 ± 0.6	48.4 ± 0.1	26.4 ± 0.4	45.1 ± 1.8	18.7 ± 0.5	18.5 ± 0.6

Table 2-1: Residual solvent and glass-transition temperature measurements as determined by TGA and mDSC, respectively. The T_g from the first heating cycle was used in further calculations. n = 3, ± SEM.

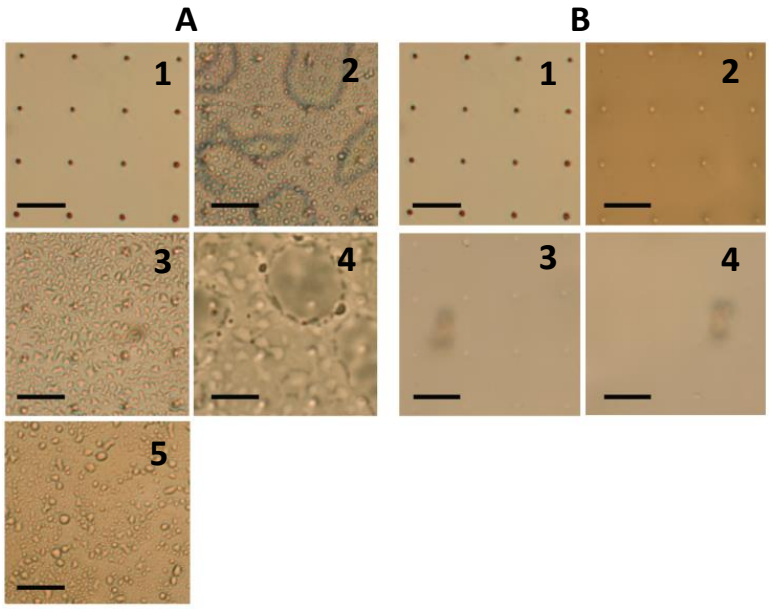

Figure 2-2: Healing of surface pores in *A*) PBST and *B*) air after; *1*) 0 h, *2*) 2 h, *3*) 4 h, *4*) 6 h, and *5*) 8 h. Scale = 50 µm.

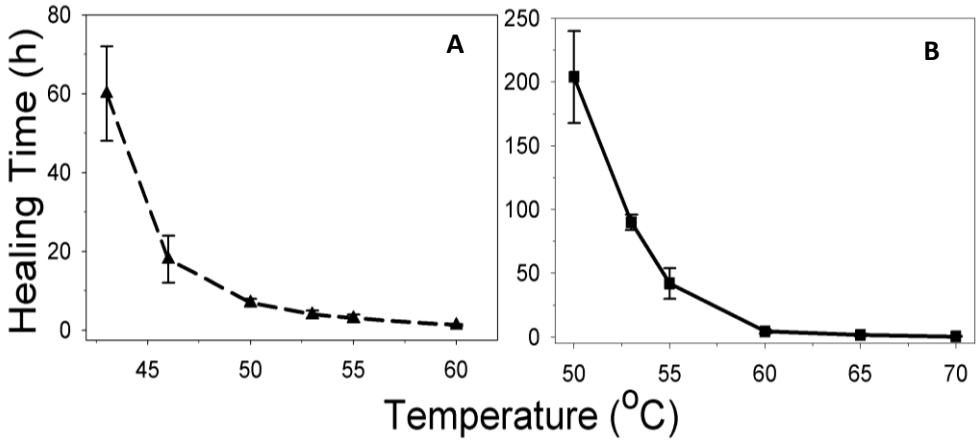

Figure 2-3: Effect of temperature on healing time of 5-µm pores on PLGA films incubated in *A*) PBST, and *B*) air (no hydration). $n = 3$, ± range.

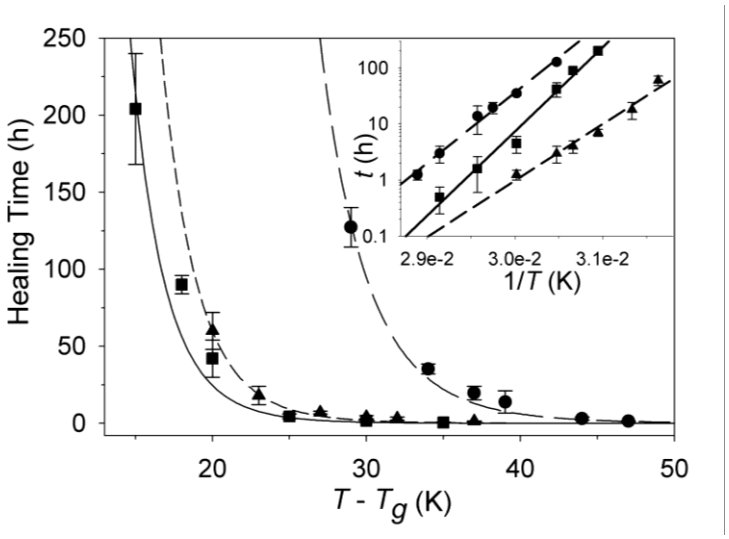

Figure 2-4: WLF describes healing time of 5-µm pores in lauryl ester-terminated PLGA incubated in PBST (▲) or dry (■) conditions, and carboxylic acid-terminated PLGA incubated dry (●). Data from Figure 2-3 was fitted by non-linear regression to WLF equation using $T_o = T_g$, C_1 = 17.4 K, and C_2 = 51.6 K. r^2 = .951 (ester-terminated dry), .993 (ester-terminated in PBST), and .981 (acid-terminated dry). Inset: Arrhenius plot of healing data. Resulting activation energies are 288 kJ/mol for dry incubation (r^2 = .985), 193 kJ/mol for incubation in PBST (r^2 = .973), and 240 kJ/mol for acid-capped PLGA incubated dry (r^2 = .991).

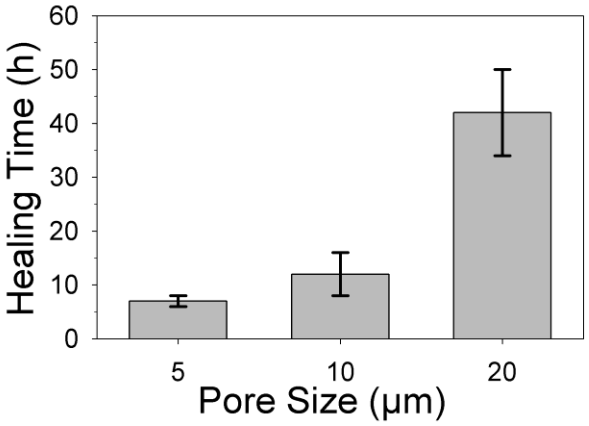

Figure 2-5: Healing time as a function of pore width under hydrated conditions at 50 °C. All pores were 7 µm deep. n = 3, ± range.

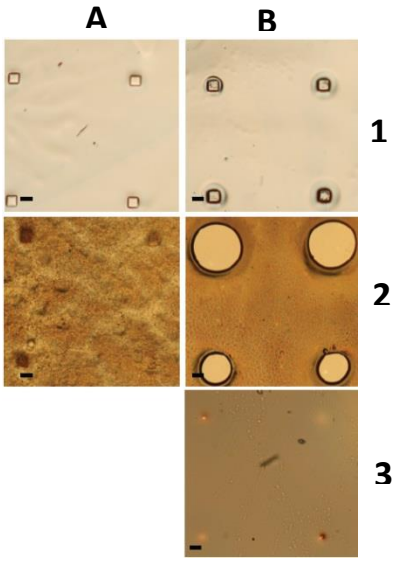

Figure 2-6: Light micrographs of microneedle-stamped PLGA pores (50 µm wide) after incubation. *A*) 7 µm deep. *B*) 15 µm deep. *1*) before incubation. *2*) after incubation in PBST. 3) after incubation in air. Scale = 50 µm.

2.9 Supplementary Information

2.9.1 Measurement of Surface Tension

The surface tensions of the PLGA films were determined by placing a drop of milliQ water on the films and using a goniometer to measure the polymer-water contact angle. Contact angles for each film were measured in three distinct locations, and a minimum of two samples were used for each set of conditions. The contact angles were used to calculate the tension, γ, following Berthelot's combining rule [35].

$$\gamma = (1+\cos\theta)^2 \gamma_{lv} / 4 \qquad (7)$$

where θ is the contact angle, and γ_{lv} is the surface tension of water.

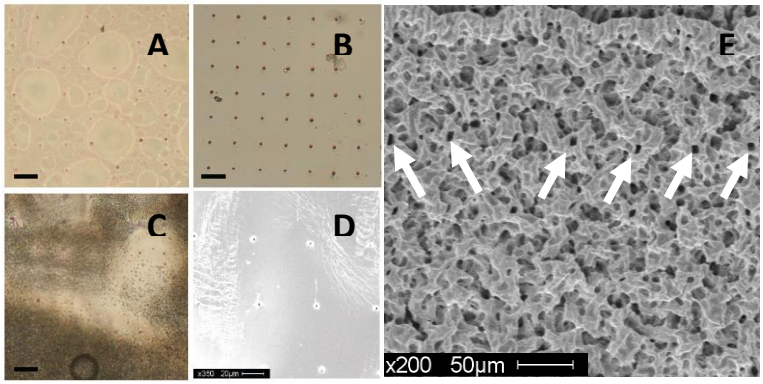

Supplementary Figure 2-1: Unhealed 5-µm pores after incubation in PBST. *A)* 1 week at 25 °C, *B)* 1 week at 5 °C, *C)* 2 weeks at 37 °C, *D)* SEM image of film in *C)*, provided due to obscurities on light micrograph, and *E)* SEM image of stamped acid-terminated PLGA film after incubation in PBST at 50 °C for 3 days, with unhealed square pores marked by arrows. Scale = 50 µm.

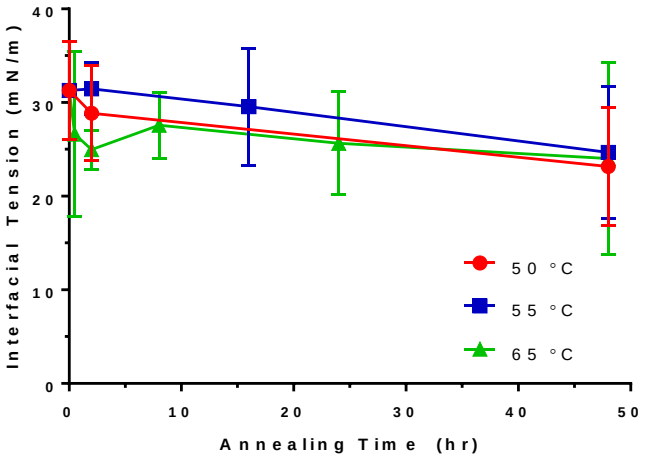

Supplementary Figure 2-2: Interfacial tension of PLGA films decreases with annealing time when incubated at various temperatures. *n* = 6, ± SEM.

Chapter 3: Active Self-Encapsulating PLGA Microparticles for Controlled Release of Vaccine Antigens

3.1 Abstract

Long-acting controlled release systems are an advantageous method of delivering biomacromolecules (*e.g.*, protein antigens/vaccines) as they reduce injection frequency, thus increasing patient compliance and overall coverage. However, the conventional controlled release strategy of encapsulating therapeutic agents into microparticles of poly(lactic-*co*-glycolic acid) (PLGA) is not well suited to proteins, as proteins are typically damaged by the encapsulation process. Presented here is the development of PLGA microparticles that can be remotely loaded from an aqueous protein solution – removing the protein from the emulsion procedure. This process, termed Active Self-Encapsulation, relies on a trapping agent to draw the protein into the microparticles where it is encapsulated by the healing of surface pores on the microparticles. By using the common vaccine adjuvant Alhydrogel as the trapping agent, a variety of different antigens were successfully encapsulated in the same microparticle formulation. This yielded high and reproducible antigen loading (1.6% *w/w* for the model antigen Ovalbumin), with encapsulation efficiencies over 90%. *In vitro*, these microparticles demonstrated biphasic controlled release of antigen over greater than one month. Initially, soluble antigen was released as antigen desorbed from Alhydrogel and diffused out of

the microparticles. Later, the microparticles physically degraded to release particulate antigen complexed to Alhydrogel. This technique is well suited to a variety of proteins and thus disease states. It could also offer the option for point-of-care compounding, where a hospital/pharmacy could maintain a stock of microparticles to be loaded *pro re nata* based on patient needs.

3.2 Introduction

Most modern vaccines are given on a schedule. These consist of a series of immunizations (shots) spread out over weeks to years (1). These schedules are necessary to fully develop protective immunity and/or maintain immunity that may fade over time. This necessity is largely due to a collective movement away from attenuated vaccines towards inactivated or purified options (2). While inactivated and purified vaccines are safer, they do not generate powerful immune responses, thus requiring more exposures to develop protective immunity. While such vaccines contain adjuvants that may increase the immune response, they do not develop any sort of infection. This allows them to be rapidly cleared. In general, if an insult can be rapidly overpowered, immunological memory does not develop as it is not required (2,3). While these scheduled doses are effective, they also present several caveats. First, they require multiple trips to a healthcare provider to receive the doses. In developed nations, this may only be an inconvenience to otherwise busy lives. In developing nations, however, this may require long travel times or not be feasible. More so, if an individual skips or misses a dose, they may not have the

protective immunity they think they do. Overall, vaccine schedules add cost, time, and the possibility of error to an otherwise critical piece of public health.

To overcome these challenges, researchers are developing single administration vaccines (4-7) that can be administered once and offer long-lasting protection. Most of these formulations contain some mechanism of controlled release where a depot holds or hides the antigen and slowly presents it to the immune system over time. These can be pulsatile to mimic the prime-booster paradigm already used (6,8,9), or continuous to better represent how an infection would naturally develop (10,11). Single-administration vaccines have the obvious advantage of only requiring a single administration to provide protective immunity – removing the possibility of missing a necessary booster dose. This makes the vaccine more convenient, and could help reduce cost and improve vaccine coverage world-wide. However, new research has shown that the kinetics of antigen presentation to the immune system may also determine the strength of response, and in this way continuous controlled release vaccines may be advantageous over repeat injections (12). For example, when a fixed dose of a meningitis antigen was administered to mice either as a single bolus dose, or spread out over several says, the “continuous” administration produced a more robust immune response. More so, an exponential increase in antigen generated the strongest response. The authors suspect that since this exponential increase best mimics a growing infection, and that is how evolution has told the immune system to expect a pathogen, the body is best prepared to provide a response (12).

While there are many methods researchers use to create controlled antigen release, a common practice is the encapsulation of antigens in a bioerodable polymer. Perhaps the most common of these polymers are poly(lactic-*co*-glycolic acids) (PLGAs), which are already used in a litany of FDA-approved devices for controlled release (13,14). Several reviews are available explaining the advantages and utility of such devices, which are too numerous to detail here (14-16). Typically, however, PLGAs are made into microparticles – small spheres ranging between roughly 1 and 100 μm in diameter. These microparticles contain the therapeutic mixed in somehow, and slowly release it through a variety of mechanisms (14,15). While PLGA microparticles have had great success encapsulating and releasing small molecule-based drugs, the technology has historically not translated well to large biomacromolecules such as protein antigens(13). The shear stresses, solvent interfaces, lyophilization, and often γ-irradiation used in the fabrication and sterilization of PLGA microparticles are too damaging to sensitive proteins (17-20). In one such study, after encapsulating Tetanus Toxoid (TT) protein inside PLGA microparticles, approximately 75% of the antigen was damaged as a result of the fabrication process (19).

To overcome the challenges of encapsulating proteins in PLGA microparticles, a new protein-loading paradigm has been set forth. Termed self-healing encapsulation, this strategy separates the fabrication of PLGA microparticles from the act of protein loading (19,21-23). That is, the microparticles are made without protein but with other excipients, and are

loaded remotely from an aqueous protein solution as a later step. This system relies on the dynamic pore behavior of PLGA microparticles (24). In brief, when microparticles are made via a w/o/w double emulsion, the inner-water phase forms a network of pores inside the hardened microparticles. If this inner-water phase contains more dissolved solutes than the outer-water phase, an osmotic imbalance exists, and the surface of the microparticle will yield, creating surface pores. Because proteins cannot penetrate the polymer, aqueous diffusion through these pore networks is typically the rate-limiting step early in the release, eventually switching to polymer erosion-limited processes later on. It was recently noticed that these pores are dynamic – closing and opening during *in vitro* release studies. Previous work shows this is a viscoelastic phenomenon driven by surface tension and resisted by viscosity (24,25). Furthermore, the pore morphology appears to correlate with release. When the pores are open, release is rapid, and when closed release is slow or non-existent (26). So, self-healing encapsulation utilizes the dynamic nature of these pores as a means of protein entrapment inside the microparticles. After fabricating porous microparticles, they are soaked in an aqueous protein solution. The proteins diffuse into the pores, and heat is applied to heal/close the pores, trapping the protein inside and effectively loading the microparticles. Because no external stresses other than mild heat are applied, the encapsulated protein is more stable than in conventional encapsulation methods (19). Also, by loading microparticles after they have been fabricated, it allows early formulation optimization to be performed without wasting protein and ensures

that only microparticles in the desired size range are loaded. Lastly, when these microparticles are then taken to release, the pores slowly reform and the polymer degrades, releasing the protein.

While this method is effective, it suffers from low encapsulation efficiencies. Also, to obtain high loading, very high concentrations of proteins are required. To improve upon this technique, Active Self-Encapsulation (ASE) was developed (19,21,23). Here, a trapping agent is added to draw the protein into the microparticles and sequester it there while the pores are healed. A schematic of this technique is outlined in Fig 3-1. The choice of trapping agent varies based on the protein to be encapsulated and the disease state being treated, but in the case of vaccine antigens, metal-based adjuvants are a promising choice as they are already used in approved vaccines and can effectively bind to many different antigens.

Presented here is a continuation of previous research utilizing the ASE loading strategy. PLGA microparticles are fabricated without protein present – containing only Alhydrogel, a common vaccine adjuvant, and trehalose as a stabilizing and pore-forming excipient. Shown here, however, is that these microparticles prove capable of loading a variety of model and clinical antigens without any changes to the microparticle formulation. The release behavior of these microparticles is also studied in greater detail. This vaccine delivery system could offer many advantages. Consider for example a healthcare center in a developing nation. It would now only need to store bulk quantities of

unloaded microparticles, which are considerably more shelf-stable than microparticles containing protein. These microparticles could then be loaded with different antigens on a case-by-case basis and offer full protective immunity from a single administration. Furthermore, this chapter lays the groundwork for the following chapter (Chapter 4), where these microparticles will be incorporated into microneedle designs for intradermal administration.

3.3 Materials & Methods

3.3.1 Materials

PLGA 50:50 (*i.v.* = 0.60 dL/g, *Mw* ≈ 55.4 kDa, ester terminated) was purchased from Lactel. Poly(vinyl alcohol) (PVA) (80% hydrolyzed, *Mw* = 9-10 kDa) and Ovalbumin (OVA) was purchased from Sigma Aldrich. Recombinant Hepatitis B surface antigen (rHBsAg) was from Arista Biologics. Recombinant protective antigen (rPA) was purchased from List Laboratories. F1-V antigen was from NIH BEI Resources. Alhydrogel 2% was from Invivogen. OVA-AlexaFluor 488 and OVA-AlexaFluor 647 was from Life Technologies. All chemicals were analytical grade or better.

3.3.2 Preparation of Active Self-Encapsulating PLGA Microparticles

Water-in-oil-in-water (w/o/w) double-emulsion porous PLGA microparticles were prepared via solvent evaporation adapting on methods previously reported (19). 350 mg PLGA was dissolved in 1 mL dichloromethane. The inner-water phase was prepared by concentrating Alhydrogel to 6.35% via centrifugation and removal of excess solution, then 8% *w/v* trehalose was added

and the slurry was mixed. 0.2 mL of the inner-water phase was added to 1 mL of the dissolved polymer phase, then homogenized for 1 minute at 17k rpm on a Tempest I.Q.^{2} Sentry Microprocessor. 2 mL of a 5% (*w/v*) PVA solution was then dumped into the PLGA and vortexed for 50 s. Lastly, the w/o/w emulsion was poured into 100 mL of a 0.5% (*w/v*) PVA solution and hardened under rapid stirring for 3 hours. The resulting microparticles were passed through a 60 µm and 10 µm sieve in series and washed with ddH_2O to remove excess PVA. The microparticles were then centrifuged (200 g, 5 min) to remove excess liquid, frozen by submersion in LN_2, and lyophilized for 48 h.

3.3.3 Scanning Electron Microscopy

Surface morphology of PLGA microparticles was evaluated by mounting dry microparticles on double-sided carbon tape and imaging on a FEI Quanta 3D scanning electron microscope (SEM) operated in low vacuum mode at voltages of 5 or 10 kV. Images were captured on EDAX® software.

3.3.4 Microsphere Size Analysis

In addition to verification via SEM, microparticle size and polydispersity was evaluated on a Malvern Mastersizer 2000. Roughly 10 mg of hydrated microspheres were resuspended in ddH_2O and added to the chamber filled with ddH_2O. The suspension was stirred at 3000 rpm, and 10 measurements were performed per sample at a sampling time of 15 s. Multiple records were taken at obscuration levels between 3 and 15% to ensure measurement stability and

that settling was not occurring. The dispersant and particle RI was 1.33 and 1.59, respectively.

3.3.5 Loading and Encapsulation Efficiency of Vaccine Antigens in ASE Microparticles

Active Self-Encapsulation of model and clinical vaccine antigens was modified from previously reported methods (19). Flocculated antigens (OVA & rPA) were resuspended at a stock concentration of 1 mg/mL in 10 mM MOPS buffer, pH 7.4. F1-V and rHBsAg were first buffer exchanged from PBS to MOPS using Microcon centrifugal filter devices with a 10K MWCO and following the provided guidelines, then brought to a 1 mg/mL stock in MOPS. Unless otherwise specified, 0.5 mL of 1 mg/mL antigen solution was added to 20 mg microparticles in a low protein-binding 0.5 mL microcentrifuge tube. The tube was protected from light and rotated for 2 d at 4 ˚C, 1 d at room temperature, and 2 d at 42 ˚C. After incubation the suspension was centrifuged for 5 min at 6010 rcf and the supernatant was removed and saved for analysis. The microparticle pellet was transferred to a 2 mL low protein-binding microcentrifuge tube and washed 3X with MOPS. Loading and encapsulation efficiencies (*EE%*) were determined using the following formulas using the lost mass of antigen from the loading solution compared against positive controls.

$$\%\ w/w \text{ loading: } \frac{mass\ of\ antigen\ encapsulated\ by\ microparticles}{mass\ of\ microparticles} \times 100$$

$$EE\%: \frac{mass\ of\ antigen\ encapsulated\ by\ microparticles}{initial\ mass\ of\ antigen\ in\ the\ loading\ solution} \times 100$$

3.3.6 Adsorption and Release of Antigens to and from Alhydrogel

To evaluate various antigens' abilities to adsorb and desorb from Alhydrogel, antigens were diluted to 400 µg/mL in 10 mM MOPS buffer. Alhydrogel was similarly diluted to 200 µg/mL (100 µg/mL for rHBsAg), and 1 mL each of antigen and Alhydrogel solutions were mixed and sent through a similar loading gamut as mentioned above. The samples were then spun down, the supernatant was collected and analyzed by HPLC and/or UPLC, and the samples were washed 3X with 1 mL MOPS before being sent to release at 37 ˚C in 1 mL PBST while shaking at 240 rpm.

3.3.7 Size Exclusion Chromatography of Antigens

Unless otherwise stated, antigen concentration was determined by size-exclusion chromatography (SEC) using either high or ultra performance liquid chromatography (HPLC/UPLC). In either case, the mobile phase consisted of PBS, pH 7.4, flowed at 1 mL/min (HPLC) or 0.4 mL/min (UPLC). Injection volumes were 50 or 10 µL for HPLC and UPLC, respectively. All samples were filtered through 0.45 µm filters prior to injection. A TSKgel G3000SWxl column was used for HPLC and an Acquity BEH SEC (4.6 X 150 mm) column was used for UPLC. UV detection was done at 215 nm. All samples were carried out in triplicate or greater.

3.3.8 Total Nitrogen Analysis

Total protein content was extrapolated from total nitrogen content using a modified automated Dumas technique (27). While this method was also used to

confirm microparticle loading, its primary utility was to determine the amount of protein remaining in a sample at various stages of release. Microparticle pellets were washed 3X with ddH_2O, then freeze-dried. 1 – 4 mg of microparticles were then massed into tin pans, which were crimped to remove excess air. Samples were run on a Leco TrueSpec® Micro CHN. The instrument was first blanked without samples to establish atmospheric baselines. Carbon, hydrogen, and nitrogen standards were then set in the anticipated range of nitrogen mass using USP grade EDTA. Lyophilized antigen standards were run to verify the percent nitrogen in the protein and set a Protein Factor. Microparticle samples were then dropped into the combustion chamber at 1050 ˚C, which converts all nitrogen to nitrogen gas, which is then quantified by a thermal conductivity cell. Protein content was determined by multiplying the nitrogen mass by the protein factor after first subtracting the nitrogen mass from negative controls (unloaded microparticles). Percent protein could then be determined by dividing protein mass by total sample mass.

3.3.7 Modulated Differential Scanning Calorimetry

Glass-transition temperatures (T_g) were determined by modulated differential scanning calorimetry (mDSC). For dry T_g, approximately 5 mg of lyophilized microparticles were crimped in aluminum pans with a non-hermetic lid. For hydrated T_g, samples were sent through the loading gamut mentioned in Section 3.3.5 (with or without antigen present), then excess solution was removed to create a slurry which was then transferred to aluminum pans

crimped with a hermetic lid. Temperatures were ramped between 5 ˚C and 80 ˚C at 3 ˚C/min, with a modulation amplitude of ± 1.0 ˚C/min and a period of 60 s. All samples were subjected to a heat/cool/heat cycle and the 2nd T_g was reported as the midpoint of the exothermic event. The analysis was done using TA Trios software, and all experiments were performed in triplicate.

3.3.8 *In vitro* Release of Soluble Antigen from Microparticles

After loading and washing, microparticles were resuspended in 1 mL PBST (PBS + 0.02% Tween 80), pH 7.4. The suspension was then shaken at 240 rpm at 37 ˚C while protected from light. At each timepoint (1, 3, 7 days and weekly thereafter), the microparticles were centrifuged 5 mins at 6010 rcf and the full release media was removed for SEC analysis and replaced with fresh PBST.

3.3.9 Distribution of Encapsulated Antigen within Microparticles and Evaluation of Particulate Release fraction

To visualize the distribution of antigen inside the microparticles after encapsulation, microparticles were loaded using an Ovalbumin-Alexa Fluor 647 conjugate (OVA-AF647) similar to as described above. After washing, the microparticles were resuspended in ddH_2O and placed on a glass slide with a coverslip and cross-sectional Z-stacked images were taken on a Nikon A-1 spectral confocal laser scanning microscope (CLSM) with NIS Elements viewing and analysis software.

To evaluate the particulate release fraction, OVA-AF647-loaded microparticles were resuspended in PBST and sent to release at 37 ˚C. At

predetermined time points, a sample of the suspension was removed and washed with ddH_2O before similarly imaging as above via CLSM. Images were compared against Alhydrogel that had similarly been loaded with OVA-AF647 and washed of unbound antigen.

3.4 Results and Discussion

3.4.1 Microparticle Fabrication and Physical/Thermal Characterization

The formulation parameters of the ASE PLGA microparticles were selected to produce spherical, porous microparticles within the desired size range (10 – 60 µm) that demonstrated self-healing when incubated in solution above T_g. After sieving and freeze-drying, approximately 70% of the formulation mass had been recovered. The microparticles were well formed and highly porous as observed via SEM (Fig 3-2A). While other formulations were attempted, they either did not result in well-formed and porous microparticles, or demonstrated inferior OVA loading. Of particular note, when the PLGA concentration was reduced to 250 mg/mL, a significant portion of the microparticles were malformed, and appeared to have collapsed, likely due to an inability to withstand the osmotic force created by the double emulsion (Supp. Fig 3-1). The hydrated microparticles had a volume-weighted mean diameter of 35.0 µm, with 80% of particles falling between 21.6 and 55.7 µm (Supp. Fig 3-2). This size is larger than the limit up to which professional phagocyte cells can internalize a particle (28). Thus, *in vivo,* any encapsulated

antigen will likely be hidden from the immune system until it is released from the microparticles.

One advantage of the ASE loading strategy is it allows formulation optimization to largely take place in the absence of protein. This reduces the amount of potentially expensive protein wasted during pilot studies to create microparticles. Thus, while 70% of the microparticles fell within the desired range, the excluded microparticles did not contain protein at this stage, further reducing waste and costs.

After incubation in the loading gamut, which included two days at 42 ˚C, self-healing of the surface pores was apparent (Fig 3-2B). This healing and rearrangement of the surface pores serves to trap some of the antigen-Alhydrogel complex inside the polymer, slowing release by closing the diffusion path out of the microparticles (19,21). While the microparticles are still porous, suggesting self-healing was not absolute, they appear mostly smooth with smaller pores. Previous research into self-healing suggested both that larger pores may not be capable of fully healing within a reasonable time-frame (24,25), and that the presence of Alhydrogel may partially hinder the self-healing process (19). Surface tension, which drives self-healing, falls during incubation above T_g, further slowing healing (25). This suggests that pores that do not heal early in the incubation may not be able to fully heal, regardless of incubation time or temperature, within reason. Additional loading gamuts were tested, including removing microparticles after two days at room temperature,

two days at 37 ˚C, or up to four days at 42 ˚C (Supp. Fig 3-3). Microparticles incubated at room temperature showed no change in surface morphology and remained buoyant – suggesting incomplete water-uptake. Microparticles incubated at 37 ˚C showed limited self-healing. This is consistent with previous work suggesting healing does not occur below T_g, and is slow in the few degrees above it (24). Microparticles incubated at 42 ˚C for four days had pronounced and significant healing, but like those incubated for two days at 42 ˚C, were also not fully healed. Four days at 42 ˚C was deemed too long and too damaging to be useful, so was not explored further. While complete self-healing was not observed with this formulation, it may be possible to promote it with the addition of hydrophobic plasticizers to the polymer phase to further drop T_g, as has been previously described (19).

The 2nd heating curve of mDSC thermographs indicated a T_g for the neat, lyophilized microparticles of 46.5 ˚C. This high T_g is ideal, as it suggests the microparticles are likely to be shelf-stable – not requiring refrigeration so long as care is taken to keep out moisture. Since the microparticles do not contain protein, it is reasonable to conclude that a healthcare provider could store them in such a manner. After hydration and loading, however, the T_g had fallen to 32.6 ˚C (Table 3-1). This is consistent with plasticization of the polymer by water, dropping the T_g (29), and further supports the aforementioned healing behavior. This T_g is also below physiologic temperature, so while the dry microparticles are shelf-stable, once resuspended they will degrade/release antigen (14).

3.4.2 Active Self-Encapsulation of Vaccine Antigens

To optimize loading conditions, OVA was used as a model antigen. Various antigen concentrations and sample volumes were added to a set mass of microparticles (20 mg) to maximize *w/w* loading % and encapsulation efficiency (Table 3-2). When the volume was maintained at 1000 µL and concentration was lowered, loading decreased significantly with concentration. But when concentration was maintained at 1000 µg/mL, the effect of decreasing volume on loading was much less pronounced. However, there was a significant effect on *EE%*. The two most optimal combinations were both at a concentration of 1000 µg/mL, and volumes of either 500 µL (which produced the best loading, 1.6% *w/w*) or 300 µL (which produced the best *EE%*, 90.7%). Thus, while one of the advantages of ASE is less wasted antigen, these studies suggest it is best to work with lower volumes than lower concentrations, but that there is versatility to change parameters depending on the importance of *EE%* or loading, which may change based on the antigen/disease of interest. It is believed that the increase in loading observed between 1000 µL and 500 µL (1 mg/mL each) is due to a change from a 2.0 mL microcentrifuge tube to a 0.6 mL option. This produced better mixing, and also limited the air-water interface. Microparticles at this interface may not load or heal properly, as has been previously observed (26). For future studies, the parameters producing the highest loading were selected (500 µL, 1000 µg/mL).

To test the effects of the loading gamut, microparticles were incubated at various temperatures ramps (Fig 3-3). All microparticles incubated at 42 ˚C with at least one prior day at lower temperatures had statistically significant loading of ~1.6% *w/w* regardless of additional time at 42 ˚C. Microparticles incubated only at 42 ˚C had slightly attenuated loading. Allowing the microparticles to incubate at lower temperatures allows time for the antigen to diffuse into the pores and bind Alhydrogel before the healing process begins. Microparticles incubated up to 37 ˚C had only slightly reduced loading, but also showed attenuated self-healing. Microparticles incubated only up to room temperature demonstrated significantly lower loading and showed no signs of self-healing. For future studies, microparticles were loaded using a temperature ramp of two days at 4 ˚C, one day at room temperature, and two days at 42 ˚C. Again, this demonstrates the versatility of the ASE approach. While higher temperatures are optimal, it is still possible to load the microparticles at lower temperatures if working with thermolabile antigens, or if heating instrumentation is not available. Furthermore, the ease with which it can be performed could allow it to be carried out directly at the point of care with minimal scientific supervision.

To visualize the distribution of antigen encapsulated in PLGA microparticles after ASE, microparticles were loaded with an Ovalbumin-AlexaFluor 488 conjugate (OVA-AF488). Cross-sectional images were taken to develop a Z-stacked image. Fig 3-4 shows a cross section image with orthogonal images alongside. This image confirms that the antigen is reasonably well

distributed throughout the microparticles. The smaller microparticles appear most homogeneous, suggesting uniform antigen distribution. The larger microparticles fluoresce most brightly towards their surface. This could be due to: *A*) inability of the antigen to diffuse deeply into the larger microparticle core, *B*) non-uniform distribution of Alhydrogel within the microparticles, or *C*) attenuation of laser strength and/or fluorophore emission through the thickest part of a dense opaque polymer material (30).

Multiple antigens were evaluated for their ability and capacity to load into the same microparticle formulation. Table 3-3 shows the loading capacity of OVA, rHBsAg, rPA, and F1-V into the microparticles, as well as their adsorption capacity to Alhydrogel. Also included was Tetanus Toxoid (TT), which was not evaluated here, but was previously shown to successfully load into ASE microparticles using a similar formulation (19). All antigens tested could be successfully loaded into the microparticles. The rPA and F1-V, however, were not thermostable, and required the addition of 20% *w/w* trehalose to the loading solution in order to stabilize the antigen during the loading gamut (Supp. Fig 3-4), as has been previously reported (31). While the addition of this excipient stabilized the antigen, it also interferes with loading. When 20% trehalose was added to OVA controls, loading was reduced by 45% (data not shown).

This data perhaps best demonstrates the vast potential of the ASE technique. Shown here are multiple antigens loading into the same

microparticle formulation. A different batch of microparticles need not be created for each antigen, as would be required of traditional encapsulation techniques. Instead, a bulk supply of unloaded microparticles was fabricated. These microparticles can be easily stored, and then aliquots of microparticles can be taken for loading as needed with whatever antigen is required without the need for specialized instrumentation or training. Because Alhydrogel, which is already included in many different vaccines, is used as the trapping agent, any antigen that can bind to Alhydrogel could be loaded into these microparticles. This offers great cost, time, and space saving opportunities, and could allow microparticle-based vaccines to reach a wider population than was previously practical.

3.4.3 Antigen Release from PLGA Microparticles

In vitro release of a model antigen, OVA, was observed to occur in two phases. Over the first 50 days, there is a controlled release of soluble OVA as detected in the release media via SEC (Fig 3-5). This includes roughly 50% of total encapsulated antigen released during the first day, an additional 20% over the first week, and approximately 5% released slowly over the following month or so. The general kinetics of this release matches closely with that of the freeze-dried inner-water phase (Alhydrogel + trehalose) and fresh/unprocessed Alhydrogel, except for a modest decrease in initial burst. This suggests that the fabrication process has likely not altered the native function of Alhydrogel.

The second phase of release is that of the Alhydrogel-antigen complex. In addition to electrostatic interactions, Alhydrogel is known to undergo ligand exchange with many phosphorylated antigens, including those tested here (32-36). The fraction of antigen that is ligand bound is generally not recoverable in the soluble form (32,37-39). Thus, this protein fraction releases from the microparticles as a particulate complex. The complex is difficult to accurately quantify and separate from the polymer, and additional research will be needed to confirm that this antigen is still antigenically active. However, to visualize the behavior of this complex, microparticles were again loaded with OVA-AF647. Fig 3-6A shows the small complexes created by co-incubation of Alhydrogel with OVA-AF647. Figures 6B-F show microparticles loaded with OVA-AF647 at various stages of release. Up through day 14, fluorescence is localized within the microparticles, which appear spherical and without obvious signs of physical degradation. At day 21, the microparticles begin to show signs of physical degradation, and what appears to be the Alhydrogel-OVA-AF647 complex begins to appear outside the microparticles. The degradation of the microparticles and subsequent release of the complex is even more pronounced at day 28. By day 42, intact microparticles are no longer visible, and the entire signal comes from these particulate complexes. This suggests that the complex is not able to escape the intact microparticles due to its particulate nature and large particle size (40). However, as the microparticles physically degrade, the complex is able to escape for presentation to the immune system. These results are further corroborated by SEM images of the microparticles taken at

equivalent timepoints (Fig 3-7). These images confirm that the microparticles maintain their spherical, intact shape through 14 days. At day 21, there are obvious signs of physical bulk degradation, and the surface morphology appears more smooth. Again, at day 28 the microparticles have lost most of their shape, while at day 42 microparticles no longer identifiable.

To verify that the mass of antigen released as a complex accounts for the remaining ~25% of antigen that does not release during the soluble phase, the microparticles were subjected to nitrogen analysis (Table 3-4). After 35 days of release, the microparticles (and any released complex) were spun down, washed with ddH_2O, and then lyophilized. The powder was mixed to ensure uniform distribution, and a sample was analyzed for nitrogen content against EDTA (standards), OVA (positive control), and unloaded microparticles also sent through 35 days of *in vitro* release testing (negative control). The PLGA and microparticle excipients do not contain nitrogen. Thus, any nitrogen signal (after subtracting negative controls) was assumed to be due to remaining protein either in the microparticles and/or released as a complex with Alhydrogel. While approximately 70% of OVA had released in the soluble form by day 35, nitrogen analysis determined the remaining microparticles contained 27% of the total encapsulated protein, thus accounting for 97% of total encapsulated protein. While this technique does not provide information about protein structure, it does support the conclusion that the antigen not released in the soluble phase is still inside the microparticles, and may be released as a complex with Alhydrogel.

Taken together, the soluble and particulate release data paints the full picture of how release occurs from these microparticles (Supp. Fig 3-5). First, there is a quick wave of soluble antigen released, which tapers off by the end of the first week or so. This release is caused by counter ions from the release media (in this case phosphate) outcompeting the antigen for binding sites on Alhydrogel. The soluble antigen then diffuses out of the polymer through the existing pore network, slowed somewhat by the partial healing of surface pores. The fraction of antigen that is ligand-bound to Alhydrogel remains inside the microparticles. Then, starting around the third week, the microparticles begin to physically degrade and fall apart, opening up larger pores through which the Alhydrogel-antigen complex can escape. The process concludes around week 6 when the microparticle is fully degraded.

It is important to note, however, that different antigens may have different ratios of electrostatic and ligand-exchange interactions with Alhydrogel. While 75% of OVA releases in the soluble phase, for the highly ligand-exchanging antigen rHBsAg (33) only 25% of encapsulated antigen was released in the soluble phase (Fig 3-8). There, the release curve of soluble antigen from Alhydrogel, freeze-dried inner-water phase, and the microparticles, is shifted down approximately 50%, respectively. The same general release kinetics apply as the microparticles behave the same regardless of the antigen.

It is known that the kinetics of antigen presentation to the immune system greatly influence the resulting immune response (12). It is in this way that that

the system presented here would be expected to outcompete soluble antigen or Alhydrogel-complexed antigen alone. The soluble antigen released may begin to prime the immune system, while the microparticles hide the remaining antigen from the immune system until they degrade and release the remaining complex. This should generate a stronger immune response than presenting all the antigen at once, as is done with conventional vaccination.

3.5 Conclusions

The microparticle system explored here is a useful alternative to conventional approaches for loading vaccine antigens inside PLGA microparticles for controlled release. Using the Active Self-Encapsulation method, high loading of both model and clinical antigens was achieved (up to 2.3% *w/w*), along with encapsulation efficiencies of up to 90%. This work is distinct from previous results (19) in that it more fully evaluated the ability of the system to work with multiple antigens, and better characterized release through both the soluble and particulate/complexed phase. Using this system, researchers can create and optimize microparticles without needing to include potentially expensive antigens, and then test the design first using inexpensive model antigens before using clinical options. This could also allow a healthcare provider to store bulk quantities of a single microparticle supply, and then load with different antigens on a case-by-case basis without requiring special equipment. Similarly, by using the common vaccine adjuvant Alhydrogel as a trapping agent, any antigen that will bind to Alhydrogel can be loaded into the

same microparticles, as shown here with OVA, rHBsAg, rPA, F1-V, and previously TT. After incubation, the antigen-Alhydrogel complexes are well distributed throughout the microparticles. *In vitro* testing revealed a biphasic release mechanism. First, there is a quick release of soluble antigen that occurs mostly over one week, but may extend out longer. Later, the remaining ligand-bound fraction of antigen releases as a complex only after the microparticles have substantially physically degraded (starting at approximately three weeks). By slowly exposing the antigen to the immune system, not only may a stronger immune response be generated, but it may also decrease reliance on booster doses needed to achieve protective immunity. This has the potential to reduce vaccination costs and improve vaccine coverage worldwide.

3.6 References

1. CDC. Immunization Schedules 2016 [updated 2/1/2016; cited 2016]. Available from: http://www.cdc.gov/vaccines/schedules/
2. David Salisbury KN, Mary Ramsay. Immunisation against infectious disease. Department of Health, Social Services and Public Saftey. 2006.
3. Murphy K, Travers P, Walport M, Janeway C. Janeway's immunobiology. 7th ed. New York: Garland Science; 2008. xxi, 887 p. p.
4. Lofthouse S. Immunological aspects of controlled antigen delivery. Advanced drug delivery reviews. 2002;54(6):863-70. Epub 2002/10/05. PubMed PMID: 12363435.
5. Oyston P, Robinson K. The current challenges for vaccine development. Journal of medical microbiology. 2012;61(Pt 7):889-94. Epub 2012/02/11. doi: 10.1099/jmm.0.039180-0. PubMed PMID: 22322337.
6. Cleland JL. Single-administration vaccines: controlled-release technology to mimic repeated immunizations. Trends in biotechnology. 1999;17(1):25-9. Epub 1999/03/31. PubMed PMID: 10098275.
7. Jain S, O'Hagan DT, Singh M. The long-term potential of biodegradable poly(lactide-co-glycolide) microparticles as the next-generation vaccine adjuvant. Expert review of vaccines. 2011;10(12):1731-42. Epub 2011/11/17. doi: 10.1586/erv.11.126. PubMed PMID: 22085176.
8. Michael Cardamone SL, Jane Lucas, Rogan Lee, Michael O'Donoghue, Mal Brandon. In vitro testing of a pulsatile delivery system and its in vivo application for immunisation against tetanus toxoid. Journal of Controlled Release. 1997;47:205-19.
9. Sanchez A, Gupta RK, Alonso MJ, Siber GR, Langer R. Pulsed controlled-release system for potential use in vaccine delivery. Journal of pharmaceutical sciences. 1996;85(6):547-52. doi: Doi 10.1021/Js960069y. PubMed PMID: ISI:A1996UP54100001.
10. Preis I, Langer RS. A single-step immunization by sustained antigen release. Journal of immunological methods. 1979;28(1-2):193-7. Epub 1979/01/01. PubMed PMID: 469267.
11. Manish M, Rahi A, Kaur M, Bhatnagar R, Singh S. A single-dose PLGA encapsulated protective antigen domain 4 nanoformulation protects mice against Bacillus anthracis spore challenge. PloS one. 2013;8(4):e61885. Epub 2013/05/03. doi: 10.1371/journal.pone.0061885. PubMed PMID: 23637922; PMCID: 3639271.
12. Johansen P, Storni T, Rettig L, Qiu Z, Der-Sarkissian A, Smith KA, Manolova V, Lang KS, Senti G, Mullhaupt B, Gerlach T, Speck RF, Bot A, Kundig TM. Antigen kinetics determines immune reactivity. Proceedings of the National Academy of Sciences of the United States of America. 2008;105(13):5189-94. Epub 2008/03/26. doi: 10.1073/pnas.0706296105. PubMed PMID: 18362362; PMCID: 2278203.
13. Schwendeman SPC, H.R., Gupta RK, Langer R. Peptide, Protein, and Vaccine Delivery from Implantable Polymeric Systems Progress and Challenges. In: Society TAC, editor. Controlled Drug Delivery1997. p. 229-67.
14. Wischke C, Schwendeman SP. Degradable Polymeric Carriers for Parenteral Controlled Drug Delivery. Adv Del Sci Technol. 2012:171-228. doi: Doi 10.1007/978-1-4614-0881-9_8. PubMed PMID: ISI:000302879700008.
15. Wischke C, Schwendeman SP. Principles of encapsulating hydrophobic drugs in PLA/PLGA microparticles. International journal of pharmaceutics. 2008;364(2):298-327. Epub 2008/07/16. doi: 10.1016/j.ijpharm.2008.04.042. PubMed PMID: 18621492.
16. Uhrich KE, Cannizzaro SM, Langer RS, Shakesheff KM. Polymeric systems for controlled drug release. Chemical reviews. 1999;99(11):3181-98. Epub 2001/12/26. PubMed PMID: 11749514.
17. Maa YF, Hsu CC. Protein denaturation by combined effect of shear and air-liquid interface. Biotechnology and bioengineering. 1997;54(6):503-12. Epub 1997/06/20. doi: 10.1002/(SICI)1097-0290(19970620)54:6<503::AID-BIT1>3.0.CO;2-N. PubMed PMID: 18636406.
18. Sah H. Protein behavior at the water/methylene chloride interface. Journal of pharmaceutical sciences. 1999;88(12):1320-5. Epub 1999/12/10. PubMed PMID: 10585229.
19. Desai KG, Schwendeman SP. Active self-healing encapsulation of vaccine antigens in PLGA microspheres. Journal of controlled release : official journal of the Controlled Release Society. 2013;165(1):62-74. Epub 2012/10/30. doi: 10.1016/j.jconrel.2012.10.012. PubMed PMID: 23103983.

20. Desai KG, Kadous S, Schwendeman SP. Gamma Irradiation of Active Self-Healing PLGA Microspheres for Efficient Aqueous Encapsulation of Vaccine Antigens. Pharmaceutical research. 2013. Epub 2013/03/22. doi: 10.1007/s11095-013-1019-2. PubMed PMID: 23515830.
21. Reinhold SE, Desai KG, Zhang L, Olsen KF, Schwendeman SP. Self-healing microencapsulation of biomacromolecules without organic solvents. Angew Chem Int Ed Engl. 2012;51(43):10800-3. Epub 2012/09/27. doi: 10.1002/anie.201206387. PubMed PMID: 23011773.
22. Reinhold SE, Schwendeman SP. Effect of Polymer Porosity on Aqueous Self-Healing Encapsulation of Proteins in PLGA Microspheres. Macromolecular bioscience. 2013;13(12):1700-10. Epub 2013/11/29. doi: 10.1002/mabi.201300323. PubMed PMID: 24285573.
23. Shah RB, Schwendeman SP. A biomimetic approach to active self-microencapsulation of proteins in PLGA. Journal of controlled release : official journal of the Controlled Release Society. 2014;196:60-70. Epub 2014/09/16. doi: 10.1016/j.jconrel.2014.08.029. PubMed PMID: 25219750; PMCID: 4268178.
24. Mazzara JM, Balagna MA, Thouless MD, Schwendeman SP. Healing kinetics of microneedle-formed pores in PLGA films. Journal of controlled release : official journal of the Controlled Release Society. 2013;171(2):172-7. Epub 2013/07/09. doi: 10.1016/j.jconrel.2013.06.035. PubMed PMID: 23831588.
25. Huang J, Mazzara JM, Schwendeman SP, Thouless MD. Self-healing of pores in PLGAs. Journal of controlled release : official journal of the Controlled Release Society. 2015;206:20-9. Epub 2015/02/24. doi: 10.1016/j.jconrel.2015.02.025. PubMed PMID: 25701611.
26. Wang J, Wang BM, Schwendeman SP. Characterization of the initial burst release of a model peptide from poly(D,L-lactide-co-glycolide) microspheres. Journal of controlled release : official journal of the Controlled Release Society. 2002;82(2-3):289-307. Epub 2002/08/15. PubMed PMID: 12175744.
27. Etheridge RD, Pesti GM, Foster EH. A comparison of nitrogen values obtained utilizing the Kjeldahl nitrogen and Dumas combustion methodologies (Leco CNS 2000) on samples typical of an animal nutrition analytical laboratory. Anim Feed Sci Tech. 1998;73(1-2):21-8. doi: Doi 10.1016/S0377-8401(98)00136-9. PubMed PMID: ISI:000074723800002.
28. Champion JA, Walker A, Mitragotri S. Role of particle size in phagocytosis of polymeric microspheres. Pharmaceutical research. 2008;25(8):1815-21. Epub 2008/04/01. doi: 10.1007/s11095-008-9562-y. PubMed PMID: 18373181; PMCID: 2793372.
29. Blasi P, D'Souza SS, Selmin F, DeLuca PP. Plasticizing effect of water on poly(lactide-co-glycolide). Journal of controlled release : official journal of the Controlled Release Society. 2005;108(1):1-9. Epub 2005/08/16. doi: 10.1016/j.jconrel.2005.07.009. PubMed PMID: 16098624.
30. Stanciu SG, Stanciu GA, Coltuc D. Compensating Light Intensity Attenuation in Confocal Scanning Laser Microscopy by Histogram Modeling Methods. In: Stanciu SG, editor. Digital Image PRocessing: InTech; 2012 p. 187-200.
31. Jiang G, Joshi SB, Peek LJ, Brandau DT, Huang J, Ferriter MS, Woodley WD, Ford BM, Mar KD, Mikszta JA, Hwang CR, Ulrich R, Harvey NG, Middaugh CR, Sullivan VJ. Anthrax vaccine powder formulations for nasal mucosal delivery. Journal of pharmaceutical sciences. 2006;95(1):80-96. Epub 2005/11/30. doi: 10.1002/jps.20484. PubMed PMID: 16315230.
32. Morefield GL, Jiang D, Romero-Mendez IZ, Geahlen RL, Hogenesch H, Hem SL. Effect of phosphorylation of ovalbumin on adsorption by aluminum-containing adjuvants and elution upon exposure to interstitial fluid. Vaccine. 2005;23(12):1502-6. Epub 2005/01/27. doi: 10.1016/j.vaccine.2004.08.048. PubMed PMID: 15670886.
33. Iyer S, Robinett RS, HogenEsch H, Hem SL. Mechanism of adsorption of hepatitis B surface antigen by aluminum hydroxide adjuvant. Vaccine. 2004;22(11-12):1475-9. Epub 2004/04/06. doi: 10.1016/j.vaccine.2003.10.023. PubMed PMID: 15063571.
34. Jendrek S, Little SF, Hem S, Mitra G, Giardina S. Evaluation of the compatibility of a second generation recombinant anthrax vaccine with aluminum-containing adjuvants. Vaccine. 2003;21(21-22):3011-8. Epub 2003/06/12. PubMed PMID: 12798645.
35. Lindblad EB, Schonberg NE. Aluminum adjuvants: preparation, application, dosage, and formulation with antigen. Methods Mol Biol. 2010;626:41-58. Epub 2010/01/26. doi: 10.1007/978-1-60761-585-9_4. PubMed PMID: 20099120.
36. Wagner L, Verma A, Meade BD, Reiter K, Narum DL, Brady RA, Little SF, Burns DL. Structural and immunological analysis of anthrax recombinant protective antigen adsorbed to aluminum hydroxide adjuvant. Clinical and vaccine immunology : CVI. 2012;19(9):1465-73. Epub 2012/07/21. doi: 10.1128/CVI.00174-12. PubMed PMID: 22815152; PMCID: 3428410.

37. Rinella JV, White JL, Hem SL. Effect of Anions on Model Aluminum-Adjucant-Containing Vaccines. Journal of colloid and interface science. 1995;172:121-30.
38. Rinella JV, White JL, Hem SL. Effect of pH on the Elution of Model Antigens from Aluminum-Containing Adjuvants. Journal of colloid and interface science. 1998;205(1):161-5. Epub 1998/12/16. doi: 10.1006/jcis.1998.5648. PubMed PMID: 9710509.
39. Iyer V, Liyanage MR, Shoji Y, Chichester JA, Jones RM, Yusibov V, Joshi SB, Middaugh CR. Formulation development of a plant-derived H1N1 influenza vaccine containing purified recombinant hemagglutinin antigen. Human vaccines & immunotherapeutics. 2012;8(4):453-64. Epub 2012/03/01. doi: 10.4161/hv.19106. PubMed PMID: 22370514.
40. Shirodkar S, Hutchinson RL, Perry DL, White JL, Hem SL. Aluminum compounds used as adjuvants in vaccines. Pharmaceutical research. 1990;7(12):1282-8. Epub 1990/12/01. PubMed PMID: 2095567.

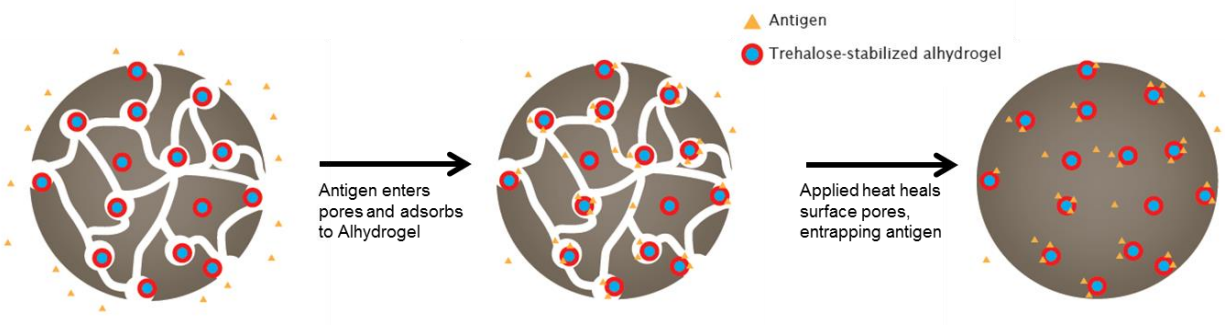

Figure 3-1: Schematic of Active Self-Encapsulation loading method. Porous microparticles containing trehalose-stabilized Alhydrogel are fabricated and freeze-dried. Microparticles are soaked in an antigen solution, antigen enters the pores and adsorbs to Alhydrogel. The solution is then mildly heated, healing the pores and entrapping the antigen. Microparticles can then be collected, washed, and utilized.

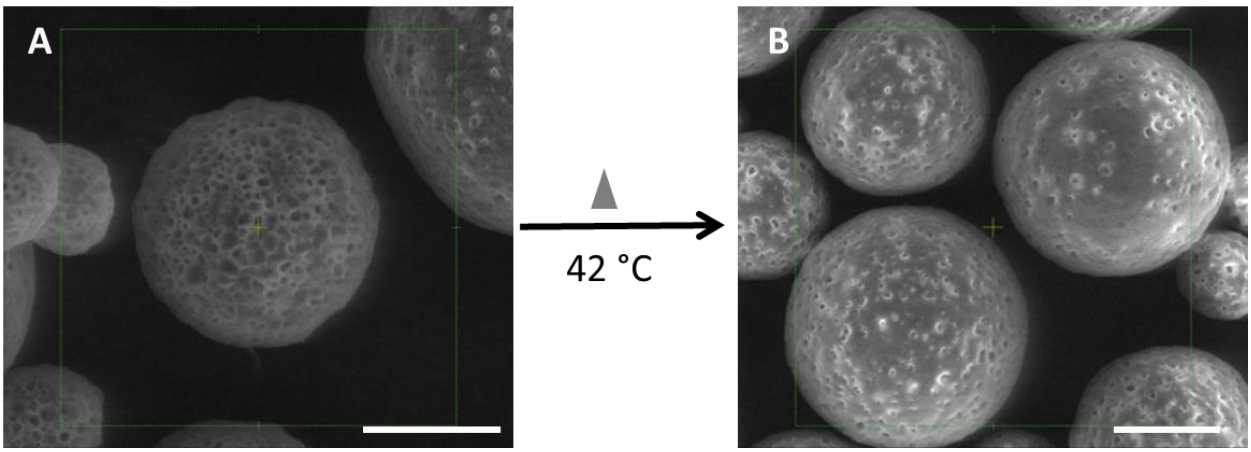

Figure 3-2: Porous PLGA microparticles self-heal under mild heat. *A*) Porous microparticles after fabrication and lyophilization. *B*) Partially self-healed microparticles after full loading/healing gamut (primarily two days at 42 °C).

2nd mDSC Heat	T_g (°C) ± SEM
Neat Microparticles	46.5° ± 0.0
Loaded, Hydrated	32.6° ± 0.2

Table 3-1: T_g of unloaded lyophilized microparticles, and of loaded and hydrated microparticles. The T_g of neat microparticles is above typical ambient temperatures, while the hydrated T_g is below physiologic temperatures. n = 3

Vol' (µL)	Conc' (µg/mL)	Loading %	*EE%*
1000	250	0.88 (.00)	75.4 (.0)
1000	500	1.01 (.01)	47.9 (.0)
1000	1000	1.50 (.01)	30.8 (.0)
500	*1000*	*1.64 (.03)*	*66.5 (1.4)*
300	1000	1.34 (.02)	90.7 (1.6)

Table 3-2: Loading % and *EE%* can be tailored based on loading conditions. Low volumes of higher concentrations perform better than high volumes of lower concentrations. (SEM)

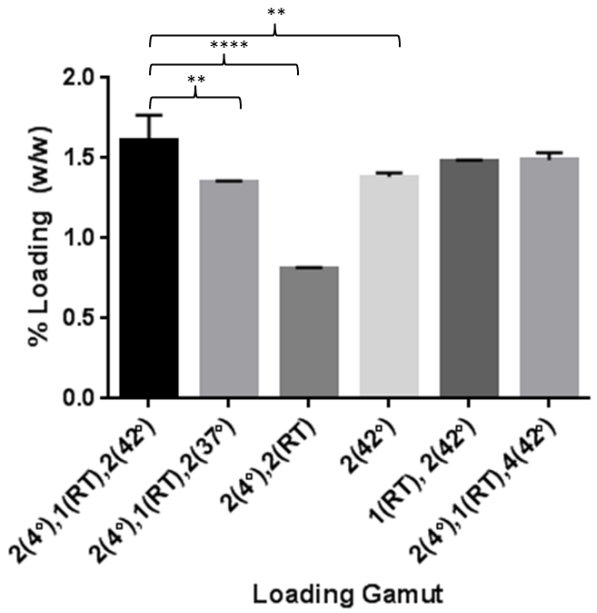

Figure 3-3: Changes to the loading gamut influence *w/w* loading. Hotter incubations yield higher loading, but additional time has no effect. ** p<.01, **** p<.0001

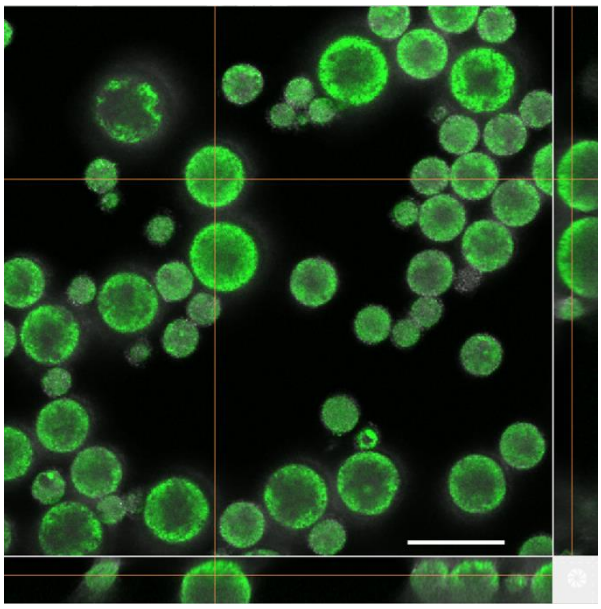

Figure 3-4: Active self-encapsulation results in thorough antigen distribution throughout the microparticles. Microparticles were loaded with OVA-AF488. Scale = 100 µm.

Antigen	Loading % (*w/w*)	Adsorption Capacity (mg/mg)
OVA	1.64 (.03)	1.25 (.02)
rHBsAg	2.25 (.11)	2.66 (.29)
rPA	0.90* (.02)	1.21* (.05)
F1-V	0.83* (.14)	0.81* (.06)
TT[a]	1.38[a] (.20)	N/A

Table 3-3: Multiple antigens can load into the same microparticle formulation using the ASE technique. *20% trehalose added to the loading solution. [a]data from Ref (19). (SEM)

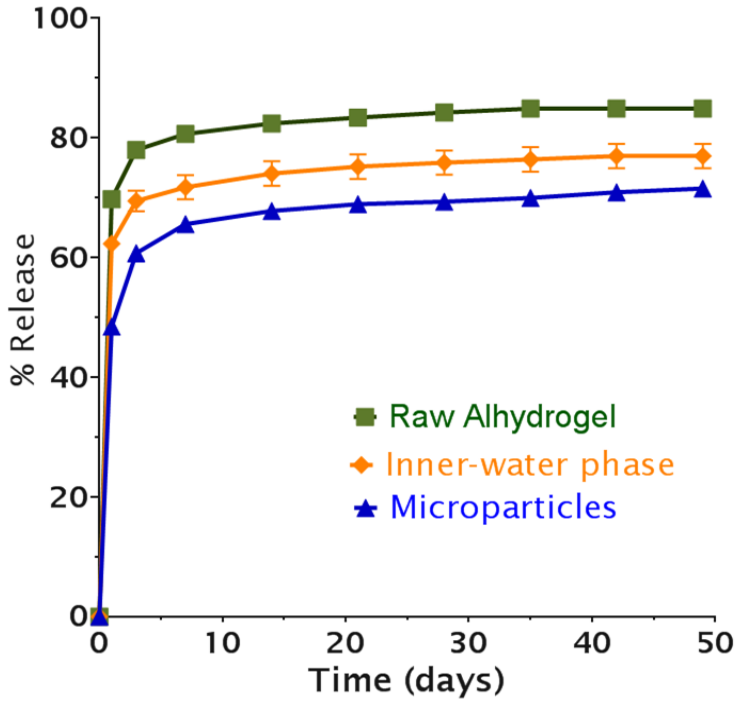

Figure 3-5: Controlled release of soluble OVA from ASE microparticles mimics the kinetics of antigen desorption from Alhydrogel. *n* = 3, ± SEM.

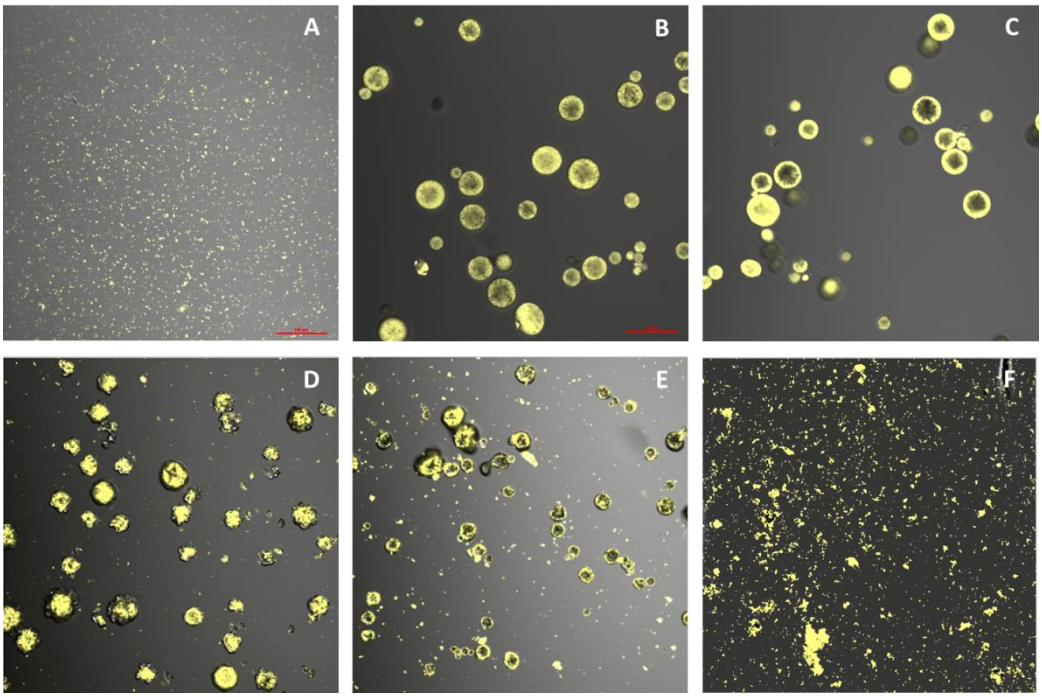

Figure 3-6: Release of Alhydrogel-OVA-AF647 complex from ASE microparticles. *A*) Alhydrogel-OVA-AF647 complex. OVA-AF647-loaded ASE microparticles after, *B*) 7 d, *C*) 14 d, *D*) 21 d, *E*) 28 d, and *F*) 42 d of *in vitro* release at 37 °C. Scale = 100 µm.

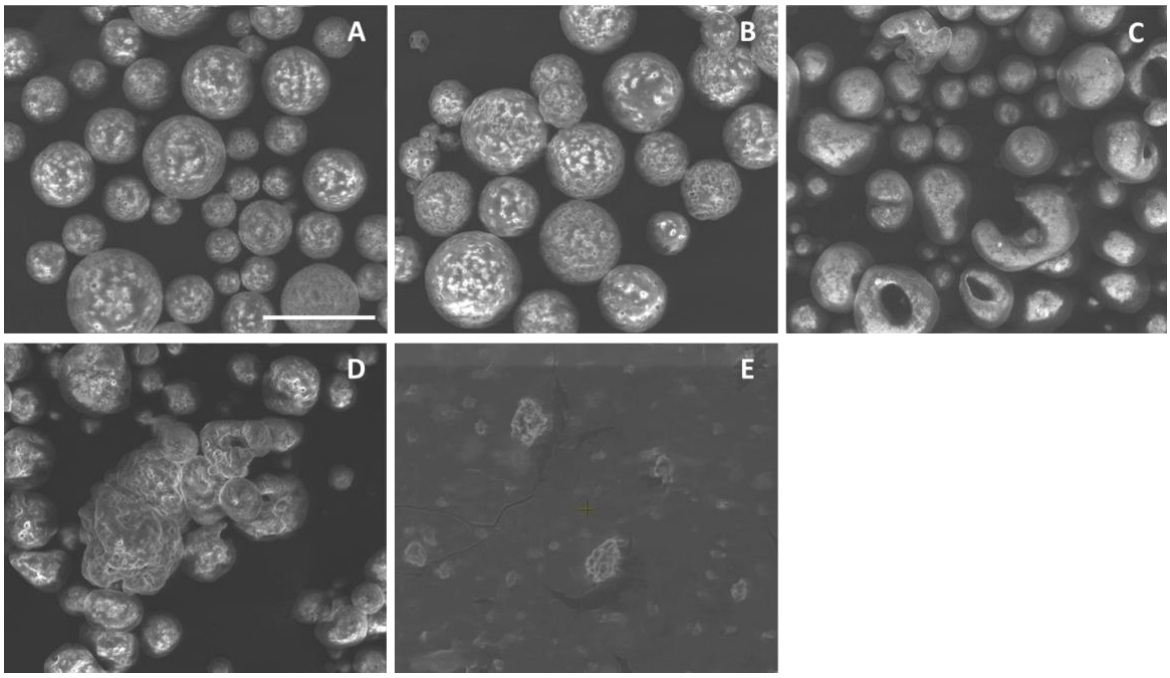

Figure 3-7: ASE microparticles slowly degrade during *in vitro* release at 37 °C, with significant degradation not apparent until 21 days. Electron micrographs of microparticles after *A*) 7 d, *B*) 14 d, *C*) 21 d, *D*) 28 d, and *E*) 42 d in release. Scale = 50 µm.

% Soluble OVA Released (d 35)	% Remaining (N_2 Analysis)	Total OVA recovery
69.9% (.0)	26.9% (.0)	96.8% (3.5)

Table 3-4: The fraction of antigen not released from ASE microparticles during the soluble release phase can be accounted for via nitrogen analysis. Approximately 70% of encapsulated OVA was released as soluble antigen by day 35. The remaining sample's mass was found to contain approximately 27% of total encapsulated OVA, for 97% total recovery. (SEM)

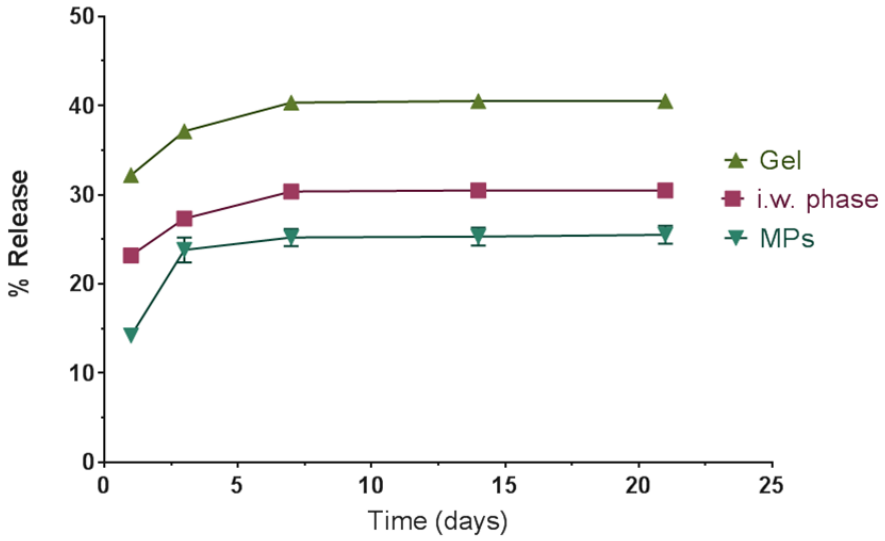

Figure 3-8: Controlled release of soluble rHBsAg from ASE microparticles, freeze-dried inner-water phase, and raw Alhydrogel. *n* = 3, ± SEM.

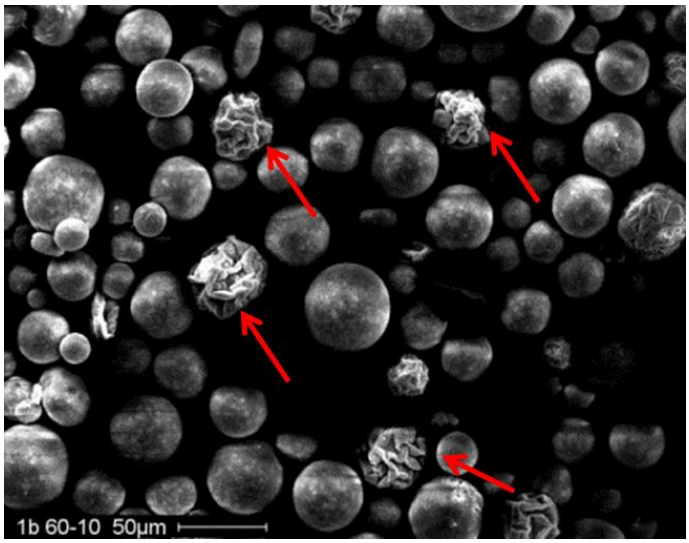

Supplementary Figure 3-1: Osmotically collapsed microparticles formed using a 250 mg/mL polymer concentration.

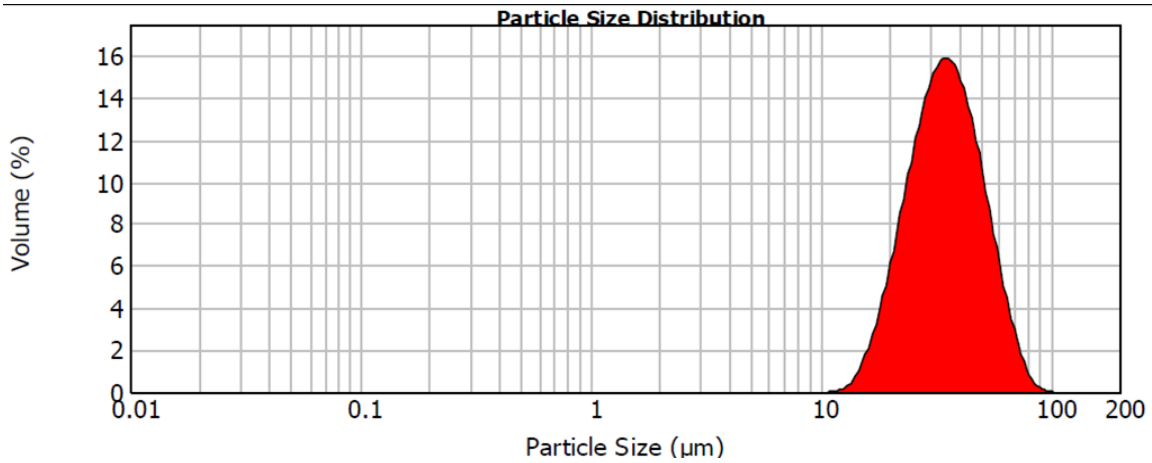

Supplementary Figure 3-2: Microparticle size distribution. Hydrated microparticles had a volume weighted mean diameter of 34.95 µm, with 80% of particles falling between 21.58 and 55.67 µm. Specific surface area = 0.184 m^2/g. Surface weighted mean = 32.57 µm.

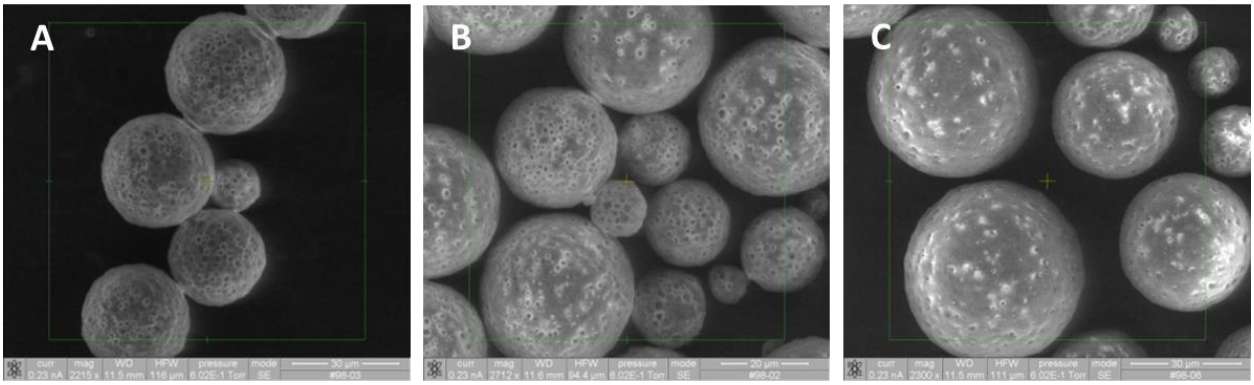

Supplementary Figure 3-3: Microparticles do not heal when incubated at room temperature for 2 d (*A*), show minimal healing after 2 d at 37 °C (*B*), and are not considerably more healed after 4 d at 42 °C (*C*) than after 2 d at 42 °C (Figure 3-2B).

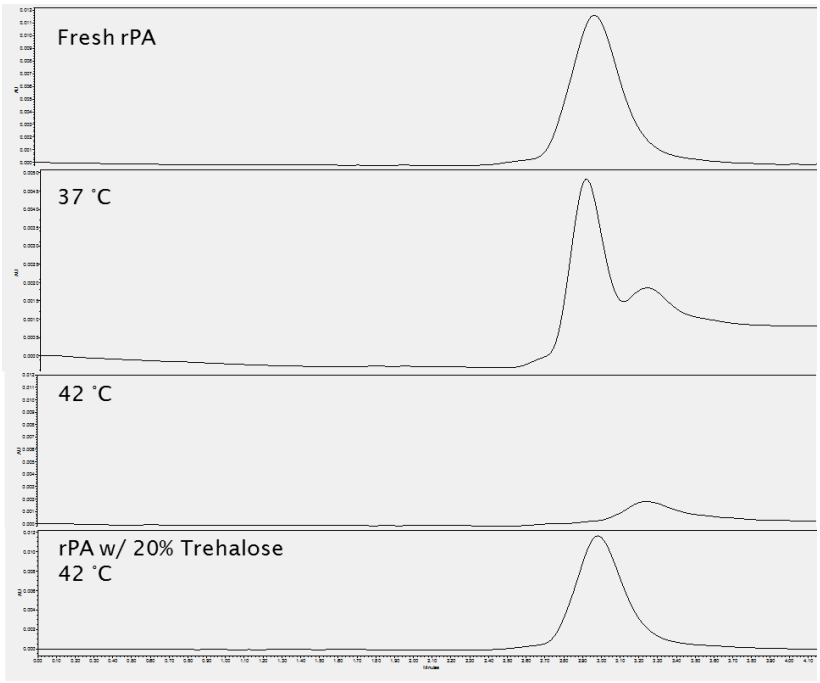

Supplementary Figure 3-4: Stabilization of rPA at 42 °C by the addition of 20% *w/v* trehalose.

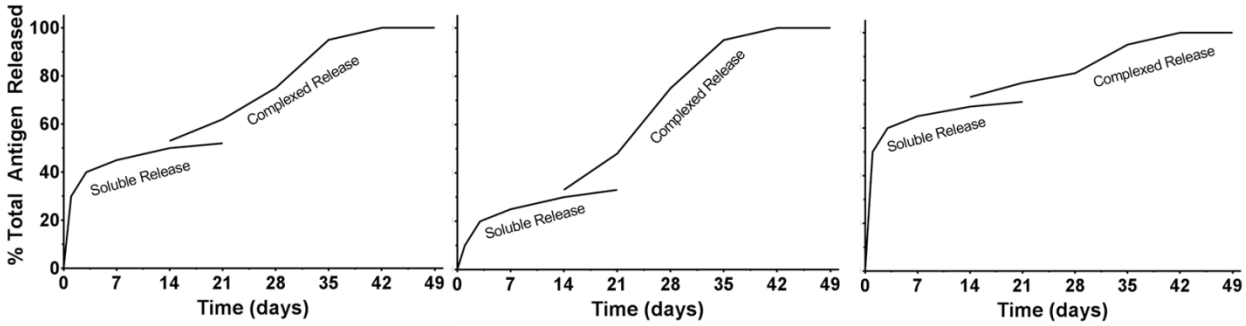

Supplementary Figure 3-5: Schematic of biphasic release from ASE microparticles. There is an initial burst (prime) of soluble antigen released as electrostatically adsorbed antigen desorbs and diffuses out of the microparticles. This is followed later (boost) by release of ligand-bound antigen-Alhydrogel complex that releases only once physical bulk degradation of the microparticles begins. The ratio of soluble to complex release will vary between antigens, depending on their binding mechanisms to Alhydrogel.

Chapter 4: Microparticle-based Microneedle Patches for Intradermal Vaccination

4.1 Abstract

Intradermal delivery is an attractive route for vaccine administration due to the skin's potent immune system. However, it is seldom used due to difficulties with precise intradermal administration.. Microneedles are a promising alternative to conventional hypodermic needles, and are specifically designed to deliver therapies into the skin. They cause little pain, can be self-administered, and are easy to store/dispose. Presented here are proof-of-concept studies utilizing microneedles to intraderamally deliver controlled release polymer microparticles loaded with vaccine antigens. By adding controlled release, it is possible to improve the immune response and reduce reliance on booster doses. These microparticles can load a variety of antigens, and demonstrate *in vitro* controlled release over greater than one month. Using a casting system, antigen-loaded microparticles were loaded into soluble microneedle patches, with the microneedles resting on pedestals to improve delivery. Each patch contained 204 μg of microparticles, which for the model antigen Ovalbumin corresponds to 3.4 μg of antigen. These microneedles readily penetrated excised porcine skin, and delivered >50% of their payload during a 20 minute application. Histologic cross-sections confirmed localization

of microparticles in the dermis after application, and retention at the site of application for over one week. The resulting wounds resealed over 2-4 days. When used to vaccinate mice, the patches and injected microparticles generated a robust antibody response that was as good as or better than conventional administration techniques, but without the need for a hypodermic injection. These studies show that microparticle-based microneedles have potential as a future self-applied, single-dose vaccine delivery system.

4.2 Introduction

Vaccines are generally considered to be the greatest medical advancement in human history. And while they have improved worldwide public health immensely, many hurdles remain. For example, in 2014 an estimated 18.7 million infants did not receive basic vaccines (1). Even in the United States, annual influenza coverage struggles to reach 50% (2), with other readily-available vaccines fairing much worse. Increasing vaccine coverage is likely to be one of the most effective means available for preventing a massive public health emergency such as the 1918 influenza outbreak that killed nearly 5% of the world's population (3).

There are many factors that might lead an individual to not receive their shots. Additionally, there is much that could be done by scientists to improve the efficacy of current vaccines. In the research presented here, a new vaccine delivery system is developed that attempts to overcome many of these limitations, which is outlined below.

A critical and often overlooked limitation of modern vaccines is their reliance on hypodermic needles. Vaccines are complex biomacromolecules that need to be presented to the immune system, and as such they generally cannot be dosed orally. As a result they are often loaded into hypodermic needles for intramuscular (i.m.) injection. Logistically, hypodermic needles present several issues. They are large, sharp, and sterile, and so require considerable space and are difficult to store. Pre-filled syringes must often be kept refrigerated, further limiting storage abilities. Otherwise, a healthcare provider must manually fill a syringe, which is time consuming and presents the possibility of error. Furthermore, after administration used needles are a serious health risk and must be disposed of as costly biohazardous waste. Lastly, administration of most shots must be done by a healthcare provider. The inability to self-administer presents numerous shortcomings, both to busy individuals whom might not take the time to get their shots, as well as to developing nations where the nearest healthcare provider may be very far from the home. Taken together, these logistical components of storage, transport, disposal, and staff time for administration represent 80% of the cost of vaccination campaigns (4). Moreover, there are many aspects that make hypodermic needles disliked by patients. The pain, possibility of blood, and needle-phobia are real considerations that prevent some patients from finishing vaccine schedules (5-7). Finally, from an immunology point-of-view, the intramuscular administration route is less than ideal. Muscle has a low resident population of professional phagocytes and antigen presenting cells, which are needed to

induce immunological memory (4). A more attractive route for immunization is by intradermal (i.d.) injection (4). The skin has very high concentrations of Langerhans and Dendritic cells, which are potent immunological players (8,9). It is frequently observed that when vaccines are administered to the skin, more powerful responses are generated, or lower doses produce equivalent responses when compared to i.m. injections (4,10,11). The caveat to i.d. vaccination has historically been a difficulty precisely accessing the intradermal space, or delivering accurate doses (12).

Microneedles (MNs) are an attractive delivery device for vaccines, as they overcome many of the obstacles mentioned above. In brief, they are typically patches containing an array of small projections (<1500 μm) that penetrate into, but not through, the skin and deliver a therapeutic payload. They are specifically designed for intradermal delivery, and come in many varieties (12-14). MNs are small and self-contained, so can easily be stored and prepared. They generally do not cause bleeding and/or may dissolve entirely, creating little or no biohazardous waste. They can be self-applied, cause less pain, and are widely preferred by patients over hypodermic needles (15-17). When used to deliver vaccines, MNs generally show a significant advantage over i.m. injections, typically on par with or superseding i.d. injections (11,18,19). MNs have real potential to replace hypodermic needles in many usages, and improve worldwide vaccine coverage.

One area of research that has been lacking in the microneedle field is that of long-acting controlled release. As previously mentioned, most vaccines require booster doses. This is generally because modern vaccines induce a weak immune response, and the antigen must be re-introduced to bolster the response and/or maintain protective levels of immunity (20). Each booster dose requires a separate shot and thus a separate trip to a healthcare provider. However, it may be possible to develop a single formulation that acts both as the priming dose and subsequent booster doses, and can be administered as a single, one-time injection. Much work has been done in the field of single-administration vaccines (21,22). Furthermore, it has been shown that the kinetics of antigen presentation significantly affect the immune response, and that continuous antigen presentation may be more advantageous than the pulsatile method used with booster injections (23).

A common approach to controlled release is to encapsulate an antigen in microspheres of a controlled release polymer such as a poly(lactic-*co*-glycolic acid) (PLGA). These polymers are already used in several FDA-approved controlled release medicines. They are biodegradable, biocompatible, and easily tailored to work within a desired controlled release time-frame (24,25). They slowly degrade *in vivo* and as they do more antigen is released. While PLGAs are currently being investigated as delivery systems for single-administration vaccines (25,26), these systems often fall victim to poor antigen stability, as the process used to fabricate PLGA microparticles is known to damage sensitive antigens (27,28). However, a new system called Active Self-Encapsulation (ASE)

largely circumvents this issue by encapsulating antigen after microparticle fabrication (29-31).

Presented here is the combination of controlled antigen release from PLGA microparticles with intradermal delivery via microneedles. By using the ASE loading paradigm, a variety of antigens can be stability loaded into PLGA microparticles for long-acting controlled release. These microparticles are used to build a microneedle patch that serves as the delivery device for intradermal presentation to the immune system. The bulk of the patch is made of a water-soluble material that dissolves when applied to the body, thus eliminating biohazardous waste while still providing the mechanical strength needed for insertion. This material also stabilizes the antigen/microparticles during a freeze-drying step that creates a solid-state vaccine, and may lessen the need for refrigeration during transit. In whole, this proof-of-concept work shows that a microneedle patch based on Active Self-Encapsulating PLGA microparticles is a viable system of presenting vaccine antigens to the intradermal immune system without the use of hypodermic needles.

4.3 Materials and Methods

4.3.1 Materials

PLGA 50:50 (*i.v.* = 0.60 dL/g, *Mw* ≈ 55.4 kDa, ester terminated) was purchased from Lactel. PLA resin was from Nature Works LLC (Ingeo biopolymer 3251D). PDMS was made from Sylgard 184 silicone elastomer from Electron Microscopy Services. Poly(vinyl alcohol) (PVA) (80% hydrolyzed,

Mw = 9-10 kDa) and Ovalbumin (OVA) was purchased from Sigma Aldrich. Recombinant Hepatitis B surface antigen (rHBsAg) was from Arista Biologics. Alhydrogel 2% was from Invivogen. OVA-AlexaFluor 488 and OVA-AlexaFluor 647 were from Life Technologies. Porcine ear tissue was obtained from the Univeristy of Michigan Animal Surgery Operating Rooms (ASOR) Laboratories, and was stored at -20 ˚C until use. All chemical were analytical grade or better. The housing and handling of all experimental animals was in accordance with the terms of the University Committee on Use and Care of Animals (University of Michigan UCUCA) and all NIH guidelines for the care and use of laboratory animals.

4.3.2 Preparation of Active Self-Encapsulating PLGA Microparticles

w/o/w double-emulsion porous PLGA microparticles were prepared via solvent evaporation adapting on methods previously reported (29). 350 mg PLGA was dissolved in 1 mL dichloromethane. The inner-water phase was prepared by concentrating Alhydrogel to 6.35% via centrifugation and removal of excess solution, then 8% (*w/v*) trehalose was added and the slurry was mixed. 0.2 mL of the inner-water phase was added to 1 mL of the dissolved polymer phase, then homogenized for 1 minute at 17k rpm on a Tempest I.Q.^{2} Sentry Microprocessor. 2 mL of a 5% (*w/v*) PVA solution was then dumped into the PLGA and vortexed for 50 s. Lastly, the w/o/w emulsion was poured into 100 mL of a 0.5% (*w/v*) PVA solution and hardened under rapid stirring for 3 hours. The resulting microparticles were passed through a 60 µm and 10 µm

sieve in series and washed with ddH_2O to remove excess PVA. The microparticles were then centrifuged (200 g, 5 min) to remove excess liquid, frozen by submersion in LN_2, and lyophilized for 48 h.

4.3.3 Loading of Vaccine Antigens in ASE Microparticles

Active self-encapsulation of model and clinical vaccine antigens was modified from previously reported methods (29). Flocculated OVA was resuspended at a stock concentration of 1 mg/mL in 10 mM MOPS buffer, pH 7.4. rHBsAg was first buffer exchanged from PBS to MOPS using Microcon centrifugal filter devices with a 10K MWCO and following the provided guidelines, then brought to a 1 mg/mL stock in MOPS. 0.5 mL of 1 mg/mL antigen solution was added to 20 mg microparticles in a low protein-binding 0.5 mL microcentrifuge tube. The tube was protected from light and rotated for 2 d at 4 ˚C, 1 d at room temperature, and 2 d at 42 ˚C. After incubation the suspension was centrifuged for 5 min at 6010 rcf and the supernatant was removed and saved for analysis. The microparticle pellet was transferred to a 2 mL low protein-binding microcentrifuge tube and washed 3X with MOPS. Loading and encapsulation efficiencies (*EE%*) were determined using the following formulas using the lost mass of antigen from the loading solution compared against positive controls.

$$\%\ w/w \text{ loading: } \frac{mass\ of\ antigen\ encapsulated\ by\ microparticles}{mass\ of\ microparticles} \times 100$$

$$EE\%: \frac{mass\ of\ antigen\ encapsulated\ by\ microparticles}{initial\ mass\ of\ antigen\ in\ the\ loading\ solution} \times 100$$

4.3.4 Preparation of Microneedle Patches, Including Masters, Molds, and Pedestals

PLA MN masters were a generous gift from the lab of Dr. Mark Prausnitz at the Georgia Institute of Technology. The fabrication of these masters has been described elsewhere (32). Briefly, the patches consisted of a 10 X 10 array of pyramidal MNs (300 µm X 300 µm X 600 µm) with tip-to-tip spacing at 640 µm. From these masters, PDMS molds were cast and used to make subsequent MN patches of equivalent geometry.

To make standard MN patches (lacking a pedestal), antigen-loaded microparticles were first washed 3X with MOPS, then resuspended in cold ddH_2O at an approximate concentration of 40 mg/mL and kept on ice. 25 µL of the microparticle suspension was pipetted onto the surface of the PDMS mold, and the mold was pulled under vacuum for 10 mins at approximately 25 in.Hg. Excess suspension was then removed and returned to the stock for reuse. The mold was then centrifuged for 10 mins at 3220 rcf at 4 ˚C. Excess microparticles were removed from the surface of the mold via gentle tape-stripping. Approximately 90 µL of a 40% PVA + 30% sucrose (*w/v*) solution was then applied over the molds, and pulled under vacuum for 30 mins. The patches were then allowed to dry in a fume hood overnight before being demolded and trimmed of excess material around the edges to form a ~1 cm^2 square patch. The patches were then submerged in LN_2 and lyophilized for >48 h. Patches were stored under desiccation at 4 ˚C until use.

The pedestal masters were 3D printed with assistance from the University of Michigan 3D lab using a ProJet 3500 HD Max printer. The pedestal was modified from lithography methods previously described (33). It consisted of a 10 X 10 array that could be overlaid onto the MN mold (center-to-center spacing of 640 µm), made of pyramidal trapezoids with a 300 µm wide square base, 800 µm tall, and a 130 µm wide square top. After fabrication the mold was cleaned of printing oil, then a PDMS mold was cast from the structure. From this mold the part was recast using the same PVA/sucrose mixture used to make the microneedles, dried, trimmed, and demolded.

To create pedestal patches, the aforementioned patch process was carried out identically through the first centrifugation step. After tape-stripping away excess surface microparticles, 25 µL of the PVA/sucrose mixture was vacuumed onto the mold for 10 minutes while the mold was covered to prevent evaporation and premature hardening of the patch. Surface PVA/sucrose was then removed using a razor under a stereomicroscope (Nikon Olympus). A pedestal part was then aligned with the MN cavities and gently pressed in place. The patches were then allowed to dry in a fume hood overnight, demolded, and freeze-dried. Each patch used in this study was visualized on a stereomicroscope to ensure microneedle quality. Malformed patches were occasional, but discarded.

4.3.5 *In vitro* Release and Stability of Antigens from Microparticles and Microneedles

For microparticles, *in vitro* release was done by resuspending microparticles (20 mg, unless otherwise noted) in 1 mL PBST (PBS + 0.02% Tween 80), pH 7.4. For MN patches, four patches were placed in a 2.0 mL microcentrifuge tube and dissolved in ddH_2O over one hour and washed 3X. The resulting microparticle pellet was then resuspended in 0.25 mL PBST. Samples were shaken (240 rpm) at 37 ˚C and at each timepoint (1, 3, 7 days and weekly thereafter), the microparticles were centrifuged 5 mins at 6010 rcf and the full release media was removed for antigen analysis via size-exclusion chromatography (SEC) and replaced with fresh PBST.

To assess the stability/immunoreactivity of OVA released from MNs, the previously mentioned release media was further quantified using a commercial OVA-specific enzyme-linked immunosorbent assay (ELISA) kit (Alpha Diagnostics). The kit was used in accordance with the manufacturer's instructions. Samples were diluted with the provided sample diluent based on SEC data to fall within the range of standards. The plate was read at 405 nm using a Synergy Neo plate with Gen5 software, and analyzed in GraphPad Prism software using a 4-parameter logistic curve.

4.3.6 Size Exclusion Chromatography of Antigens

Unless otherwise stated, antigen concentration was determined by SEC using either high or ultra performance liquid chromatography (HPLC/UPLC). In

either case, the mobile phase consisted of PBS, pH 7.4 flowed at 1 mL/min (HPLC) or 0.4 mL/min (UPLC). Injection volumes were 50 or 10 µL for HPLC and UPLC, respectively. All samples were filtered through 0.45 µm filters prior to injection. A TSKgel G3000SWxl column was used for HPLC and an Acquity BEH SEC (4.6 X 150 mm) column was used for UPLC. UV detection was done at 215 nm. All samples were carried out in triplicate or greater.

4.3.7 Microneedle Penetration and Microparticle Deposition/Histology

For all studies evaluating mechanical integrity of microneedle patches, excised porcine ear tissue was used. The shaved inner skin with cartilage attached was separated from the outer skin and subcutaneous fat with a razor, and pinned taut on a cutting board. Standard and pedestal patches were gently placed tip-down onto the skin, and pressed in firmly with the thumb for 10 s. The patch was then removed and Gentian Violet (Ricca Chemical Co.) was applied to the application site for one minute before being wiped away with an alcohol pad. The application site was then cut away and imaged on a stereomicroscope (n=5 for each patch type).

To evaluate depth of MN penetration/microparticle deposition, microparticles loaded with OVA-AF488 were fabricated into MNs and the experiment was performed similar to above, except patches were held on the tissue for 5 minutes with pressure, then placed in a 37 ˚C chamber at 98% humidity for 15 additional minutes to allow the MNs to dissolve. The backing of the patches was gently removed and the application site tissue was cut out and

embedded in OCT compound, which was subsequently dipped in isopentane chilled by surrounding LN_2. The samples were then cut into 50 µm sections using a Leicia 3050S cryostat onto Superfrost+ microscope slides. Slides were thawed and immediately imaged on a fluorescent stereomicroscope.

4.3.8 Microparticle Mass Balance and Fraction of Dose Delivered

To determine the mass of microparticles in each patch, four patches were placed in a microcentrifuge tube and the PVA/sucrose material was dissolved with ddH_2O and washed 3X before drying in a vacuum oven at 40 ˚C overnight. The resulting sample was weighed and the mass divided to determine the mass per patch.

To determine the mass of microparticles delivered upon application of the MN patches, a live animal model was necessary. Using male nude BALB/c mice (Charles River), the application site was removed of any light hair using depilatory cream (Nair®) one day in advance of patch application. The mice were anesthetized via vaporized isoflurane, and placed on a heated pad to maintain body temperature. A fold of skin from the dorsal flank was pulled from the body and held taut on a cutting board. A microneedle patch was gently placed on the skin, and pressed in with the thumb for 5 mins. Pressure was then removed and the patch was kept on the skin for an additional 15 mins. The remaining portion of the patch was then removed and placed in a microcentrifuge tube. Again, four patches were used per sample (n=3 samples). The patches were then dissolved in ddH_2O and washed 3X, then dried in a

vacuum oven at 40 ˚C overnight. To account for residual animal tissue that was picked up by the patches, the mass of microparticles remaining in the patches after application was determined by Gel Permeation Chromatography (GPC). The pellet was resuspended in 0.5 mL tetrahydrofuran (THF) and rotated for 30 mins to dissolve the polymer. The samples were then spun for 5 mins at 6010 rcf to pellet the tissue and the supernatant was run on a Waters model 2414 IR detector with a Styragel HR 5E THF column in series with a Styragel HR 1 THF column both kept at 35 ˚C. The mobile phase of THF was pumped at 0.5 mL/min, and the full run time was 20 mins. Samples were run against standards made from known masses of microparticles dissolved in THF.

4.3.9 *In vivo* Microparticle Tracking

To evaluate the residence time and tissue distribution of microparticles and antigen administered via MN patches, microparticles were first loaded with OVA-AF647 and incorporated into pedestal MN patches. The patches were then applied to male albino C57BL/6J mice (Jackson Laboratories) as described above. Two patches were applied per mouse, to the left anterior and right posterior dorsal flank. At predetermined time-points, the whole animal was anesthetized and imaged using a PerkinElmer IVIS Spectrum imaging system. Fluorescence data was processed using a region-of-interest (ROI) analysis with background subtraction using Living Image 4.5 software. Other study groups included mice given an i.d. injection to the same locations of an equivalent delivered dose of OVA-488-loaded microparticles or soluble OVA-AF647. Also

included were smaller (mean diameter = 7.1 μm) calcium phosphate-based microparticles (supplementary information) and pedestal patches made from said microparticles. Mice were kept on an alfalfa-free diet to reduce autofluorescence. Depilatory cream was not reapplied during the study, but hair was kept trimmed using electric razors (n=4 mice/group, 2 applications per mouse).

4.3.10 Skin Resealing

Evaluation of skin resealing kinetics was determined in tandem with the *in vivo* microparticle tracking study mentioned above. Transepithelial water loss (TEWL) was measured using a Delfin Technologies VapoMeter with DelfWin 4 capture software. Study groups consisted of application of *A*) ASE microparticle-loaded pedestal patches, *B*) pedestal patches loaded with calcium phosphate-based microparticles, *C*) vehicle-only patches (pedestal MN patches made of only PVA/sucrose, no microparticles), and *D*) PLA master patches (no pedestal) that did not dissolve or considerably break when applied to animals. Three measurements were taken per application site, per animal, at each timepoint, and the TEWL chamber was allowed to re-equilibrate to environmental conditions before each measurement. To measure TEWL, the VapoMeter was gently pressed against the application site without any manual tension applied to the skin. Data is presented as percent increase over an application control using ANOVA with Fisher's LSD. The application control

consisted of a flat PVA/sucrose mock patch that did not contain any microneedles, but was applied similar to other groups.

4.3.11 Immunization Study

Male C57Bl/6 (for OVA groups) or BALB/c (for rHBsAg groups) mice, 5-6 weeks old, 5 mice/group, were purchased from Jackson Laboratories. One day prior to priming and booster immunization the application site for MN patches or i.d. administered groups was shaved and depilatory cream was applied, or just shaved for i.m. administered groups. On day zero mice were immunized with either *A*) two pedestal microneedle patches, or equivalent delivered antigen dose from, *B*) i.d. microparticles, *C*) i.m. microparticles, *D*) Alhydrogel-adsorbed antigen, or *E*) soluble antigen. A sham group received patches containing microparticles that did not contain antigen. To evaluate the controlled release potential of the system, additional groups received a double dose on day zero of pedestal MN patches, i.m. microparticles, or Alhydrogel-adsorbed antigen. These groups did not receive a booster. Booster doses for other groups were given 21 days after the priming dose.

To evaluate antibody titers, blood was drawn on days 20 and 42 via submandibular bleed. Serum was separated using Microvette 500 Zgel serum collection tubes centrifuged for 5 mins at 10,000 rcf. Serum was stored at -80 ˚C until analysis. Serum samples were analyzed by the University of Michigan Cancer Center Immunology Core for IgG, IgG1, IgG2c, and IgA via ELISA. Antigen-specific IgG1 isotype was used as a standard for all IgGs to

determine relative concentration. Data was compared using one-way ANOVA with Tukey's post-test via GraphPad Prism® software.

To evaluate the nature of the cytokine response produced after restimulation of splenic lymphocytes, all mice were euthanized on day 42 and spleens were collected under sterile conditions. Splenocytes were collected by grinding each spleen through a 70 µm nylon strainer. Red blood cells were lysed with ACK lysing buffer and the cells were washed 3X with sterile PBS before being resuspended in RPMI 1640 media supplemented with glutamine, 10% FBS (10%), 1 U/mL penicillin + 1 µg/mL streptomycin, 55 µM 2-mercaptoethanol, MEM non-essential amino acids (1%), 1 mM Sodium Pyruvate, and 10 mM HEPES. Cells were then plated at 5 x 10^5 cells/well in a 96-well plate and stimulated with media (negative control) or 25 µg/mL whole antigen (OVA or rHBsAg). Positive controls were pooled from each spleen within a group and stimulated with 2 µL/mL PMA/ionomycin (cell stimulation cocktail). Cells were incubated for 96 hours at 37 ˚C with 5% CO_2 before collecting the supernatant and storing at -80 ˚C. Concentrations of IL2, IL6, IL10, and TNFα were analyzed via ELISA through the University of Michigan Cancer Center Immunology Core. Stimulated cell supernatants were compared against negative controls using Student's t-test.

4.4 Results and Discussion

4.4.1 Microparticle Fabrication, Loading, and Release

A detailed evaluation of the microparticles used in these studies is provided in Chapter 3 of this dissertation.

4.4.2 Fabrication and Evaluation of Microneedle Patches Containing Microparticles

The process utilized here proved to be a reliable and consistent method for fabricating MN patches containing PLGA microparticles in the microneedles. This represents the first known occurrence of PLGA microparticles in this size range (10–60 µm) being successfully encapsulated into microneedles, and is the first work to utilize PLGA microparticles loaded via the Active Self-Encapsulation system in this manner. When making standard patches, microparticles could be readily observed in the microneedles, with only a minute amount of particles in the backing (Fig 4-1 A&B). The process was effective at minimizing microparticle waste, as excess microparticles used in the first suspension cast could be recovered. Only after centrifugation and tape stripping were microparticles lost. In future work, it may be possible to more accurately manipulate the molds to minimize loss, such as through direct micropipetting into individual microneedle cavities. It is important to minimize or prevent microparticles from sitting in the backing, as any fraction of the dose localized to that space is unlikely to be delivered upon application.

Furthermore, this approach was easily adapted to include a pedestal design that increased the functional length of the MNs while keeping the

microparticles localized to the microneedle portion (Fig 4-1 C&D). While pedestal-style patches are becoming more frequent in microneedle literature as their necessity becomes apartment (further described below), previous designs utilized either a non-biocompatible support structure (which must be removed and may be considered biohazardous waste), or included drug in the pedestal portion that was not delivered (32,33,35). Here, however, the full patch is made of a dissolvable material, allowing the patch to be applied and left on the skin until it fully dissolves. By excluding microparticles from the pedestal, the fabrication process became more complex, but reduced antigen waste and may improve downstream variability.

Additionally, utilizing 3D printing proved to be a cost-effective method for fabricating the pedestal master. Alternative pedestals from the literature have relied on photolithography, which can run 10–100X the cost of 3D printing. Since these parts did not require a sharp tip or smooth edges, as they were not intended to directly penetrate tissue, the limited resolution of current 3D printing was not a factor. Once the part was fabricated, a mold was made and it was recast using the dissolving PVA/sucrose mixture used in the microneedles (Supp. Fig 4-1). Creating a pedestal MN patch involved additional manual manipulation, as excess PVA/sucrose had to be removed with a razor, and the pedestal part was manually aligned with the MN cavities and pressed in place. While this occasionally resulted in malformed patches, advances in automation could greatly improve this process. While the standard microneedles had a height of 600 µm, and the pedestal part was 800 µm tall, the final tip-to-base

height of the pedestal patches was 1183 ± 6 μm, suggesting roughly 200 μm of overlap between the pedestal and the microneedle, which is confirmed by confocal imaging (Fig 4-1D).

To determine the mass of microparticles that could be packed into a patch, the patches were dissolved, washed, and massed. The standard patches contained 244 μg of microparticles, while the pedestal patches contained 208 μg (Table 4-1). The difference in mass likely results from the additional manipulation required of the pedestal patches; possibly from pulling some microparticles out of the mold, or doing a more complete job of removing microparticles from the backing. Focusing on a model antigen, OVA, which loads into the microparticles at 1.64% (*w/w*), this corresponded to a final antigen dose of 4.0 and 3.4 μg/patch for standard and pedestal patches, respectively. Because different antigens load at different levels into the microparticles, this dose will mildly increase or decrease with different antigens. To adjust dosage, several options present, such as changing the number of microneedles in the array, using multiple patches, or diluting the microparticles. It does not seem likely that more microparticles in this size range could be packed easily into a MN without changing the overall geometry.

4.4.3 *In vitro* Release and Stability

In vitro, the MN patches demonstrated controlled release of soluble antigen (OVA) over approximately one month (Fig 4-2). To evaluate this, microparticles were loaded with antigen, either OVA (Fig 4-2) or rHBsAg (Supp. Fig 4-2) and

loaded into microneedle patches. The patches were dissolved in and washed 5X with ddH_2O to remove PVA/sucrose binding material prior to starting the release study in PBST. While this was a necessary step to ensure accurate analysis, it represents a considerable discrepancy between these *in vitro* results and possible *in vivo* predictions. *In vivo* the dissolution of the PVA/sucrose binding material is expected to take considerably longer than *in vitro*, as interstitial fluid must be recruited to the application site, dissolve the material, and then be cleared to allow complete dissolution and subsequent liberation of the microparticles. In addition, since the patch has been lyophilized, the microparticles must be hydrated as well in order for release to begin (36). In brief, the burst release observed on day one is expected to be delayed *in vivo*.

The microparticles and MN patches demonstrate similar release kinetics, but with the microneedles' release curve shifted downward 10-15% in total cumulative release. This could be due to a variety of factors including, *A*) unrecorded antigen release while dissolving the PVA/sucrose binding material, *B*) a change in release mechanism or damage to the antigen caused by the microneedle fabrication process – likely the application of the PVA/sucrose material or the lyophilization process (37), *C*) difficulties accurately determining the amount of antigen in the microneedle patches, or *D*) an increase in binding avidity between the antigen and Alhydrogel adjuvant brought on by post-adsorption lyophilization. For example, when OVA-loaded microparticles were freeze-dried without cryoprotection and then evaluated for *in vitro* release, similar release kinetics were observed but with a significant

downward shift (Supp. Fig 4-3), possibly suggesting that more antigen is now ligand-bound to Alhydrogel (38). In any case, the remaining antigen that was not released as a soluble fraction was likely released as a particulate complex ligand-bound to Alhydrogel. A detailed explanation and evidence of this process is outlined in Chapter 3 of this dissertation.

To evaluate the immunoreactivity/stability of antigen after patch fabrication and during *in vitro* release, antigen concentration as determined by SEC was compared to that determined via ELISA (Fig 4-3). The measurements were found to be in good agreement (generally near 100% immunoreactivity), suggesting that the antigen was not damaged during the patch fabrication process. There is a modest decrease in immunoreactivity at some later time points, possibly due to the increased length of the sampling interval, and/or that the soluble antigen may become less stable over time.

4.4.4 Microneedle Penetration and Microparticle Deposition

To assess the ability of the microneedles to penetrate skin, patches were manually applied to excised porcine tissue and the resulting microchannels were stained with Gentian Violet. Both standard and pedestal patches were evaluated (Fig 4-4A,B), n=5. For standard patches, all five patches tested produced 100 clearly identifiable microchannels, suggesting the patches possess the mechanical integrity necessary to penetrate skin tissue. Pedestal patches produced an average of 98 (±2) microchannels. This is likely due to a combination of factors such as: *A*) poor alignment of the pedestal with the

microneedles, *B*) imperfect microneedle tips due to excess force used during patch fabrication, *C*) decreased structural integrity due to the addition of the pedestal, or *D*) non-uniform pressure during application, which is exacerbated by the longer microneedles.

To verify that after the MNs penetrate the skin they dissolve intradermally to deliver microparticles, patches were fabricated with microparticles loaded with OVA-AF488. These were applied same as above, but the patch was allowed to remain in the tissue for 20 minutes to dissolve. After removing the patch, the tissue could be fluorescently imaged to visualize the microparticles (Fig 4-4C). The fluorescence is localized to the grid pattern, strongly suggesting that the microneedles dissolve intradermally and release the microparticle payload, and the microparticles do not spread out either on the surface of the skin or within the tissue.

Afterwards, the tissue was frozen and cryosectioned to visualize cross-sections of the skin at the application site. Fig 4-4D shows a representative cross-section of the tissue, and confirms that microparticles had been intradermally deposited via the MN patches. Together, Fig 4-4C and 4-4D suggest that microparticles are not left on the surface of the skin where they would be inactive, but rather are deposited below the stratum corneum, mostly in the dermis.

After removing the patches in the aforementioned studies, it was apparent some microparticles remained on the patch and had not been deposited. To

quantify this, a live animal model was necessary to account for the temperature and recruitment of interstitial fluid necessary to dissolve the patches. Standard and pedestal patches were applied to hairless mice as described above. Images of the patches after application are shown in Supp. Fig 4-4. To account for hair and tissue that was picked up by the patches, a GPC method was developed to determine the ratio of PLGA mass in an applied patch versus a neat patch. As shown in Table 4-1, an applied standard patch still contained 75% of the original PLGA, while a pedestal patch only contained 45%. The inability of microneedle patches to deliver 100% of the dose located in the microneedles is well established in the literature (32,39,40). This is typically attributed to the elasticity of the skin preventing the entirety of the microneedles from entering the dermis for delivery, and is the motivation for pedestal designs as described here and elsewhere (32,33,35). While the pedestal improved delivery, and thus was used for further animal testing, delivery was still not complete. This is likely due to the tip of the microneedles breaking off or dissolving immediately upon penetrating the stratum corneum and preventing the microneedle from inserting as deeply as would otherwise be possible. Cross-sectional images of microparticles imbedded by standard or pedestal patches also showed that the pedestal patches only had a modest improvement in maximum microparticle deposition depth (data not shown). Thus, future work could investigate using either a stronger and/or slower-dissolving material in place of the PVA/sucrose, or possibly coating the tip of the microneedles with a material to enhance their strength.

4.4.5 Skin Resealing via TEWL

A potential concern for advancing MN technologies is the wounds caused to the skin by application of the patch. If these wounds do not close quickly the potential for infection exists. Several studies have investigated the ability of skin to reseal after application of MN patches, including the ability of microorganisms to traverse these microchannels (41-44). Those results suggest that the microchannels can close rapidly, ranging from under an hour up to two days, depending on the style of MN patch and the skin model used. However, at least one study suggests that when the resulting microchannels are occluded, the resealing time is greatly increased (44). Furthermore, existing literature focuses on the use of solid, non-dissolving type patches, which do not deposit any material in the wound. Thus, it was necessary to explore the skin resealing kinetics after application of the patches used here in order to evaluate if the microparticles, or the PVA/sucrose binding material, affected the skin's ability to close the microchannels.

All patches were applied identically to shaved mice, and TEWL data was recorded at predetermined intervals. Immediately after application, TEWL values for all test groups rose significantly (Fig 4-5). The PLA master group generated a much higher response than the other groups. This could be because these patches were made of a stronger, non-dissolving material, that did not significantly deform when applied and thus likely generated larger wounds through which more moisture could escape (giving higher TEWL

readings). However, it is also plausible that because the other patches deposited material in the skin, moisture that would have otherwise escaped was instead blocked and used for MN dissolution, yielding a TEWL value that was irrepresentably low of actual wound size.

Within six hours of application, wounds from the PLA master patches had already resealed. This is consistent with previous literature suggesting wounds made from solid non-dissolving MNs reseal quickly (41,42). Wounds from vehicle patches and from patches containing smaller microparticles resealed by the end of the first day. Wounds from the standard microparticle patches resealed between the second and third day. This data may suggest that material deposited in the skin by dissolving MNs acts as an occlusion and hinders skin resealing. Furthermore, insoluble microparticles that were deposited in the skin, and did not dissolve, further hindered the skin-resealing process, with larger particles further slowing the process compared to an equivalent volume of smaller particles.

4.4.6 *In vivo* Tracking of Fluorescently-loaded Microparticles

While penetration and microparticle deposition studies are useful to determine how well the microneedle patches deposit their payload when applied, it is also important to determine the behavior of the microparticles and antigen in the skin over time. While it is generally understood that soluble material will be absorbed into the circulation and/or lymphatics, the behavior of larger biodegradable depots is less well characterized. To evaluate this,

microparticles were again loaded with OVA-AF647 and fabricated into pedestal MN patches. Included again were the smaller calcium phosphate-based microparticles, treated similarly. All patches were applied to mice and the mice were imaged over time to evaluate the strength and localization of the fluorescent signal. Values were compared against i.d. injected microparticles (both types) and soluble OVA.

After administration the application site was highly visible through fluorescent imaging, with individual MN channels identifiable (Fig 4-6A). Over the next 3-10 days, the application site retained its fluorescence for all patches and injected microparticles. After only one day, however, the soluble antigen signal was heavily attenuated and was lost entirely by day 3. This suggests that microparticles deposited by the MNs are not quickly pushed out of the skin either by the rapid turnover of the epidermal layer (45), nor by the general movement of the animals. While the signal did decrease faster than was anticipated, this was true for the i.d. injected microparticles as well (Fig 4-6 B&C). This could be due to *A*) attenuation of the fluorescent signal, either by a cleaving off/degradation of the fluorescent tag, or by photobleaching, *B*) more rapid and complete antigen release *in vivo*, *C*) the animals manually removing some microparticles while licking/cleaning the site, or *D*) a gradual migration of the depot away from the injection site. However, additional studies are needed to further probe this phenomenon.

4.4.7 Immunizations

To determine if these MN patches or stand-alone microparticles stimulate an immune response, mice were dosed with MN patches or microparticles alone containing OVA or rHBsAg. 20 days after OVA priming doses, i.m. and i.d. microparticles were the only groups to generate significant anti-OVA IgG levels compared to sham control groups (Fig 4-7A). This is consistent with the hypothesis mentioned in Section 4.4.3 that MN patches would release slower *in vivo* than is predicted by the *in vitro* release tests, but that this disconnect would not correlate as strongly to stand-alone microparticles. 21 days after booster doses however, all microparticle/microneedle groups showed high IgG levels compared to sham and soluble OVA, and were as good as or better than conventional Alhydrogel-adsorbed antigen. Trends were similar for IgG1 (which results from a Th2-mediated response (46)), while IgG2c (which results from a Th1-mediated response (46)) was very low for all groups, with only the microparticle groups producing slightly significant levels by the end of the study. rHBsAg-immunized mice showed similar results at the end of the study, with MN-dosed mice showing high levels of total IgG and IgG1 compared to sham, and at levels that were again as good as or better than Alhydrogel-adsorbed antigen (Fig 4-7B). At day 20, however, MN-dosed mice showed no response, whereas Alhydrogel-adsorbed rHBsAg was already producing high levels of both total IgG and IgG1. This is could be due to the same *in vivo* delay explained for OVA, coupled with the fact that rHBsAg was shown to release even slower than OVA (Supp. Fig 4-2). In brief summary, these results suggest

MNs and microparticles generate a robust Th2-skewed response, which is as good as or better than conventional vaccine approaches.

When a booster dose was omitted, and the full antigen dose was given on day zero, mice immunized with microparticles produced an equivalent response to those that received the booster (Fig 4-8). Otherwise, following a prime-boost approach generally produced stronger responses than prime alone. However, this suggests these formulations warrant further evaluations as a single-administration vaccine.

When harvested splenocytes were restimulated with antigen, the only cytokine detected in sufficient quantities was IL-10 (Fig 4-9), which is secreted by Th2 cells (46). The immune response resulting from a Th2-type pathway is typically associated with a more humoral response, and only a weak or undetectable cell-mediated response. This is in agreement with the aforementioned IgG data, as well as the failure to detect high levels of antigen-specific $CD8^+$ cells in the blood of immunized mice (Supp. Fig 4-5).

As a whole, this proof-of-concept immunization study shows that hypodermic needle-free vaccination via ASE microparticle-containing microneedle patches is a viable option for further exploration, and that the ASE microparticles used in the MNs may be a useful method for controlled antigen release. The MN patches produced responses that were generally equivalent to i.d. injection of the microparticles, but did not rely on a hypodermic needle for injection. This seemingly minor detail actually has enormous consequences for

improving vaccine coverage for reasons mentioned above, including higher patient acceptability, self-application, and easier storage/disposal. It is unexpected that i.m. injection of microparticles produced equivalent or even stronger responses than i.d./microneedle administration, as this trend is typically reversed in the existing literature (11,47).

The controlled release potential of these polymer-based delivery systems is also apparent in the IgG data. For example, rHBsAg was shown to release more slowly from the microneedles than OVA (Fig 4-2 and Supp. Fig 4-2). Before the boost, it appears that Alhydrogel-adsorbed rHBsAg is producing a more robust IgG response, whereas after boost the responses are nearly equivalent. This may suggest that the slower release of this antigen delayed the development of the immune response. This is also true of the comparison between the microneedle patches and i.d. microparticles, as the patches were shown to release antigen more slowly than free microparticles (Fig 4-2). Future work would benefit from longer-term studies using a more robust skin model (*e.g.*, guinea pigs) to evaluate how the response stabilizes 60 or even 90 days after priming, and whether or not the responses continue to increase, as may be expected based on previous reports (23).

4.5 Conclusions

The MN patches explored here are shown to be a promising system for controlled release of vaccine antigens without reliance on hypodermic needles for administration. By basing the platform on Active Self-Encapsulating

controlled release PLGA microparticles, it gives the microneedle patches versatility to encapsulate not only various antigens, but also different styles of microparticles, as was shown here. These patches, with the addition of a pedestal, deliver their payload intraderamally with a simple application process that could easily be done by a patient or other non-healthcare professional. *In vitro* and *in vivo*, the patches show evidence of long acting controlled release of antigen (>1 mo). Importantly, they generate immune responses that are similar to or better than standard injected vaccines, but without the use of a hypodermic needle, and with long-acting results. While additional modifications to the system could further improve its utility, this work lays a foundation for a self-administered single-administration vaccine system that is applicable to a variety of vaccines and thus disease states.

4.6 References

1. WHO. Immunization Coverage 2016 [cited 2016]. Available from: http://www.who.int/mediacentre/factsheets/fs378/en/.
2. Williams W, Lu P, O'Halloran A. Surveillance of Vaccination Coverage Among Adult Populations - United States, 2014. Surveillance Summaries. 2016;65(1):1-36.
3. USDHHS. The Great Pandemic: The United States in 1918-1919 2016. Available from: http://www.flu.gov/pandemic/history/1918/
4. Glenn GM, Kenney RT. Mass vaccination: Solutions in the skin. Curr Top Microbiol. 2006;304:247-68. PubMed PMID: ISI:000242419300014.
5. Taddio A, Ipp M, Thivakaran S, Jamal A, Parikh C, Smart S, et al. Survey of the prevalence of immunization non-compliance due to needle fears in children and adults. Vaccine. 2012;30(32):4807-12. Epub 2012/05/24. doi: 10.1016/j.vaccine.2012.05.011. PubMed PMID: 22617633.
6. Johnson DR, Nichol KL, Lipczynski K. Barriers to adult immunization. The American journal of medicine. 2008;121(7 Suppl 2):S28-35. Epub 2008/07/01. doi: 10.1016/j.amjmed.2008.05.005. PubMed PMID: 18589065.
7. Uscher-Pines L, Maurer J, Kellerman A, Harris KM. Healthy young and middle age adults: what will it take to vaccinate them for influenza? Vaccine. 2010;28(46):7420-2. Epub 2010/09/15. doi: 10.1016/j.vaccine.2010.08.095. PubMed PMID: 20837079.
8. Bos J, Luiten R. Skin Immune System. In: Stockfleth E, Ulrich C, editors. Skin Cancer after Organ Transplantation: Springer US; 2009. p. 45-62.
9. Bos JD, Zonneveld I, Das PK, Krieg SR, van der Loos CM, Kapsenberg ML. The skin immune system (SIS): distribution and immunophenotype of lymphocyte subpopulations in normal human skin. The Journal of investigative dermatology. 1987;88(5):569-73. Epub 1987/05/01. PubMed PMID: 3494791.
10. Belshe RB, Newman FK, Wilkins K, Graham IL, Babusis E, Ewell M, et al. Comparative immunogenicity of trivalent influenza vaccine administered by intradermal or intramuscular route in healthy adults. Vaccine. 2007;25(37-38):6755-63. Epub 2007/08/19. doi: 10.1016/j.vaccine.2007.06.066. PubMed PMID: 17692438; PubMed Central PMCID: PMC2148502.
11. Quan FS, Kim YC, Vunnava A, Yoo DG, Song JM, Prausnitz MR, et al. Intradermal vaccination with influenza virus-like particles by using microneedles induces protection superior to that with intramuscular immunization. Journal of virology. 2010;84(15):7760-9. Epub 2010/05/21. doi: 10.1128/JVI.01849-09. PubMed PMID: 20484519; PubMed Central PMCID: PMC2897640.
12. Kim YC, Jarrahian C, Zehrung D, Mitragotri S, Prausnitz MR. Delivery systems for intradermal vaccination. Current topics in microbiology and immunology. 2012;351:77-112. Epub 2011/04/08. doi: 10.1007/82_2011_123. PubMed PMID: 21472533; PubMed Central PMCID: PMC3173582.
13. Kim YC, Park JH, Prausnitz MR. Microneedles for drug and vaccine delivery. Advanced drug delivery reviews. 2012;64(14):1547-68. Epub 2012/05/12. doi: 10.1016/j.addr.2012.04.005. PubMed PMID: 22575858; PubMed Central PMCID: PMC3419303.
14. Park JH, Allen MG, Prausnitz MR. Polymer microneedles for controlled-release drug delivery. Pharmaceutical research. 2006;23(5):1008-19. Epub 2006/05/23. doi: 10.1007/s11095-006-0028-9. PubMed PMID: 16715391.
15. Norman JJ, Arya JM, McClain MA, Frew PM, Meltzer MI, Prausnitz MR. Microneedle patches: Usability and acceptability for self-vaccination against influenza. Vaccine. 2014. Epub 2014/02/18. doi: 10.1016/j.vaccine.2014.01.076. PubMed PMID: 24530146.
16. Gill HS, Denson DD, Burris BA, Prausnitz MR. Effect of microneedle design on pain in human volunteers. The Clinical journal of pain. 2008;24(7):585-94. Epub 2008/08/22. doi: 10.1097/AJP.0b013e31816778f9. PubMed PMID: 18716497; PubMed Central PMCID: PMC2917250.
17. Gupta J, Park SS, Bondy B, Felner EI, Prausnitz MR. Infusion pressure and pain during microneedle injection into skin of human subjects. Biomaterials. 2011;32(28):6823-31. Epub 2011/06/21. doi: 10.1016/j.biomaterials.2011.05.061. PubMed PMID: 21684001; PubMed Central PMCID: PMC3143217.
18. Matriano JA, Cormier M, Johnson J, Young WA, Buttery M, Nyam K, et al. Macroflux microprojection array patch technology: a new and efficient approach for intracutaneous immunization. Pharmaceutical research. 2002;19(1):63-70. Epub 2002/02/12. PubMed PMID: 11837701.

19. DeMuth PC, Li AV, Abbink P, Liu J, Li H, Stanley KA, et al. Vaccine delivery with microneedle skin patches in nonhuman primates. Nature biotechnology. 2013;31(12):1082-5. Epub 2013/12/10. doi: 10.1038/nbt.2759. PubMed PMID: 24316643; PubMed Central PMCID: PMC4011140.
20. Murphy K, Travers P, Walport M, Janeway C. Janeway's immunobiology. 8th ed. New York: Garland Science; 2012. xix, 868 p. p.
21. Preis I, Langer RS. A single-step immunization by sustained antigen release. Journal of immunological methods. 1979;28(1-2):193-7. Epub 1979/01/01. PubMed PMID: 469267.
22. Vogelhuber W, Rotunno P, Magni E, Gazzaniga A, Spruss T, Bernhardt G, et al. Programmable biodegradable implants. Journal of controlled release : official journal of the Controlled Release Society. 2001;73(1):75-88. Epub 2001/05/05. PubMed PMID: 11337061.
23. Johansen P, Storni T, Rettig L, Qiu Z, Der-Sarkissian A, Smith KA, et al. Antigen kinetics determines immune reactivity. Proceedings of the National Academy of Sciences of the United States of America. 2008;105(13):5189-94. Epub 2008/03/26. doi: 10.1073/pnas.0706296105. PubMed PMID: 18362362; PubMed Central PMCID: PMC2278203.
24. Wischke C, Schwendeman SP. Degradable Polymeric Carriers for Parenteral Controlled Drug Delivery. Adv Del Sci Technol. 2012:171-228. doi: Doi 10.1007/978-1-4614-0881-9_8. PubMed PMID: ISI:000302879700008.
25. Schwendeman SPC, H.R., Gupta RK, Langer R. Peptide, Protein, and Vaccine Delivery from Implantable Polymeric Systems Progress and Challenges. In: Society TAC, editor. Controlled Drug Delivery1997. p. 229-67.
26. Manish M, Rahi A, Kaur M, Bhatnagar R, Singh S. A single-dose PLGA encapsulated protective antigen domain 4 nanoformulation protects mice against Bacillus anthracis spore challenge. PloS one. 2013;8(4):e61885. Epub 2013/05/03. doi: 10.1371/journal.pone.0061885. PubMed PMID: 23637922; PubMed Central PMCID: PMC3639271.
27. Jiang W, Schwendeman SP. Stabilization of tetanus toxoid encapsulated in PLGA microspheres. Molecular pharmaceutics. 2008;5(5):808-17. Epub 2008/08/20. doi: 10.1021/mp800027f. PubMed PMID: 18710256.
28. Zhu G, Mallery SR, Schwendeman SP. Stabilization of proteins encapsulated in injectable poly (lactide- co-glycolide). Nature biotechnology. 2000;18(1):52-7. Epub 2000/01/14. doi: 10.1038/71916. PubMed PMID: 10625391.
29. Desai KG, Schwendeman SP. Active self-healing encapsulation of vaccine antigens in PLGA microspheres. Journal of controlled release : official journal of the Controlled Release Society. 2013;165(1):62-74. Epub 2012/10/30. doi: 10.1016/j.jconrel.2012.10.012. PubMed PMID: 23103983.
30. Reinhold SE, Desai KG, Zhang L, Olsen KF, Schwendeman SP. Self-healing microencapsulation of biomacromolecules without organic solvents. Angew Chem Int Ed Engl. 2012;51(43):10800-3. Epub 2012/09/27. doi: 10.1002/anie.201206387. PubMed PMID: 23011773.
31. Reinhold SE, Schwendeman SP. Effect of Polymer Porosity on Aqueous Self-Healing Encapsulation of Proteins in PLGA Microspheres. Macromolecular bioscience. 2013;13(12):1700-10. Epub 2013/11/29. doi: 10.1002/mabi.201300323. PubMed PMID: 24285573.
32. Chu LY, Choi SO, Prausnitz MR. Fabrication of dissolving polymer microneedles for controlled drug encapsulation and delivery: Bubble and pedestal microneedle designs. Journal of pharmaceutical sciences. 2010;99(10):4228-38. Epub 2010/08/26. doi: 10.1002/jps.22140. PubMed PMID: 20737630.
33. Chen MC, Huang SF, Lai KY, Ling MH. Fully embeddable chitosan microneedles as a sustained release depot for intradermal vaccination. Biomaterials. 2013;34(12):3077-86. Epub 2013/02/02. doi: 10.1016/j.biomaterials.2012.12.041. PubMed PMID: 23369214.
34. Fan Y, Sahdev P, Ochyl LJ, J JA, Moon JJ. Cationic liposome-hyaluronic acid hybrid nanoparticles for intranasal vaccination with subunit antigens. Journal of controlled release : official journal of the Controlled Release Society. 2015;208:121-9. Epub 2015/04/15. doi: 10.1016/j.jconrel.2015.04.010. PubMed PMID: 25869965; PubMed Central PMCID: PMC4430437.
35. Chu LY, Prausnitz MR. Separable arrowhead microneedles. Journal of controlled release : official journal of the Controlled Release Society. 2011;149(3):242-9. Epub 2010/11/05. doi: 10.1016/j.jconrel.2010.10.033. PubMed PMID: 21047538; PubMed Central PMCID: PMC3040254.
36. D'Souza SS, Dorati R, DeLuca HF. Effect of Hydration on Physicochemical Properties of End-Capped PLGA. Advanced Biomaterials. 2014;2014:1-9.

37. Solanki VA, Jain NK, Roy I. Stabilization of tetanus toxoid formulation containing aluminium hydroxide adjuvant against freeze-thawing. International journal of pharmaceutics. 2011;414(1-2):140-7. doi: DOI 10.1016/j.ijpharm.2011.05.022. PubMed PMID: ISI:000292795500018.
38. Hansen B, Belfast M, Soung G, Song L, Egan PM, Capen R, et al. Effect of the strength of adsorption of hepatitis B surface antigen to aluminum hydroxide adjuvant on the immune response. Vaccine. 2009;27(6):888-92. Epub 2008/12/17. doi: 10.1016/j.vaccine.2008.11.078. PubMed PMID: 19071182.
39. Naito S, Ito Y, Kiyohara T, Kataoka M, Ochiai M, Takada K. Antigen-loaded dissolving microneedle array as a novel tool for percutaneous vaccination. Vaccine. 2012;30(6):1191-7. doi: DOI 10.1016/j.vaccine.2011.11.111. PubMed PMID: ISI:000300963400029.
40. Donnelly RF, Raj Singh TR, Woolfson AD. Microneedle-based drug delivery systems: microfabrication, drug delivery, and safety. Drug delivery. 2010;17(4):187-207. Epub 2010/03/20. doi: 10.3109/10717541003667798. PubMed PMID: 20297904; PubMed Central PMCID: PMC2906704.
41. Kalluri H, Kolli CS, Banga AK. Characterization of microchannels created by metal microneedles: formation and closure. The AAPS journal. 2011;13(3):473-81. Epub 2011/07/07. doi: 10.1208/s12248-011-9288-3. PubMed PMID: 21732220; PubMed Central PMCID: PMC3160154.
42. Kalluri H, Banga AK. Formation and closure of microchannels in skin following microporation. Pharmaceutical research. 2011;28(1):82-94. Epub 2010/04/01. doi: 10.1007/s11095-010-0122-x. PubMed PMID: 20354766.
43. Donnelly RF, Singh TR, Tunney MM, Morrow DI, McCarron PA, O'Mahony C, et al. Microneedle arrays allow lower microbial penetration than hypodermic needles in vitro. Pharmaceutical research. 2009;26(11):2513-22. Epub 2009/09/17. doi: 10.1007/s11095-009-9967-2. PubMed PMID: 19756972; PubMed Central PMCID: PMC2900181.
44. Gupta J, Gill HS, Andrews SN, Prausnitz MR. Kinetics of skin resealing after insertion of microneedles in human subjects. Journal of controlled release : official journal of the Controlled Release Society. 2011;154(2):148-55. Epub 2011/06/07. doi: 10.1016/j.jconrel.2011.05.021. PubMed PMID: 21640148; PubMed Central PMCID: PMC3164267.
45. Clausen OP, Schjolberg AR. Turnover and Maturation Kinetics in Regenerating Mouse Epidermis. Apmis. 1988;96:111-9. PubMed PMID: ISI:A1988Q741700006.
46. Storni T, Kundig TM, Senti G, Johansen P. Immunity in response to particulate antigen-delivery systems. Advanced drug delivery reviews. 2005;57(3):333-55. Epub 2004/11/25. doi: 10.1016/j.addr.2004.09.008. PubMed PMID: 15560945.
47. Demuth PC, Garcia-Beltran WF, Ai-Ling ML, Hammond PT, Irvine DJ. Composite dissolving microneedles for coordinated control of antigen and adjuvant delivery kinetics in transcutaneous vaccination. Advanced functional materials. 2013;23(2):161-72. Epub 2013/03/19. doi: 10.1002/adfm.201201512. PubMed PMID: 23503923; PubMed Central PMCID: PMC3595545.
48. Bailey B. Development and Characterization of Novel Self-Encapsulating Poly(lactic-co-glycolic acid) Microspheres for Vaccine Delivery. University of Michigan, PhD Thesis, Department of Pharmaceutical Sciences. 2016.

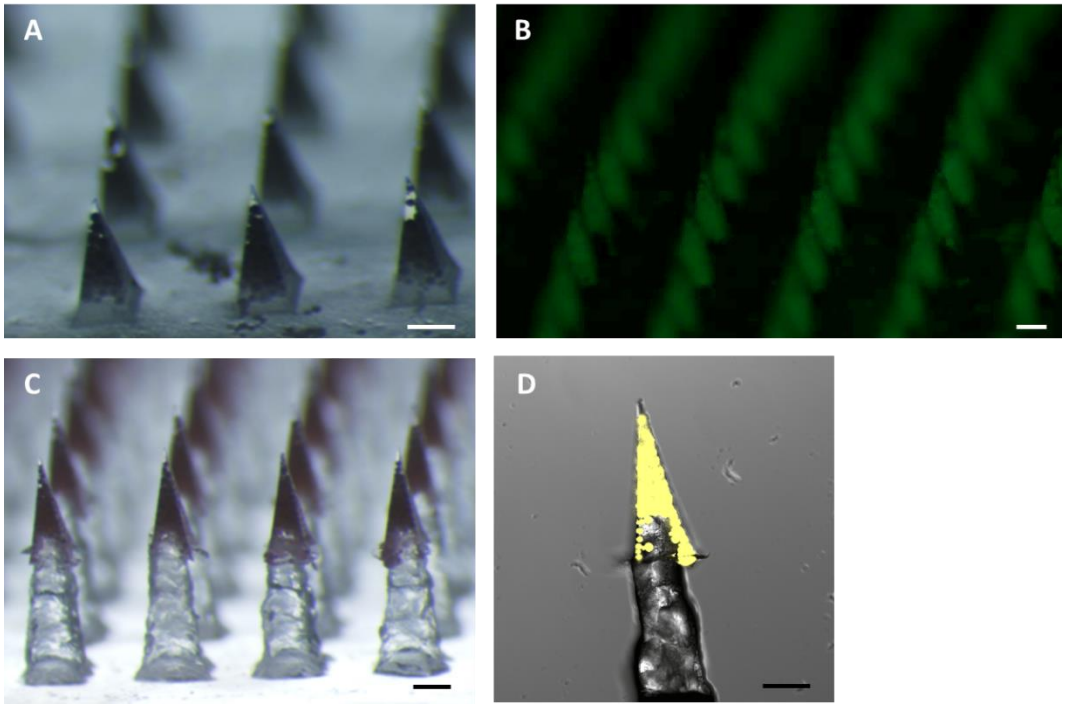

Figure 4-1: Light micrographs of microparticle-loaded microneedle patches. *A*) standard patch, *B*) fluorescent micrograph of standard patch loaded with OVA-AF488-loaded microparticles, *C*) pedestal patch with sulforhodamine B added to the first PVA/sucrose cast, and *D*) confocal image of individual pedestal microneedle containing microparticles loaded with OVA-AF647. Scale = 250 µm.

Patch Design	Microparticle mass/patch	OVA mass/patch	% MPs Delivered
Standard	244 µg (8)	4.0 µg (.0)	25% (11%)
Pedestal	208 µg (9)	3.4 µg (.0)	55% (8%)

Table 4-1: Microparticle and antigen mass contained within a single standard or pedestal microneedle patch. % MPs delivered represents the percent of microparticles delivered to the tissue after a 20 minute application on live mice. (SEM)

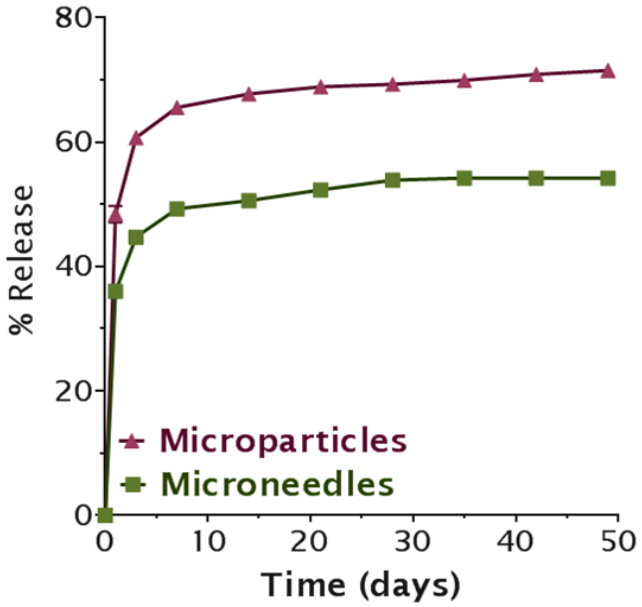

Figure 4-2: Microneedle patches demonstrate controlled release of soluble antigen over approximately one month, and follow similar kinetics to the microparticles. Microneedles were washed of PVA/sucrose binding material prior to release. *n*=3, ± SEM

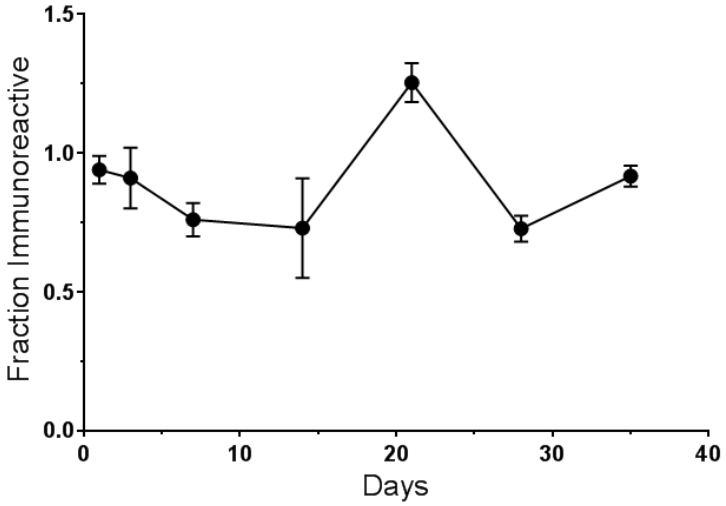

Figure 4-3: Antigen released from microneedles remains immunoreactive. Immunoreactivity was defined as the ratio of concentration as determined by SEC to concentration determined via ELISA. *n*=3, ± SEM.

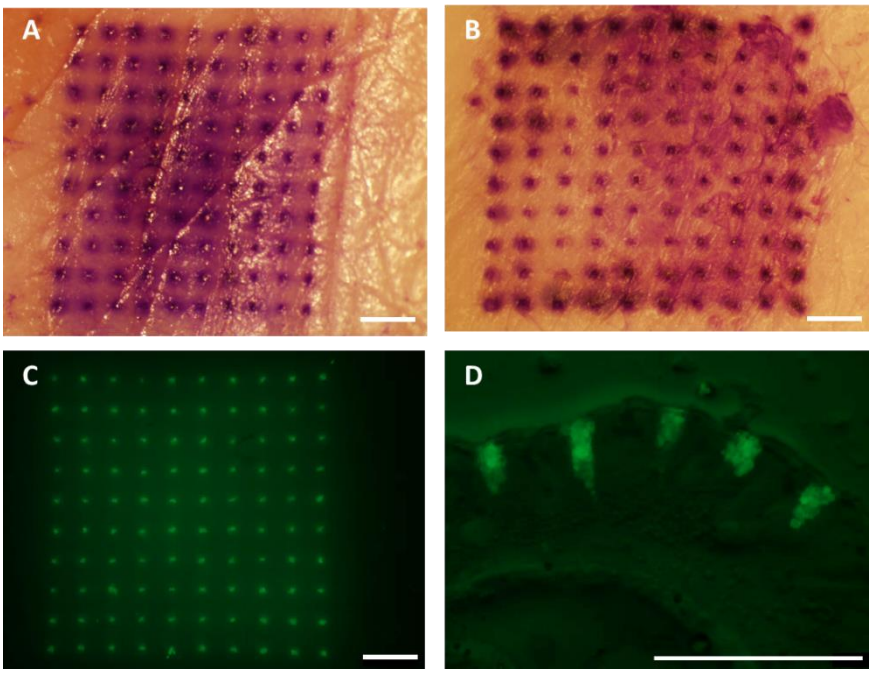

Figure 4-4: Microneedle patches readily penetrate skin and deposit microparticles intradermally. *Top*) Micrographs of excised porcine skin after application and staining. *A*) Standard patch, *B*) Pedestal patch. *Bottom*) Fluorescent micrographs of tissue after application of pedestal patch loaded with OVA-AF-488-loaded microparticles. *C*) Overhead, *D*) Cross-sectional. Scale = 1 mm.

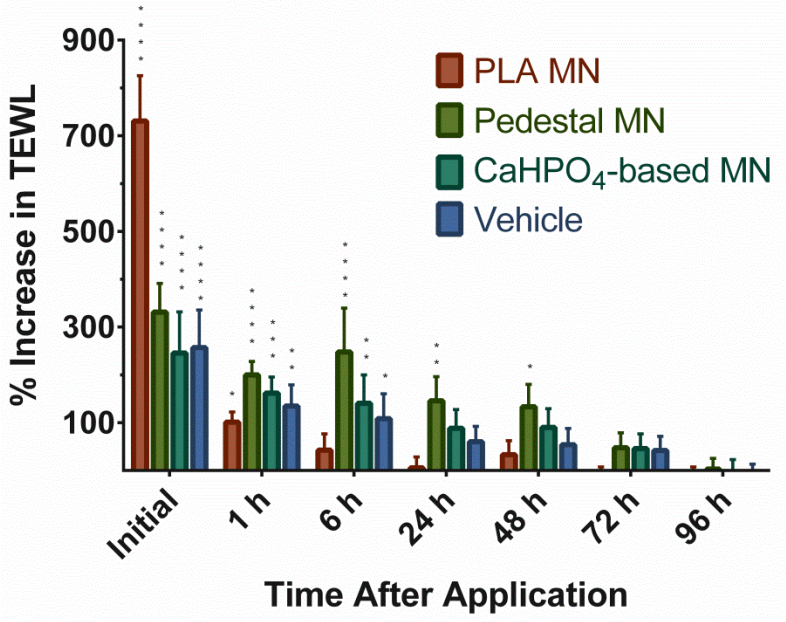

Figure 4-5: Skin resealing as measured by TEWL after application of various microneedle patches. Unoccluded microchannels made by non-dissolving PLA patches reseal rapidly, while wounds with deposited material reseal slower, with larger occlusions taking the longest. **** p <.0001, *** p < .001, ** p <.01, * p < .05. *n*=8, ± SEM.

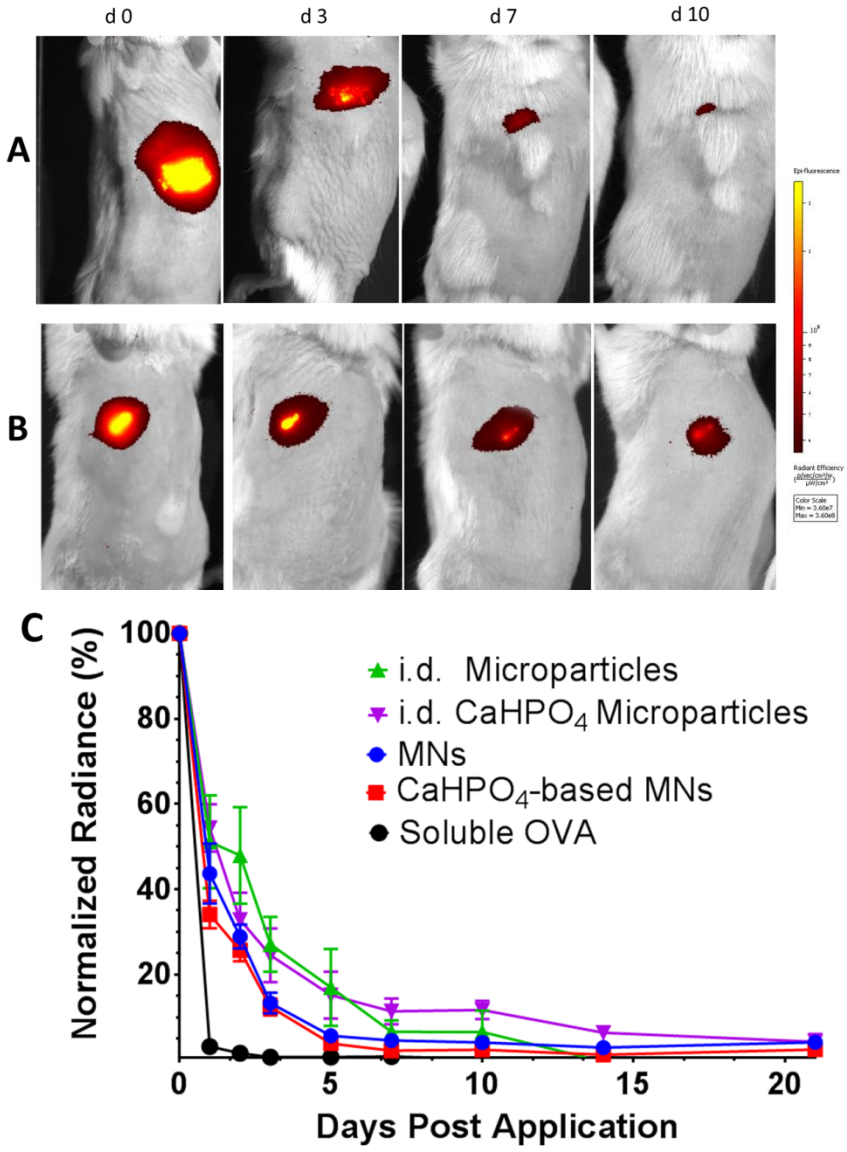

Figure 4-6: OVA-AF647-loaded ASE microparticles remain in the skin for several days following intradermal administration from *A*) microneedles, or *B*) i.d. injection. *C*) Normalized radiance quantification of OVA-AF647 signal at the application site, *n*=8, ± SEM.

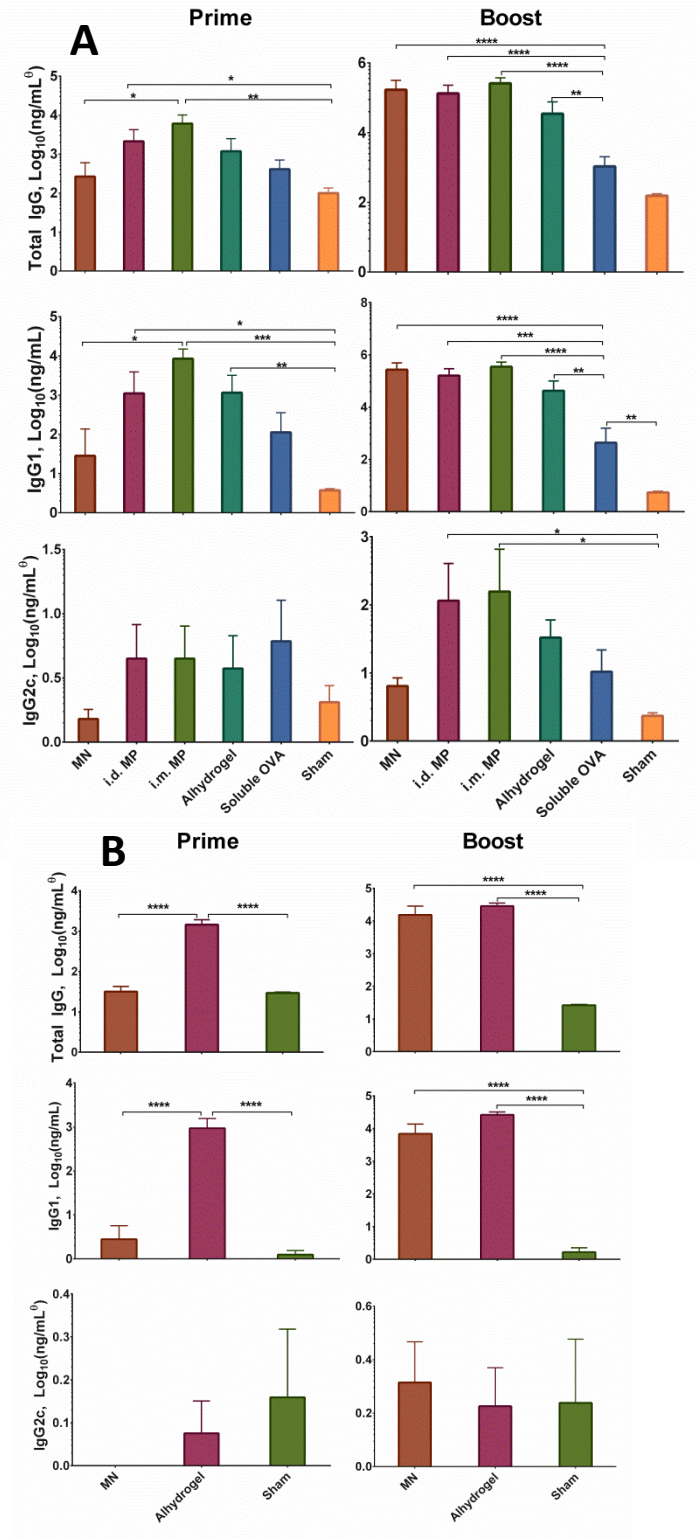

Figure 4-7: ASE microparticles and microneedles generate a robust antibody response. Serum IgG levels at day 20 (*Left*, prime) and day 42 (*Right*, boost).
A) OVA-immunized groups, *B*) rHBsAg-immunized groups. *n*=5, ± SEM
$^{\Theta}$ Concentrations were determined using an IgG1 standard, and may not be absolute for other IgG isotypes. **** p <.0001, *** p < .001, ** p <.01, * p < .05.

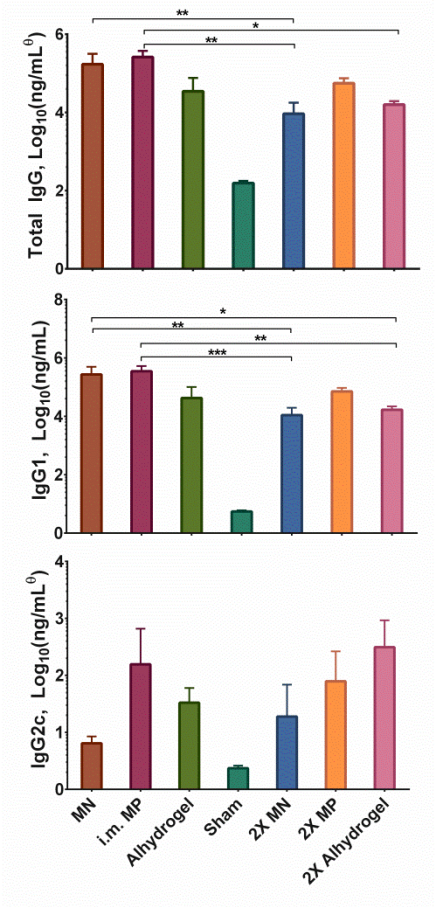

Figure 4-8: Controlled release potential of ASE microparticles and microneedles. An equivalent dose was given either split between prime and booster doses, or given all at once during prime (2X). *n*=5, ± SEM,*** p < .001, ** p <.01, * p < .05.

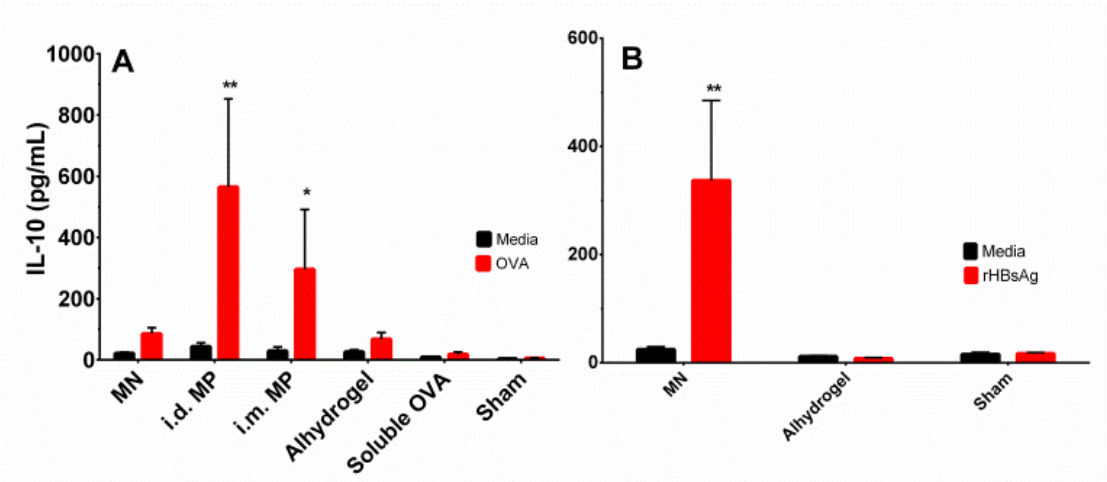

Figure 4-9: Splenocytes restimulated with OVA (*A*) or rHBsAg (*B*) produce considerable amounts of IL-10, indicative of a Th2-type immune response. *n*=5, ± SEM, ** p <.01, * p < .05.

4.7 Supplementary Material

4.7.1 Preparation and Loading of ASE Calcium Phosphate-based PLGA Microparticles

Smaller ASE PLGA microparticles (median diameter = 7.1 μm) that utilized calcium phosphate in place of Alhydrogel were also fabricated. A detailed overview of these microparticles is available elsewhere (48).

4.7.2 Determination of Antigen-specific $CD8^+$ Cells in Peripheral Blood

Antigen-specific $CD8^+$ cell populations in peripheral blood were evaluated on day 28 (7 days post-boost) via an MHC tetramer assay as previously described(34). Briefly, whole blood was collected via submandibular bleed and lysed with ACK lysis buffer and washed with PBS + 1% BSA. The Fc receptor was blocked with CD16/32 antibody. Cells were then incubated with PE-labeled tetramer (SIINFEKL for OVA groups, IPQSLDSWWTSL for rHBsAg groups – the rHBsAg tetramer was only available for BALB/c-background mice) (from MBL International) for 30 mins on ice, followed by addition of anti-CD8-APC conjugate for an additional 20 mins. Cells were washed and then incubated with DAPI to discriminate live and dead cells. Samples were stored on ice until read on a Beckman Coulter CyAn 5 flow cytometer with data processing in FlowJo software.

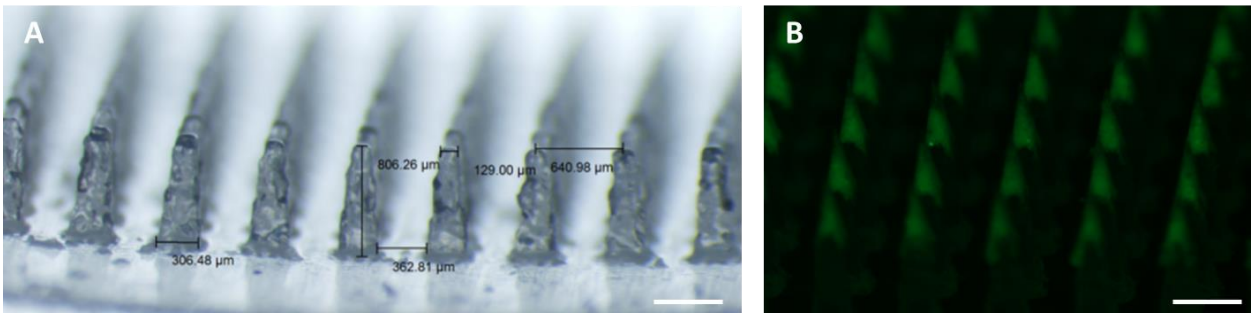

Supplementary Figure 4-1: *A*) 3D printed pedestal master part. *B*) Fluorescent micrograph of a pedestal patch loaded with OVA-AF488-loaded microparticles. Scale = 500 µm.

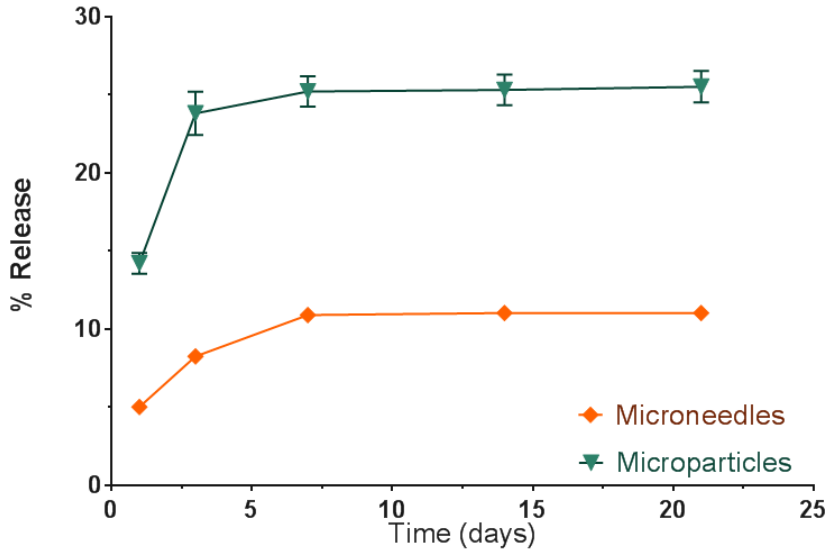

Supplementary Figure 4-2: *In vitro* release of soluble rHBsAg from microneedle patches and microneedles. *n*=3, ± SEM.

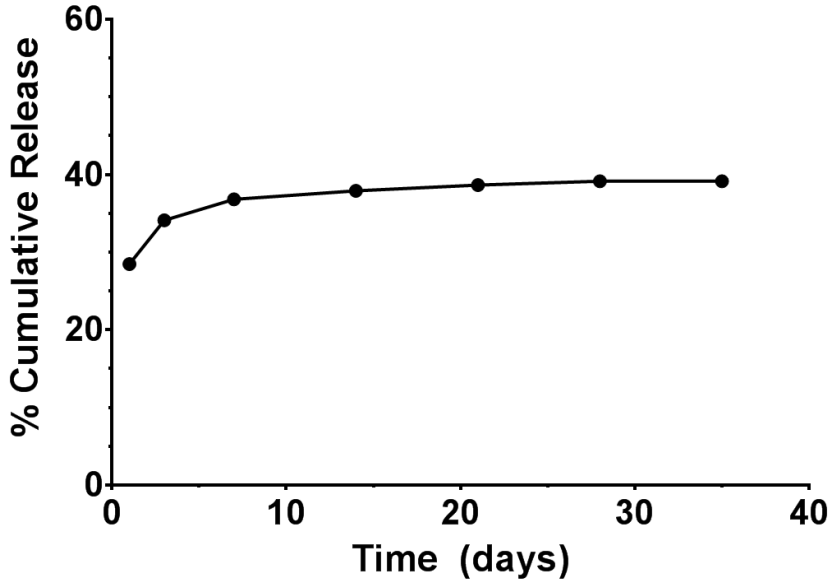

Supplementary Figure 4-3: *In vitro* release of OVA-loaded ASE microparticles after unprotected lyophilization.

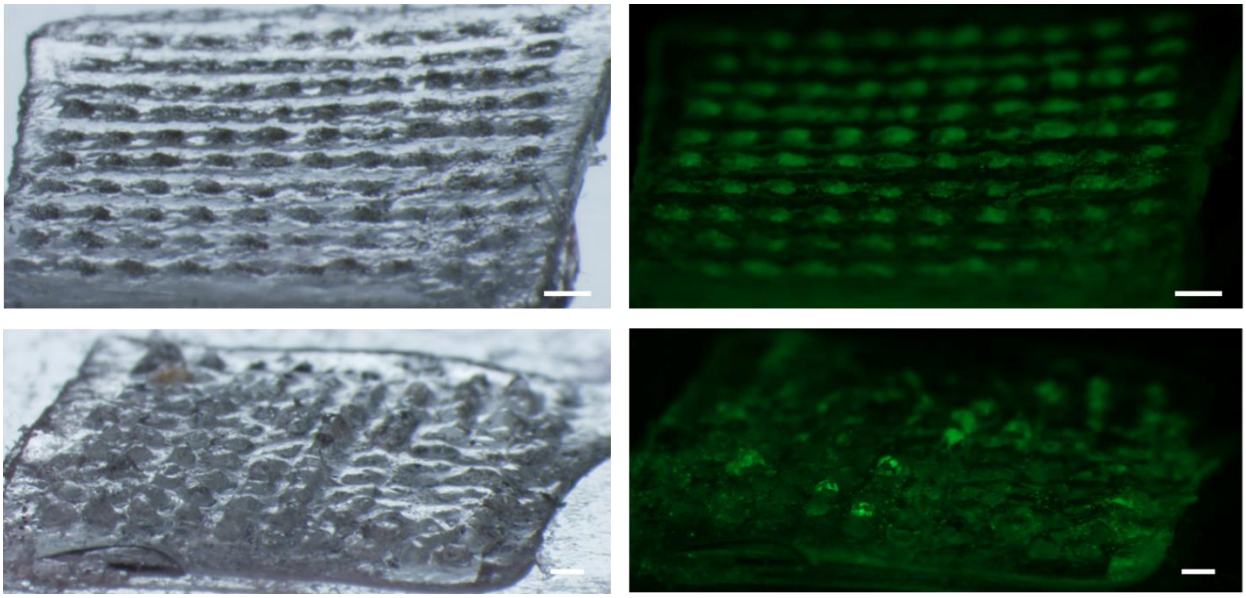

Supplementary Figure 4-4: Stereomicrographs of (*Top*) standard, and (*Bottom*) pedestal patches after application to mice. Right images emphasize microparticles via fluorescent imaging.

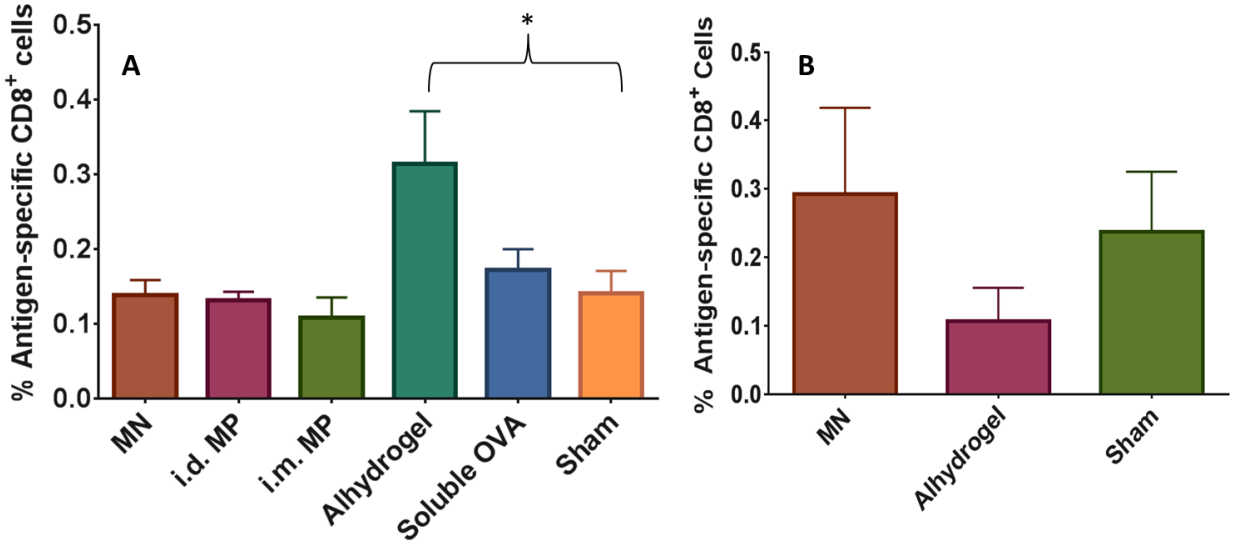

Supplementary Figure 4-5: Neither MNs or MPs show a considerable OVA (*A*), or rHBsAg (*B*), specific $CD8^+$ response at d 28. Alhydrogel produced a statistically significant but still very weak response. * $p < .05$, $n=5$, ± SEM

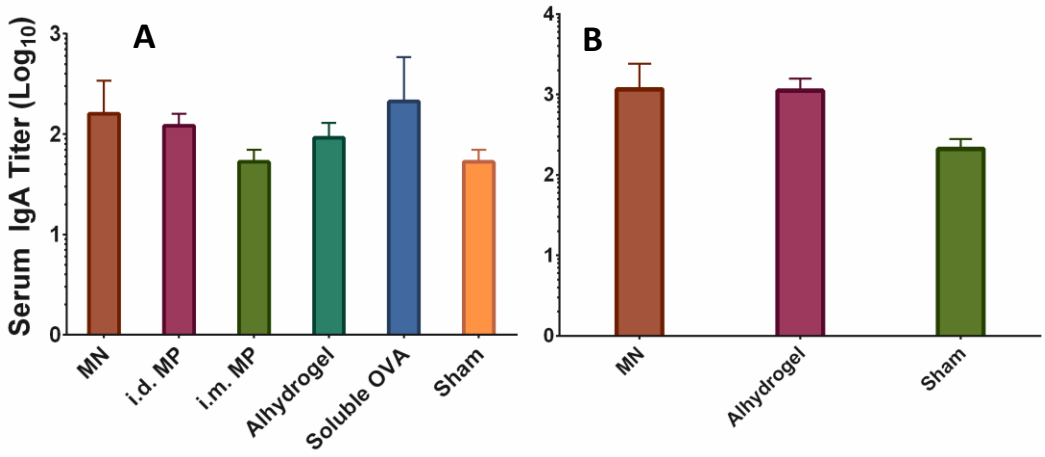

Supplementary Figure 4-6: Serum IgA titers at day 42 after immunization with *A*) OVA, and *B*) rHBsAg. *n*=5, ± SEM.

Chapter 5: Conclusions, Significance, and Future Work

The work presented in this thesis is grounded in the understanding, development, and utility of the Active Self-Encapsulation (ASE) loading technique. As pharmaceutical discovery and development starts to utilize more sensitive biomacromolecules, ASE is likely to be more heavily utilized in controlled release systems, and thus a deeper understanding and operational framework will be important.

In Chapter 2, the self-healing of PLGAs is studied directly in a film model. Self-healing is the phenomenon on which ASE is based, and thus a deep mechanistic understanding of it is critical to successful utility. The primary conclusions of the work are that self-healing is driven by high surface tension, which causes creep of the amorphous polymer when $T > T_g$. This is resisted by the polymer's ability to flow (viscosity). The rate of self-healing is thus dependent on the polymer type, the environment, residual stress left from fabricating the polymer device, temperature, and the geometry of the pores. This is the first time that self-healing has been studied directly in PLGAs, and these conclusions have direct influence on the utility and limitations to future ASE systems.

One of the limitations found in Chapters 2 and 3 are long healing times required for full pore closure. While Chapter 2 points out ways in which self-healing can be accelerated, such as high temperatures or hydrophobic polymer end-groups, such alterations are not always feasible. Thus, future work should focus on external methods for accelerating self-healing without significantly damaging the polymer or

therapeutic. Possible options are weakly penetrating or selective heat sources, surface tension-modifying excipients, or creating microparticles with a high number of smaller pores. This could reduce the required healing time to a few hours or less and create a more viable option for point-of-care compounding. This would also help overcome the thermoliability issues seen with some antigens utilized in Chapter 3, and allow a greater number of therapeutics to be utilized in ASE systems.

Chapters 3 and 4 are dedicated to showing the utility of ASE-based microparticles both by themselves, and as part of a more complex delivery system involving microneedles. Chapter 3 builds on previous work exploring ASE and shows its versatility by successfully encapsulating and releasing a variety of vaccine antigens from the same batch of microparticles. It also delves deeper into the various stages of antigen release. The work suggests initial burst release is caused by soluble antigen desorbing from Alhydrogel (trapping agent) and then diffusing out of the microparticles. This is followed by a second phase of Alhydrogel-complexed antigen releasing after physical degradation of the microparticles.

While Chapter 3 is successful in showing that ASE works with a variety of antigens, it also suggests that the choice of trapping agent may in fact be more critical than previously thought. Because of Alhydrogel's adsorption mechanisms and the challenges of completely healing all surface pores, the desorption of antigen from Alhydrogel becomes the rate-limiting factor in the early stages of release. Thus, burst release will vary greatly and with limited control as different antigens are utilized. Instead, it may be desirable if different antigens could have the same or similar release profile. Future work could thus focus on selecting a more uniformly applicable trapping agent that will adsorb and desorb to different antigens will similar strength

and kinetics. Alternatively, it could be possible to utilize a mix of different microparticle formulations each working with different loading and/or release mechanisms such that no one formulation is expected to work with all antigens across all stages of release, but is such that the mix of formulations produces a consistent outcome with different antigens.

If the aforementioned limitations can be overcome, the resulting drug delivery platform would have enormous potential. As previously mentioned, healthcare providers the world over could keep stocks of these unloaded microparticle formulations, and then load/compound them with various antigens or other therapeutics *pro re nata* on a case-by-case basis to create long-lasting or single-administration medications.

Chapter 4 focuses entirely on utilizing ASE microparticles in a novel drug delivery system based on microneedles. Microneedle-based systems eliminate reliance on hypodermic needles, which are currently a major hurdle to improving worldwide public health. While the microneedle field is currently receiving a lot of research, very little of it attempts to add long-term controlled release elements, which could lead to the development of a self-administered single-administration vaccine. The work done in Chapter 4 outlines proof-of-concept development and testing of such a system utilizing the ASE microparticles explored in Chapter 3. The platform designed was fairly straightforward, but proved effective in most of the target areas. Each patch could hold ~4 μg of antigen (inside of microparticles), was strong enough to penetrate skin, and deposited its payload intradermally. The result was a potent immune response that was as good as or better than traditional vaccination options, but did not require a hypodermic needle and was freeze-dried for easy storage/transport.

While the results were promising, many improvements would be needed for such a patch to advance towards clinical development. First, future work should consider methods for increasing the dose that can be stored and delivered in a single patch. This could include simple options such as increasing the number of microneedles per patch, utilizing larger needles, or creating microparticles capable of higher antigen loading. One of the biggest limitations not only to the microneedle system developed here, but to many similar systems, is the efficacy with which the patches deliver their dose. Without a pedestal, only 25% of the encapsulated microparticles were delivered. Even with a pedestal, this jumped to only 55%, thus effectively wasting half the dose. More research is needed to develop optimal pedestals patches, which should possess greater mechanical strength than those developed here, with emphasis on a greater ability to penetrate the skin more deeply. This also includes possible improvements to pedestal geometry, as well as the material used to construct the pedestal and the microneedles. The material should be biocompatible, soluble so to leave no potentially biohazardous waste, and rapidly disintegrating to reduce application time. Lastly, microneedle patches should be evaluated in conjunction with post-application topical therapies such as bandages, creams, or ointments. A secondary application could add several benefits to the system, such as to aid in wound healing, help retain the microparticles in the skin, or even possibly to act as an additional adjuvant and further direct the immune response to the application site.

It is intended that the work outlined in this thesis will act as a base of knowledge and experimental proof-of-concept for future studies to expound on the potential of Active Self-Encapsulating controlled release systems, as well for inclusion of such systems into microneedle patches.

Appendix A: Modeling and Predictions of Self-healing Pores in PLGAs

A.1 Abstract

Self-healing of pores in Poly(lactic-*co*-glycolic acid)s (PLGAs) plays an important role in the encapsulation and controlled release of drugs from PLGA microparticles. Despite the importance of this phenomenon, neither the mechanics of the deformation nor the material properties that control it have been fully studied. In this study, the material properties of PLGA have been characterized using mechanical tests, and a finite-element model has been developed to predict how pores heal. This model assumes that the healing process occurs by viscous flow resulting from the deviatoric stress field induced by the interaction between the surface curvature and the surface tension of the PLGA. The simulations, which incorporate measured material properties, show good agreement with experimental observations. However, annealing processes that occur over prolonged times increase the viscosity and slow the healing times of PLGA films at intermediate temperatures above the glass-transition temperature. These findings may be reasonably applied towards the prediction of healing processes in PLGA and in related biomaterials for important biomedical applications such as drug delivery.

A.2 Introduction

A.2.1 Motivation

Poly(lactic-*co*-glycolic acids) (PLGAs) forms the basis of some of the most widely-used biomaterials today. Since their first patented use in the 1960s, they now form key components of many products that have been approved by the US Food and Drug Administration, such as sutures (1), cardiovascular stents (2-4), skin implants (5, 6), and a plethora of drug-delivery devices such as microparticles (7-9), patches (10), and *in-situ* forming gels (11). Several characteristics make PLGAs attractive for medical applications. They have excellent biocompatibility, and their degradation kinetics and mechanical strengths can be easily tailored by altering molecular weights, monomer ratios, lactide isomer content, and type of end-capping. In addition, glass-transition

temperatures (T_g) near body temperature result in desirable *in vivo* release-behavior of drug-delivery systems with enhanced shelf-lives. Despite the prevalent use of PLGAs, the associated scholarly literature often does not focus on analyses of their material properties. There have been reports on the moduli of PLGA products, but very little work has been reported on the underlying physics and mechanics of the deformation behavior. An understanding of this behavior will become increasingly important as PLGA and related materials are used in new ways. Therefore, in the present work, we explore the constitutive properties of PLGA, with a focus on developing a model of the passive self-healing process in polymers.

Autonomous healing in polymers can be achieved by several different strategies. For example, "active" methods have been developed that rely on an encapsulated healing/filling agent, either in pores or in micro-vascular networks (12-15). Alternatively, in the absence of significant tensile stresses, voids and cracks in many materials can heal passively as a result of creep / viscous flow driven by surface tension. This process requires no chemical modification of the material, and relies only on the temperature being sufficiently elevated to ensure flow. This phenomenon can occur in many different applications from self-healing automotive paints (12), to erasable data storage (16). A major application of self-healing in PLGAs is the recent description of an aqueous-based micro-encapsulation method for bio-macromolecules (9). In this case, pores on the surface of PLGA microparticles self-heal to trap bio-macromolecules inside them, without the need for micronization and organic solvent exposure known to be deleterious to proteins. Similarly, healing has also been linked to the termination of the initial burst release and long-term release kinetics of PLGA-encapsulated large molecules (17, 18).

Porosity can be introduced in PLGAs as a result of phase transitions and associated density changes during curing (19). Furthermore, pore networks in PLGA microparticles can be created by the control of osmotic pressure differences induced by changes in the internal and external environments. Healing of these pores is critical for the quality of the encapsulation and release of drugs and peptides (9, 18). The healing process was explored in a series of model experiments by Mazzara *et al.* (20) using controlled pores that had been artificially introduced into the surface of PLGA films by blunt-tip micro-needle arrays. These experiments showed empirically that the

healing times were controlled by the visco-elastic properties of the PLGA. In this present paper, we extend this work by developing a finite-element model for pore healing. The model assumes that healing proceeds by viscous flow in response to a deviatoric stress field induced by the surface tension and curvature of the pores. The model can be used to describe pore healing in terms of the temperature and geometry. It may be useful to explain the results of past self-healing experiments. It may also be useful as the basis of a quantitative design to predict healing times corresponding to desired controlled release with PLGA dosage forms.

A.2.2 Theoretical Background

The underlying assumption of this model is that the pores heal by flow driven by internal stress fields established by surface tension effects (21, 22). In this section, we summarize the theoretical background of these two phenomena.

A.2.2.1 Constitutive Models for a Linear Polymer

The simplest representation of a linear visco-elastic material is known as a Maxwell model. The constitutive behavior corresponding to such a model can be represented by a spring (with a modulus of E_m) in series with a dashpot (with a viscosity of η_m). The dashpot represents a single thermally-activated mechanism of flow, so the viscosity is of the form

$$\eta_m = \eta_{mo} e^{Q_m/RT}, \tag{1}$$

where Q_m is the activation energy of the relaxation mechanism leading to flow, R is the molar gas constant, T is the absolute temperature, and η_{mo} is a material constant. The characteristic relaxation time (τ_m) of a Maxwell model is given by

$$\tau_m = \eta_m / E_m = \tau_{mo} e^{Q_m/RT}, \tag{2}$$

where τ_{mo} is a material constant. A time-dependent modulus, $E(t)$ can be defined for a polymer as the ratio of the stress at a given time t that results from a fixed strain:

$$E(t) = E_m e^{-t/\tau_m}, \tag{3}$$

The fully-relaxed modulus of a Maxwell solid, given by $t \to \infty$, is zero. This is important in the present context, because pore healing can only occur when the fully-relaxed modulus approaches zero.

While a Maxwell model describes some important characteristics of a polymer that exhibits pore healing, polymers generally exhibit more than one relaxation mechanism. Some of these mechanisms may allow for complete relaxation of polymer, while others may allow only partial relaxation. Each mechanism will have its own activation energy and characteristic relaxation time, and can be represented by an assembly of elements consisting of linear springs and dashpots. The time-dependent deformation of a polymer can then be modeled as the resultant of such an assembly. The individual moduli and viscosities that go into such a model are determined by fits to the observed response of the polymer at different time scales through experiments such as dynamic mechanical analyses (DMA) and stress-relaxation tests, as described below.

A.2.2.2 Role of Surface Energy and Curvature

The chemical potential of an atom or molecule at the surface of a material depends on the product of the surface energy (surface tension) and the local surface curvature. Gradients in this potential provide a driving force for the material to change its shape, either by diffusion of atoms or molecules along the surface, or by bulk deformation in response to deviatoric (shear) stresses established within the body of the material. In the present work, we assume that bulk flow is the dominant mechanism; this is consistent with the experimental results presented later.

The internal stress field associated with a surface (or interface) is established by the change in normal stress (σ_n) across a curved surface, as given by the Young-Laplace equation:

$$\sigma_n = \gamma\left(\kappa_1 + \kappa_2\right), \tag{4}$$

where γ is the surface tension of the material, and κ_1 and κ_2 are the local principal curvatures. A convex surface results in a compressive normal stress at the surface and a concave surface results in a tensile stress at the surface. The internal stress field induced by surface curvature is exactly equivalent to the stress field induced by

applied surface tractions that are normal to the surface and have a magnitude given by Equation 1. This equivalence between the stresses induced by surface curvatures and those induced by applied surface tractions forms the basis for the analysis used in this paper.

A.2.2.3 Pore Healing

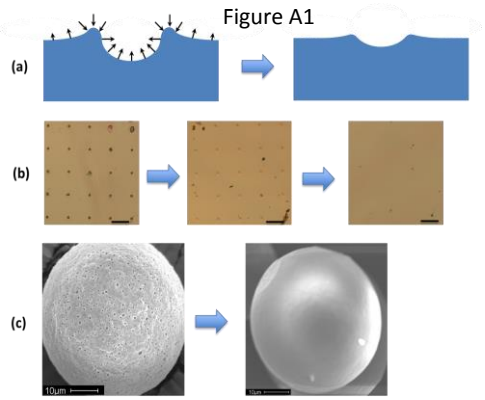

Figure A1

The healing of a surface indent is illustrated in Fig A1. The indent is initially formed by the application of a localized external pressure during indentation of a freshly-spun PLGA film. This creates large deviatoric stresses to which the polymer responds by rapidly flowing and forming an indent. The effects of surface energy at this stage are relatively small compared to the effects of the indentation stress field, so surface features such as a lip around the indent can often be retained (20). (Even when the indentations are square, the surrounding lip is approximately circular). When the indenter is removed and the film dried, deformation is driven by the deviatoric stress field that is established by the surface tension and curvatures. (A residual stress field resulting from the indentation can also contribute to this deformation; in the present work, we assume this is relaxed by flow during the indentation process.) The resulting stress field can be visualized and modeled by considering equivalent surface tractions, as shown in the schematic of Fig A1. Provided the fully-relaxed modulus is significantly smaller than the stresses induced by the surface curvature, the material can flow to smooth out any surface curvatures. Both the depth of the indent and the amplitude of any lip formed around the indent will decay over time.

For an incompressible linear-viscous material, the deformation field that results from a deviatoric stress field can be calculated using the Levy-Mises flow rule (23):

$$\frac{\dot{\varepsilon}_1}{\sigma_1 - 0.5(\sigma_2 + \sigma_3)} = \frac{\dot{\varepsilon}_2}{\sigma_2 - 0.5(\sigma_1 + \sigma_3)} = \frac{\dot{\varepsilon}_3}{\sigma_3 - 0.5(\sigma_1 + \sigma_2)} = \frac{\dot{\tilde{\varepsilon}}}{\tilde{\sigma}} = \frac{1}{3\eta}, \qquad (5)$$

where $\dot{\tilde{\varepsilon}}$ and $\tilde{\sigma}$ are the von-Mises effective strain rate and stress, and $\dot{\varepsilon}_i$ and σ_i (i = 1, 2, 3) are the principal strain rates and stresses. In Mazzara *et al.* (20), this approach

was used to develop a simple analytical result for healing an isolated spherical pore in the middle of a viscous material. The Lamé equations (23) for a spherical pore of radius a with an internal pressure of $p = -2\gamma/a$, give principal stresses at a distance r from the center of the pore of

$$\sigma_{rr} = \frac{2\gamma\ a^2}{r^3}; \sigma_{\theta\theta} = \sigma_{\phi\phi} = -\frac{\gamma\ a^2}{r^3}. \tag{6a}$$

The corresponding principal strain rates are given by

$$\varepsilon_{rr} = \frac{\partial u}{\partial r}; \varepsilon_{\theta\theta} = \varepsilon_{\varphi\rho} = \frac{u}{r}, \tag{6b}$$

where u is the radial displacement at a distance r from the center of the pore. Recognizing that at $r = a$, $\dot{u}(a) = \dot{a}$, and that at time $t = 0$ the initial pore radius is a_o, it was shown (20) that the pore size is given by

$$a = a_o - \frac{\gamma\ t}{2\eta}, \tag{7}$$

So, the time to heal a spherical pore is predicted to be $2\eta a_o/\gamma$.

A.3 Material and Methods

A.3.1 Numerical Implementation

Figure A2

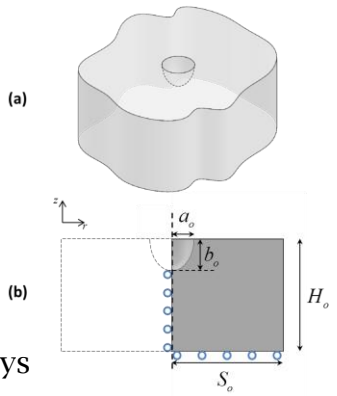

In the numerical simulation, the initial pores were assumed to be ellipsoidal, with a depth of b_o, and a half width of a_o, on the surface of a film of thickness H_o (Fig A2). The radius of the external boundaries, S_o, were set to a value of $S_o/a_o = 10$ in all simulations. It was demonstrated numerically that this value was large enough so that its effect was always limited to less than a 2% error in the calculated pore depth. The bottom of the film was assumed to be attached to a rigid substrate, but free to expand. The assumption of axisymmetric geometries allowed the calculations to be simplified, while retaining the essential elements of the experimental studies. Furthermore, since the stresses are dependent on local curvatures, there is a very large driving force for any sharp corners to be rounded out. This results in a transition to axisymmetric shapes early in the

healing process, so that details of the initial geometry have only a limited effect on the healing time. Indeed, Mazzara *et al.* (20) reported that their initially square pores quickly became circular. We used our numerical method to analyze cylindrical pores, and they evolved fairly quickly into ellipsoidal shapes. However, the initial sharp corners in a cylindrical void requires a very dense mesh for finite-element analyses. Therefore, ellipsoidal geometries were used to model the pores in the general cases presented in this paper.

Finite-element analyses were conducted using the commercial package ABAQUS. The stress fields resulting from the surface tension were induced in the finite-element model by applying tractions to the surface proportional to the sum of the principal curvatures (Equation 4). A numerical technique for calculating the curvatures has been described by Henann *et al.* (24). We used a similar approach to calculate the curvatures of the axisymmetric surfaces. Such a surface can be described by $z = Z(r)$, where z is the height above an arbitrary reference value, and r is the distance from the axis of symmetry. The sum of the two principal curvatures (twice the mean curvature) at any point on the surface is given by

$$2\kappa = \kappa_1 + \kappa_2 = \frac{\partial^2 Z/\partial r^2}{\left[1+\left(\partial Z/\partial r\right)^2\right]^{3/2}} + \frac{\partial Z/\partial r}{r\left[1+\left(\partial Z/\partial r\right)^2\right]^{1/2}} \quad . \qquad (8)$$

Thus, the calculation is reduced to a two-dimensional problem. The coordinates of an integration point A (r_A, z_A), and the coordinates of its two nearest neighboring integration points, B (r_B, z_B) and C (r_C, z_C), can be fitted to a parabola ($y'/y_o = x'^2$) in terms of a local coordinate system with an origin located at point A and aligned with the local normal direction. The sum of the principal curvatures at A is then given by

$$2\kappa = 2y_o - n_r/r \quad , \qquad (9)$$

where n_r is the radial component of the outward normal vector at A. This procedure was used to calculate the curvature, and the corresponding surface tractions, at all points on a surface. A DLOAD user-subroutine was developed and implemented in ABAQUS/Standard. The user-subroutine was verified using the simple geometries of a sphere and a cylinder. Mesh and boundary sensitivity studies were conducted empirically by changing the size of the mesh and the distance to remote boundaries,

and verifying that any influence on the results was significantly less than the uncertainty associated with the measurements of the material parameters.

A.3.2 Material Preparation

PLGA 50:50 with lauryl-ester-terminated chains, with a weight-averaged molecular weight of 55.3 kDa, and average inherent viscosity of 0.61 dL g^{-1} was provided by Lactel Inc. Details of the preparation of the PLGA films were reported by Mazzara *et al.* (20). Briefly, the polymer was dissolved in acetone (27% *w/w*), and spin-coated onto a Teflon-coated glass substrate. The films were dried for one day in a fume-hood at room temperature, and then for an additional day under vacuum at room temperature to remove excess solvent. When the films were separated from the glass substrate they had a final thickness of 16 ± 3 μm (n=3, ± SD).

A.3.3 Material Characterization

A.3.3.1 Stress Relaxation Tests

Dry films were cut into rectangular specimens of approximately 10 mm in width and 30 mm in length. Stress-relaxation tests were conducted in a temperature range of 40 ˚C to 65 ˚C using a TA Instruments RSA3 dynamic mechanical analyzer. The samples were placed in the grips at room temperature and heated to the desired temperature at 100 ˚C min^{-1}. One minute was allowed for the temperature to stabilize before a strain of 3 % was applied within 5 ms. The strain was held constant, and the corresponding stress was then measured every 0.01 second.

A.3.3.2 Dynamic Mechanical Analysis

The same instrument was used to measure the visco-elastic properties of the PLGA films by dynamic mechanical analysis (DMA). Samples were tested in uniaxial tension at a frequency of 1 Hz, with a strain amplitude of 0.1% and an initial mean force of 0.01 N. The storage modulus, E', loss modulus, E'', and loss tangent, tanδ, were measured over a temperature range of 25 ˚C to 70 ˚C, with a temperature ramp-up rate of 3 ˚C min^{-1} and a soak time of 30 seconds to reach steady state at each temperature. Three identical samples were analyzed to determine representative values and uncertainties.

Frequency sweep tests in the range of 0.001 Hz to 99 Hz with a strain amplitude of 0.1% were then conducted in a temperature range of 25 ˚C to 65 ˚C. The mean strains

in these cyclic tests were set to be 25% greater than the strain amplitudes to ensure that the specimen never went into compression. The storage modulus, loss modulus and tanδ were determined as functions of frequency.

A.3.3.3 Measurement of Surface Tension

The surface tensions of the PLGA films were determined by placing a drop of water on the films and using a goniometer to measure the polymer-water contact angle. Contact angles for each film were measured in three distinct locations, and a minimum of two samples were used for each set of conditions. The contact angles were used to calculate the tension, γ, following Berthelot's combining rule (25)

$$\gamma = \left(1+\cos\theta\right)^2 \gamma_{lv} / 4 , \qquad (10)$$

where θ is the contact angle, and γ_{lv} is the surface tension of water.

A.3.3.4 The Effects of Annealing and the Kinetics of Solvent Escape

To investigate the effects of annealing and annealing time on the visco-elastic properties of the PLGA, films were incubated at three temperatures (50 ˚C, 55 ˚C and 65 ˚C) above the T_g for various times. The properties of these films were tested using DMA and relaxation tests, as described above.

To quantify the kinetics of annealing and solvent escape, the films were subjected to thermo-gravimetric analysis (TGA). Approximately 20 mg of PLGA was placed on platinum pans and quickly heated (50 ˚C/min) to 50 ˚C, 55 ˚C and 65 ˚C. The films were held isothermally for 8 hours, and the percent change in mass was recorded. Note that glass-transition temperature data for these films were reported in our previous work (20).

Figure A3

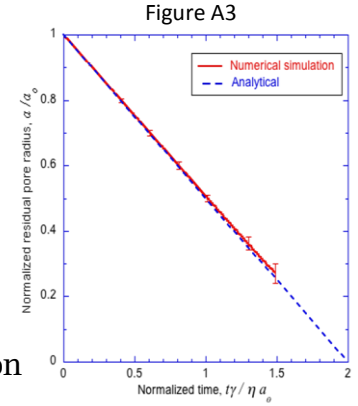

A.4 Results

A.4.1 Validation of Finite-element Model

Equation (7) gives the analytical solution for the radius of a spherical pore in an infinite body of an incompressible Maxwell solid as a function of time. As a check on the validity of our numerical technique, we repeated this calculation

numerically, using the finite-element model discussed above. A comparison between the simulation and the analytical results is presented in Fig A3, showing that the finite-element model gives the expected result. It should be noted that, in this case, the numerical calculations suffer from excessive distortion of the mesh when the pore is very small, owing to the huge normal stresses acting at the surface. For this reason, the numerical calculations shown in Fig A3 could not be taken all the way to complete pore healing.

A.4.2 Numerical Results for Surface Pores

Fig A4(a) shows how the depth of an initially ellipsoidal surface pore evolves with time for a Maxwell material. It should be noted that, in contrast to the healing of a spherical pore inside a polymer, the depth of the pore goes to zero only asymptotically. There is no well-described healing time. Instead, the healing time must be defined in terms of how long a pore takes to heal to a given percentage of its original depth. Experimentally, this will be the depth at which the pore can no longer be distinguished. Unless stated otherwise, we use a fixed percentage of 85% to define healing in the numerical simulations, since this corresponds to the point at which the healing rate starts to decay markedly. This arbitrary definition introduces a systematic error into absolute comparisons with experimental data for healing times; however, it is expected that relative comparisons will be unaffected as all the simulations will be affected equally.

Figure A4

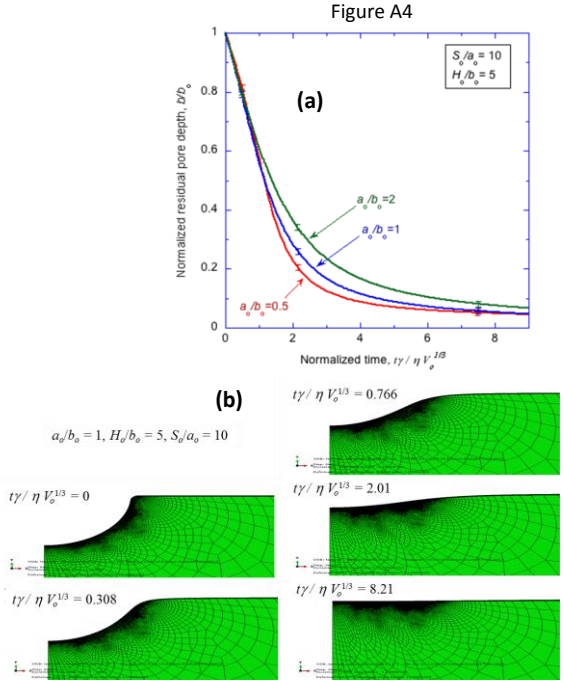

The change in the cross-sectional profile of an axisymmetric surface pore with time is shown in Fig A4b. This set of images corresponds to the simulation for which $a_o/b_o = 1$ in Fig A4a. The full animated clip from which these images are taken can be found in the supplementary material.

A.4.3 Effect of Temperature on Healing of Wet Films

We did not have the capability to do DMA and stress-relaxation tests in an aqueous environment. However, the results presented by Mazzara *et al.* (20) for the healing of pores in wet films as a function of temperature were used as a preliminary validation of the physics of the model. An activation energy of 193 kJ mol^{-1} for the viscosity of the wet PLGA films was found by fitting the healing data to an Arrhenius plot in Ref. (20). This value of activation energy was used in our finite-element calculations, with a representative value of Young's modulus E = 1 GPa. (This choice of modulus was not important for the calculations, but it is consistent with the measured value for a dry PLGA film, as described later). It is important to note that the activation energy and T_g of these hydrated films were suppressed compared to those of the dry films, owing to plasticization of the polymer by water (20).

Figure A5

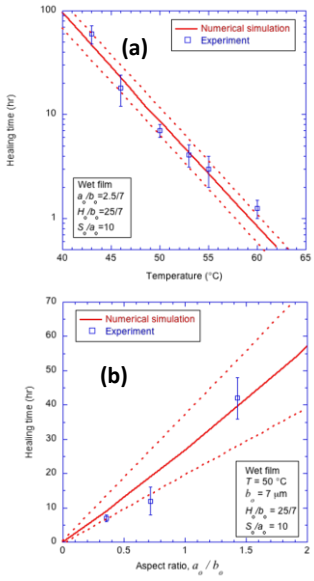

The pores in the wet PLGA had an initially square cross section, and an initial width-to-depth ratio of a_o/b_o = 5/14. By fitting the observed healing time for these pores at one arbitrarily chosen temperature of 53 ˚C to the numerical predictions for ellipsoidal pores with the same aspect ratio to heal to 85%, and using an activation energy of 193 kJ mol^{-1} for the viscosity, a value for γ/η_o could be determined as 7.9 ± 2.3 x 10^{21} m s^{-1}. This fitted value of γ/η_o was then used in conjunction with the activation energy of 193 kJ mol^{-1} for the viscosity in the finite-element model to calculate the healing time for identical pores over a range of temperatures. A comparison between the predicted healing times and the temperature is shown in Fig A5a.

The role of the initial aspect ratio and volume on healing time was also investigated experimentally in Ref. (20). The material parameters described above were incorporated into a finite-element calculation, and used to predict the healing time (again, defined as an 85% reduction in depth) for differently shaped pores. These predictions are shown in Fig A5b, and compared with the experimental observations. It should be emphasized that this comparison, unlike that of Fig A5a, does not reflect

any fits to the data. Therefore, the reasonable agreement between the predictions and experimental results provides support for the modeling.

A.4.4 Measurement of Properties for Pry PLGA Films

A.4.4.1 Stress Relaxation

Figure A6

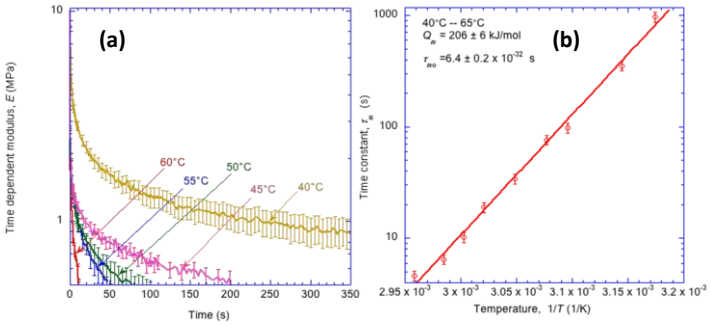

In the study described above, the material properties for wet PLGA films were determined from fits to experimentally observed data, and then used to calculate pore healing. While this shows consistency between the model and the experimental observations, a much more important question is whether it is possible to measure the material properties independently of the pore-healing experiments, and to use these properties in a numerical model to predict the healing behavior. This was the goal of the studies on the dry PLGA films for which it was possible to measure the properties.

An initial assumption was that the PLGA behaves in these stress-relaxation tests as a simple Maxwell solid with a time-dependent modulus as given by Equation 3. This equation shows that a log-linear plot of the time-dependent modulus against time should be of the form of a straight line with a slope of $-\tau_m$.

Experimental plots for the time-dependent modulus are shown in Fig A6(a) for the temperature range of 40 ˚C to 65 ˚C. These plots show a very fast initial relaxation of the time-dependent modulus followed by a slower decrease. If we assume that PLGA is a linear polymer, this initial rapid drop indicates at least one additional relaxation mechanism with a relatively short time constant. The time constant for this fast relaxation was too small to be extracted reliably from the stress-relaxation data of Fig A6(a); however, it was determined by means of DMA, as described later. At longer time scales, there does appear to be a single dominant mechanism that gives a constant slope to the stress-relaxation curves. The slopes of these lines corresponding to different temperatures were determined by a least-squares fit process, and plotted on an Arrhenius plot in the form of $\log(\tau_m)$ against $1/T$ in Fig A6(b). The slope of this line

indicates an activation energy of Q_m = 206 ± 6 kJ mol^{-1}, and a pre-exponential term of τ_{mo} = 6.4 ± 0.2 x 10^{-32} s. It can be observed that at all temperatures, the constant slope at long time scales starts when the time-dependent modulus is in the range of 1.5 ± 0.5 MPa. Using this value of the modulus for E_m in the Maxwell model, Eqns. (1) and (2) can be used to deduce a value of η_{mo} = 9.6 ± 3.5 x 10^{-32} MPa·s.

A.4.4.2 Dynamic Mechanical Analysis

The storage modulus and loss tangent for dry PLGA films computed from DMA temperature-sweep tests at 1 Hz are plotted in Fig A7(a). From this plot, the unrelaxed modulus is estimated to be 1.6 ± 0.3 GPa, being the asymptotic level that the storage modulus tends to at low temperatures. It should be noted from Fig A7(a) that the peak in tanδ is a double peak. The first peak is at about 38 ˚C, which is consistent with the estimate of Mazzara *et al.* (20) for a T_g between 35 ˚C and 40 ˚C. Here, we will neglect the fine details of the relaxation peak, and assume a single relaxation mechanism that operates at 1 Hz over the temperature range of 38 ˚C to 48 ˚C.

To extract the visco-elastic properties of the relaxation mechanisms that caused the fast initial relaxations observed in the stress relaxation tests, we conducted frequency sweep tests. Representative results of the tests are shown in Fig A7(b). The results show single peaks in the loss modulus, and they can be interpreted based on a standard-linear-solid (SLS) model. Such a model results in a time-dependent modulus of the form (26)

$$E(t) = E_r + E_s e^{-t/\tau_s} . \qquad (11)$$

In this equation, the fully-relaxed modulus, $E(\infty)$, is given by E_r, and the unrelaxed modulus, $E(0)$ is given by $E_r + E_s$. The temperature-sweep tests gave a value for this unrelaxed modulus of $E(0)$ = 1.6 ± 0.3 GPa.

A standard-linear solid also has a viscosity of the form $\eta_s = \eta_{so} \exp(Q_s / RT)$, where Q_s is the activation energy and η_{so} is a material constant. The storage modulus, $E'(\omega)$, and loss modulus, $E''(\omega)$, of an SLS are given by (26):

$$E'(\omega) = E_r + E_s \frac{\omega^2 \tau_s^{\,2}}{1+\omega^2 \tau_s^{\,2}}, \tag{12a}$$

$$E''(\omega) = E_s \frac{\omega \tau_s}{1+\omega^2 \tau_s^{\,2}}, \tag{12b}$$

where ω is the angular frequency of the input strain, and the time constant is $\tau_s = \eta_s / E_s$. The loss modulus is maximal at $\omega = 1/\tau_s$, so the time constants at different temperatures can be extracted from the peaks in the loss modulus. These are plotted as an Arrhenius plot in Fig A7(c). From this plot, the activation energy was determined to be Q_s = 250 ± 29 kJ mol^{-1}, and the pre-exponential term, $\tau_{so} = \eta_{so} / E_s$, was determined to be 6.6 ± 0.8 x 10^{-44} s.

Figure A7

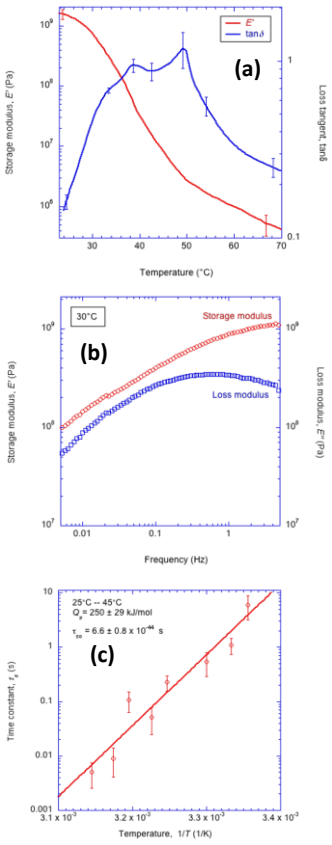

The fully-relaxed modulus, E_r, of a standard-linear solid can be determined from the difference between the storage and loss modulus at the frequency corresponding to the maximum loss modulus (Equation 12 A and B). In the present case, there was a slight dependence of the relaxed modulus on temperature. This indicates the presence of additional fast relaxation mechanisms, which are ignored in the present analysis. However, the relaxed moduli measured from the peaks in the loss modulus are consistent with the value of 1.5 ± 0.5 MPa determined from the stress-relaxation experiments for E_m.

Combining the results from the stress-relaxation tests and the frequency-sweep tests, we propose a material model for dry PLGA films as shown in Fig A8(a). The model consists of a standard-linear solid in series with a dashpot, and has a time-dependent modulus of

$$E(t) = \left(E_r + E_s e^{-t/\tau_s}\right) e^{-t/\tau_m}. \tag{13}$$

In this model, the standard-linear solid provides a time-dependent initial modulus for the Maxwell dashpot. The parameters for the different elements of the model are summarized in Table 1. The Maxwell dashpot with a viscosity of η_m dominates the healing process and is the one we are particularly interested in when analyzing the healing process. The dashpot associated the standard-linear solid, with a viscosity η_s, is associated with relaxing 99.9% of the instantaneous modulus, but it has no significant effect on healing. When this model is used in a finite-element code, it needs to be converted to the form shown in Fig A8(b), which is the equivalent Prony-series representation. In this figure, $E_1 = E_s$, $E_2 = E_m$, $\eta_1 = (1/\eta_s + 1/\eta_m)^{-1}$, and $\eta_2 = \eta_m$. A Prony-series representation requires a non-zero fully-relaxed modulus. Therefore, an arbitrary value of E_3 was chosen that was sufficiently low so as not to impede the healing.

Figure A8

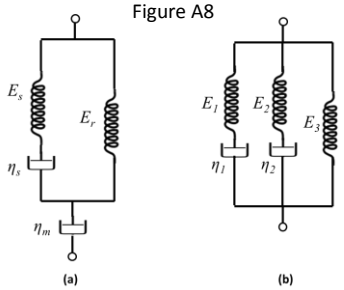

Table A1: Values of parameters of the unannealed dry PLGA (See Fig. A8a)

	E_s [MPa]	(1.6 ± 0.3) x 10^3
	E_r [MPa]	1.5 ± 0.5
	η_o [MPa·s]	Q (kJ mol^{-1})
η_s	(1.1 ± 0.3) x 10^{-40}	250 ± 29
η_m	(9.6 ± 3.5) x 10^{-32}	206 ± 6

A.4.4.3 Interfacial Tension for Dry PLGA

The water-polymer contact angle for the PLGA films used above was measured to be 71.8 ± 1.4°. Using the Berthelot combining rule and a water-air interfacial tension of 72.70 mN m^{-1} (25), the surface energy of dry PLGA films was calculated to be γ = 31.0 ± 2.0 mN m^{-1}.

A.4.5 Prediction of Healing Himes for Pores in Dry PLGA Films

Finite-element calculations of pore healing in dry PLGA films using the material properties described above were performed. Axisymmetric ellipsoidal pores with an aspect ratio a_o / b_o = 2.5/7 and a pore volume of 91.6 μm^3 were used to match the values from the experimental study (20). The predicted healing times are plotted as a

function of temperature in Fig A9, along with the experimental results. Three different contours of different healing levels are plotted in Fig A9, showing the effect of small changes in the definition of healing.

Figure A9

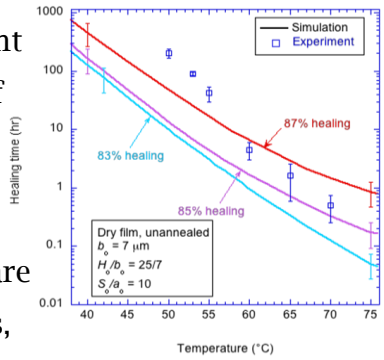

A.5 Discussion

While Fig A9 shows that the numerical predictions are generally consistent with the experimental observations, the experimental healing times appear to be significantly longer than expected at lower temperatures. It is conjectured that this is a result of changes in material properties associated with annealing, as a result of relatively long healing times at low temperatures. In particular, the films used in the study had significant residual solvent content. This excess solvent acts as a plasticizer for the polymer, effectively decreasing its viscosity and T_g (27). Consequently, any loss of this solvent over long periods of times may cause an increase in the viscosity and T_g and a corresponding increase in the healing times. This is consistent with the common observation of a higher T_g during the second heating cycle of differential scanning calorimetry (20).

To elucidate the effects of annealing, samples of the PLGA were held isothermally in a TGA experiment for 8 hours at temperatures of 50 ˚C, 55 ˚C and 65 ˚C (Supplementary Fig A1). The initial rate of solvent evaporation increased with temperature. However, after two hours, there was no significant further evaporation, and the final weigth loss indicated that the initial residual solvent content had been about 1.7%. The weight loss during the first one hour was fitted to the equation:

$$w_{loss}(t) = C_1\left(1 - e^{-At}\right) \quad , \tag{14}$$

where C_1 is a constant, which is the asymptotic value of the weight of the evaporated solvent at long time scales, and A is a temperature-dependent rate parameter. By fitting the data within the first hour (when most drastic weight loss occurs) using Equation 14, and plotting the parameter A on an Arrhenius plot, the activation energy of this solvent escape process was determined to be 55 ± 1.3 kJ mol^{-1}.

The most important visco-elastic property of the films, from the perspective of pore healing, is the viscosity represented by the second dashpot (η_m) in Fig A8a. The effects of annealing on viscosity were investigated by holding the films isothermally at 65 ˚C for up to two hours. DMA was then used to measure the T_g, and stress-relaxation measurements were used to determine the viscosity. These results showed that annealing raised the T_g, increased the viscosity and dropped the activation energy, but the instantaneous modulus was not significantly affected. These changes are summarized in Table A2 for different annealing times at 65 ˚C. It should be noted that the time scales over which the relaxation data were obtained (see Fig A6a, for example) were much smaller than the time scales over which significant annealing might occur. Therefore, it is believed that annealing did not occur while the relaxation data were being collected.

Table A2: Parameters for the dry PLGA after annealing at 65 °C.

Annealing time [hours]	T_g [°C]	η_{mo} [MPa·s]	Q_m [kJ mol^{-1}]
0	38.4 ± 0.3	(9.6 ± 3.5) x 10^{-32}	206 ± 6
0.5	47.0 ± 0.3	(2.0 ± 0.2) x 10^{-20}	140 ± 10
1	49.5 ± 0.3	(2.0 ± 0.2) x 10^{-22}	150 ± 10
2	50.8 ± 0.3	(2.8 ± 0.2) x 10^{-22}	150 ± 10

In addition to changes in the bulk properties of the PLGA, measurements of the contact angle suggested that the polymer-air interfacial tension may also change significantly as a result of solvent evaporation and annealing. In particular, annealing at 65 ˚C for two hours gradually reduced the interfacial tension from 31 ± 2 mN m^{-1} to 25 ± 3 mN m^{-1}.

Figure A10

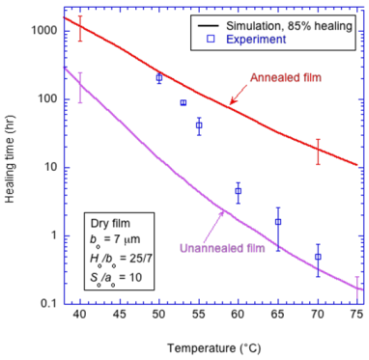

Finite-element simulations of pore healing were performed using the most extreme values of the material properties given in Table A2 (to provide an upper bound on the healing time). These results are presented in Fig A10. As can be seen from this figure, while the use of the unannealed properties provide excellent predictions for the behavior at high temperatures, the use of

annealed properties provide better predictions at the lower temperatures. At the higher temperatures, the total time required to heal the film is comparable to the annealing time, so most of the healing occurs before full annealing. However, at lower temperatures, the time scales for annealing are smaller than the time scales for healing, so the results are more affected by the annealing. This is expected since the activation energy for solvent evaporation of 55 ± 1.3 kJ mol^{-1} is smaller than the activation energy for viscous flow. The differences between the simulations for an annealed and unannealed film reflect different values for surface tension, viscosity, and T_g, all of which appear to change during annealing of a film.

In many materials, surface pores can also heal by surface diffusion; for example, this is the mechanism often ascribed to the healing of pores in high-temperature ceramics (28-30). However, this does not appear to be the case for PLGA. First, the healing data does seem to be quite well described by the visco-elastic properties of the PLGA. Second, surface diffusion tends to have a lower activation energy than the bulk diffusive processes responsible for flow. This would decrease the healing time at low temperatures below that predicted from viscous flow. The opposite trend was observed, so the discrepancy in healing times is not a result of surface diffusion; rather it is a result of solvent evaporation, as discussed above.

Finally it is interesting to consider how these changes might correlate to pore healing in PLGA microparticles. These are generally dried to remove excess water and solvent, so there is expected to be a low solvent content during incubation. However, water is known to plasticize PLGA so, upon hydration of the polymer, the glass-transition temperature would drop, as it does in the presence of residual solvent. Furthermore, the pores in the microspheres can vary considerably in size, from roughly 10 nm up to 10 μm. These compound effects of variability in T_g and a range of pore sizes, would make the application of the analysis presented here to PLGA microspheres a logical application to model the influence of healing on the long-term release of macromolecules.

A.6 Conclusions

Self-healing in PLGA can be modelled by viscous flow driven by internal stress fields established by surface-tension effects. A finite-element model incorporating a

numerical method to calculate the evolution of surface curvatures was developed to analyze indent healing in visco-elastic materials. The rate of healing for surface pores decreases as the pores heal, with the pore depth approaching zero asymptotically. The visco-elastic properties of PLGA films were characterized using a combination of DMA and stress-relaxation tests. The dry PLGA films used in this study had a relatively high instantaneous modulus of 1.6 ± 0.3 GPa, and a glass transition temperature of 38.4 ± 0.3 ˚C, owing to reduced solvent content. The PLGA displayed relaxation mechanisms with at least two distinct time scales. The first mechanism is a fast one with a very short time constant; this reduced the modulus by 99.9% at a time scale of less than a minute at temperatures above glass transition temperature, leaving the film with a partially-relaxed modulus of 1.5 ± 0.5 MPa. This modulus, although much smaller than the instantaneous modulus, is still too large for healing to occur. A second relaxation mechanism with a much longer time constant was responsible for viscous flow that could accommodate pore healing.

Finite-element simulations of indent healing using material properties that had been independently measured were broadly consistent with earlier experimental observations reported by Mazzara *et al.* (20). It was noted that annealing of the films, which is associated with solvent evaporation, resulting in longer healing times than expected at lower temperatures.

Since the healing mechanism is thermally activated, temperature is one of the most important factors in self-healing of PLGA. The temperature needs to be high enough for viscous flow to occur during the time scales of interest. In addition to the temperature, the indent geometry also affects healing time, with larger indents requiring longer time to heal. While this present study has focused on the healing of indents as a model for surface pores in PLGA films, we believe that the numerical tools used to analyze the process and the experimental techniques used to deduce the relevant material properties will be appropriate for predicting the pore-healing processes of significance for pharmaceutical use of these materials.

A.7 Acknowledgements:

This work was partially supported by NIH R21 EB 08873. Graduate-student support for JMM was provided by the PhRMA Foundation's pre-doctoral fellowship in Pharmaceutics. Graduate-student support for JH was provided by the Department of Mechanical Engineering of University of Michigan. The authors would like to thank Prof. Ellen Arruda for the instruments used in the DMA experiments and Dr. Kristen Mills for her guidance in developing the user-subroutine.

A.8 References

1. Schmitt EE, Polistina RA. Surgical sutures 1967.
2. Klugherz BD, Jones PL, Cui X, Chen W, Meneveau NF, DeFelice S, et al. Gene delivery from a DNA controlled-release stent in porcine coronary arteries. Nature Biotechnology. 2000;18(11):1181-4.
3. Wang X, Venkatraman SS, Boey FYC, Loo JSC, Tan LP. Controlled release of sirolimus from a multilayered PLGA stent matrix. Biomaterials. 2006;27(32):5588-95.
4. Pan CJ, Tang JJ, Weng YJ, Wang J, Huang N. Preparation and characterization of rapamycin-loaded PLGA coating stent. Journal of Materials Science: Materials in Medicine. 2007;18(11):2193-8.
5. Patrick Jr CW, Zheng B, Johnston C, Reece GP. Long-term implantation of preadipocyte-seeded PLGA scaffolds. Tissue Engineering. 2002;8(2):283-93.
6. Wang Y, Ameer GA, Sheppard BJ, Langer R. A tough biodegradable elastomer. Nature Biotechnology. 2002;20(6):602-6.
7. Hans ML, Lowman AM. Biodegradable nanoparticles for drug delivery and targeting. Current Opinion in Solid State and Materials Science. 2002;6(4):319-27.
8. Cheng J, Teply BA, Sherifi I, Sung J, Luther G, Gu FX, et al. Formulation of functionalized PLGA–PEG nanoparticles for in vivo targeted drug delivery. Biomaterials. 2007;28(5):869-76.
9. Reinhold SE, Desai KGH, Zhang L, Olsen KF, Schwendeman SP. Self-healing microencapsulation of biomacromolecules without organic solvents. Angewandte Chemie International Edition. 2012;51(43):10800-3.
10. Park JH, Allen MG, Prausnitz MR. Biodegradable polymer microneedles: fabrication, mechanics and transdermal drug delivery. Journal of Controlled Release. 2005;104(1):51-66.
11. Ghahremankhani AA, Dorkoosh F, Dinarvand R. PLGA-PEG-PLGA tri-block copolymers as in situ gel-forming peptide delivery system: effect of formulation properties on peptide release. Pharmaceutical Development and Technology. 2008;13(1):49-55.
12. van Benthem RATM, Ming W, de With G. Self-healing polymer coatings. Self Healing Materials. 2008:139-59.
13. Wilson GO, Andersson HM, White SR, Sottos NR, Moore JS, Braun PV. Self-healing polymers. Encyclopedia of Polymer Science and Technology: John Wiley & Sons, Inc.; 2002.
14. Cho SH, White SR, Braun PV. Self-Healing Polymer Coatings. Advanced Materials. 2009;21(6):645-9.
15. Toohey KS, Sottos NR, Lewis JA, Moore JS, White SR. Self-healing materials with microvascular networks. Nature Materials. 2007;6(8):581-5.
16. Vettiger P, Cross G, Despont M, Drechsler U, Durig U, Gotsmann B, et al. The 'millipede'-nanotechnology entering data storage. Nanotechnology, IEEE Transactions on. 2002;1(1):39-55.
17. Wang J, Wang BM, Schwendeman SP. Characterization of the initial burst release of a model peptide from poly (D, L-lactide-co-glycolide) microspheres. Journal of Controlled Release. 2002;82(2):289-307.
18. Kang J, Schwendeman SP. Pore closing and opening in biodegradable polymers and their effect on the controlled release of proteins. Molecular Pharmaceutics. 2007;4(1):104-18.
19. Nakahara S. Microporosity in thin films. Thin Solid Films. 1979;64(1):149-61.
20. Mazzara JM, Balagna MA, Thouless MD, Schwendeman SP. Healing kinetics of microneedle-formed pores in PLGA films. Journal of Controlled Release. 2013;171(2):172-7.
21. Packard CE, Schroers J, Schuh CA. In situ measurements of surface tension-driven shape recovery in a metallic glass. Scripta Materialia. 2009;60(12):1145-8.
22. Kumar G, Schroers J. Write and erase mechanisms for bulk metallic glass. Applied Physics Letters. 2008;92(3):031901.
23. Chakrabarty J. Theory of plasticity: Butterworth-Heinemann; 2006.
24. Henann DL, Anand L. Surface tension-driven shape-recovery of micro/nanometer-scale surface features in a Pt (57.5) Ni (5.3) Cu (14.7) P (22.5) metallic glass in the supercooled liquid region: A numerical modeling capability. Journal of the Mechanics and Physics of Solids. 2010;58(11):1947-62.

25. Kwok DY, Neumann AW. Contact angle measurement and contact angle interpretation. Adv Colloid Interfac. 1999;81(3):167-249. doi: Doi 10.1016/S0001-8686(98)00087-6. PubMed PMID: ISI:000082127900001.
26. Lakes RS. Viscoelastic Materials. Cambridge: Cambridge University Press; 2009.
27. Sperling LH. Introduction to Physical Polymer Science, 4th Edition. Introduction to Physical Polymer Science, 4th Edition. 2006:1-845. PubMed PMID: ISI:000298543000017.
28. Evans AG, Charles EA. Strength recovery by diffusive crack healing. Acta Metallurgica. 1977;25(8):919-27.
29. Rödel J, Glaeser AM. High-Temperature Healing of Lithographically Introduced Cracks in Sapphire. Journal of the American Ceramic Society. 1990;73(3):592-5601.
30. Smith DL, Evans B. Diffusional crack healing in quartz. Journal of Geophysical Research: Solid Earth. 1984;89(B6):4125 -- 35.

A.9 Figure Captions

Figure A1 Self-healing in PLGA. *a*) A schematic illustration of the healing process showing the shape-recovery of a surface pore driven by stress fields arising from surface curvature. The stress fields can be mimicked by the application of surface tractions that are proportional to local curvatures. *b*) Micrographs of self-healing of pores introduced by indentation of a PLGA film when incubated at 65 °C. *c*) Self-healing of surface pores in PLGA microparticles used in controlled release. The left image is after fabrication using the solvent evaporation method as previously described (9), and the right image is after incubation in solution at 42 °C (above T_g) for 48 hours.

Figure A2 *a*) A schematic illustration of an axisymmetric ellipsoidal surface pore. *b*) The axisymmetric geometry used in the numerical simulations. The boundaries are located at an outer radius of S_o, which is big enough so that the pore can be considered as an isolated pore. The thickness of the substrate is H_o. The bottom symmetry plane models free sliding on a rigid substrate.

Figure A3 The results of a numerical calculation of the healing time of a spherical pore in an infinite visco-elastic body agree with the analytical results. The numerical results are affected by the excessive distortion when the residual radius of the pore is small, resulting in larger uncertainties, as represented by the error bars.

Figure A4 (*a*) Numerical results showing how the residual depth of an ellipsoidal surface pore in a Maxwell material varies as a function of time; these results illustrate how the rate of healing slows down as the pore depth decreases. In this plot, the time, t, has been normalized by the surface tension, γ, the viscosity, η, and the initial volume of the pore, V_o. Wider and shallower pores, of the same initial volume require longer times to reach the same level of healing. The error bars on these plots correspond to numerical uncertainties associated with mesh size. (*b*) Numerical results showing how the cross-sectional profile of a surface pore evolves with time. This images are taken from the simulation used to generate the data of Fig A4a, with $a_o/b_o = 1$.

Figure A5 (*a*) A comparison between the calculated time to heal pores in a wet PLGA film ($T_g = 23.4 \pm 0.4$ °C) and the experimental observations of Mazzara *et al.* (20), as a function of temperature. The geometrical parameters of the ellipsoidal pore used in the numerical calculations were $a_o/b_o = 5/14$, $S_o/a_o = 10$, and $H_o/b_o = 25/7$. These were consistent with the experimental geometries that had pores with an initially square cross section. The material properties were chosen to fit the experimental results at 53 °C, and an activation energy of 193 kJ mol^{-1} for the viscosity had been previously estimated from an Arrhenius fit to these data (20). The uncertainty in the numerical simulations (represented by the dashed lines) matches the uncertainty from the experimental results at 53 °C. (*b*) Good agreement is shown between the predicted and experimentally-observed effects of pore volume and aspect ratio on healing time. The experimental data are from Mazzara *et al.* (20), and the parameters for the numerical studies were identical to those used for Fig A5(a). The uncertainty in the numerical simulations (represented by the dashed lines) comes from the uncertainties to the fit in Fig A5(a).

Figure A6 (*a*) Sample data of stress relaxation tests for dry PLGA films at different temperatures for an initial strain of 3%, using a TA Instruments RSA3 dynamic mechanical analyzer. While the plot for a single thermally-activated relaxation is a straight line, the initial change in slope indicates additional rapid relaxation mechanisms. Only the longer-scale relaxation data were obtained from this plot. The constant slope associated with this longer time scales starts when the time-dependent modulus is 1.5 ± 0.5 MPa. (*b*) The time constant, t_m, obtained from the data of Fig A6(a) decreases as the temperature, T, increases. An Arrhenius plot of relaxation time against $1/T$ shows an activation energy of 206 ± 6 kJ mol^{-1} for the viscosity term responsible for the slow relaxation in the temperature range of 40 °C to 65 °C. The data also indicate that the pre-exponent for the time constant (Equation 2) is given by t_{mo} = 6.4 ± 0.2 x10^{-32} s.

Figure A7 (*a*) Temperature dependence of storage modulus and loss tangent determined by DMA for dry PLGA films. The tests were conducted at a constant frequency of 1 Hz. Three samples were tested, and the average value has been plotted. The double peaks in tanδ indicate at least two relaxation mechanisms with similar time constants in the temperature range, which can be approximated by one equivalent dashpot. The unrelaxed storage modulus is estimated to be 1.6 ± 0.3 GPa. (*b*) Representative data from DMA frequency sweep test showing the storage and loss modulus as functions of frequency for dry PLGA films at 30 °C. The loss modulus presents with a single peak within the range of frequency analyzed, and can be interpreted based on a standard linear solid model. The time constant can be calculated from the peak in the loss modulus, as explained in the text. (*c*) The time constant obtained from data such as that shown in Fig A7b decreases as the temperature, T, increases. An Arrhenius plot shows an activation energy of 250 ± 29 kJ mol^{-1} for the fast relaxation. The pre-exponent for the time constant (Equation 2) is given by τ_{so}= 6.6 ± 0.8 x 10^{-44} s.

Figure A8 Proposed material model for PLGA. (*a*) The model consists of a standard linear solid in series with a dashpot. The standard linear solid series provide a time-dependent initial modulus for the lower dashpot. The material has a fully-relaxed modulus of zero, ensuring complete healing to occur. The lower dashpot is the dominant relaxation mechanism at longer time scales. (*b*) The equivalent model used as a Prony series for finite element calculations in ABAQUS, with $E_1 = E_s$, $E_2 = E_r$, $\eta_1 = (1/\eta_s + 1/\eta_m)^{-1}$, and $\eta_2 = \eta_m$. E_3 was arbitrarily chosen for the implementation of the Prony series, and was sufficiently small so as not to impede healing.

Figure A9 The predicted time to heal a surface pore in dry PLGA films, using the material properties obtained in this study. Three different definitions of healing, 83%, 85% and 87% are shown to illustrate the sensitivity of the results to the definition of healing. The predicted results are in good agreement with the experimental observations at high temperatures, but predict too short a healing time at lower temperatures.

Figure A10 The predicted time to heal a surface pore in annealed PLGA films, using the annealed properties of the PLGA. The annealed properties provide a better match for the predictions at low temperatures, while the un-annealed properties provide a better match at higher temperatures. This is consistent with the notion that the long healing times at low temperatures allow annealing to occur, and the corresponding loss of solvent reduces the viscosity of the PLGA.

Supplementary Data

Figure AS1 The weight of dry PLGA films measured as a function of time when held at 50 °C, 55 °C, and 65 °C. The relative weight change percentage of evaporated solvent after 8 hours of treatment was 1.9 ± 0.2%.

Supplementary Movie A1: Simulated healing of a surface pore in a Maxwell film. The pore geometry used was a_o/b_o=1. The corresponding pore depth as a function of time can be found in Fig A4a. This movie can be viewed at http://www.sciencedirect.com.proxy.lib.umich.edu/science/article/pii/S0168365915001352.

Supplemental Figure 1